DISS. ETH NO. 30417

Openable Self-Bearing Motor Sealless Production Ultracentrifuge, and Acoustic Diagnosis

A thesis submitted to attain the degree of

DOCTOR OF SCIENCES
(Dr. sc. ETH Zurich)

presented by

EMANUEL JOHANNES HUBMANN

born on 12.06.1993

accepted on the recommendation of

Prof. Dr. Johann W. Kolar, examiner
Prof. Dr. Elena A. Lomonova, co-examiner

2024

ETH Zurich
Power Electronic Systems Laboratory
Physikstrasse 3 | ETL H23
8092 Zurich | Switzerland

http://www.pes.ee.ethz.ch

I would like to dedicate this work to my dear parents,
Katharina and Hanspeter Hubmann-Graf.
Emanuel J. Hubmann

Acknowledgments

First, I express my gratitude to Prof. Dr. Johann W. Kolar for giving me the opportunity to conduct my doctorate at his renowned Power Electronic Systems Laboratory, PES, at the Swiss Federal Institute of Technology, ETH Zurich. He deserves my sincere thanks for his continuous supervision throughout my doctorate. His warm welcome to his laboratory and making me part of his wonderful team immediately filled me with the pioneering and innovative spirit he established in his laboratory. His scientific and strategic guidance thorough the doctorate are the foundations of this dissertation. His financial support through PES was crucial to conducting this doctorate. His dedication to maintaining the highest research quality standards in his laboratory and conducting cutting edge research in an international group will continue to inspire me in my future career.

I would like to thank Prof. Dr. Elena A. Lomonova, Professor and Chair of Electromechanics, Power Electronics and Motion Systems at Eindhoven University of Technology, for the honor of having her to serve as the co-examiner of this dissertation, reviewing it as a highly regarded expert in magnetic levitation.

The Swiss Innovation Agency, Innosuisse, has made a significant contribution to the success of this dissertation through its substantial financial support, for which I am very grateful.

I would like to express my deep gratitude to the company Levitronix GmbH for its scientific and financial support for my doctorate. Having Levitronix as an industrial partner of this research collaboration allowed us with its expertise and capabilities to achieve as a collaboration the industry-oriented research results presented in this thesis.

I am greatly indebted to all senior scientists from PES and Levitronix, which I was honored to call my mentors during my doctorate. Dr. Michael Flankl onboarded me at PES and introduced me to the ongoing electric motor know-how and research at PES. Dr. Dominik Bortis provided guidance in the beginning of the doctorate, and we worked together for his new lectures ”Fundamentals of Electric Machines”, and ”Design and Control of Electric Machines”. From Levitronix, Dr. Daniel Steinert as an industry expert in magnetic levitation supported me in all aspects during the dissertation and Dr. Thomas Nussbaumer supported me from an industrial strategy and research point of view.

During my doctorate, I received incredible support from outstanding colleagues from PES and Levitronix GmbH. I would like to mention especially Ass. Prof. Dr. Dr. Spasoje Miric, Dr. Panteleimon Papamanolis, Dr.

Michael Haider, Dr. Rosario Giuffrida, Dr. Pascal Niklaus, Dr. Morris Heller, Dr. Jon Azurza, Fabian Weissofner, Florian Wassmer, Jonas Gine, Andreas Kalapos, Marcel Stettler, Dr. Thomas Schneeberger, Dr. Thomas Holenstein, Dr. Ivana Bagaric, Lars Beglinger, Philipp Campos, Dr. Thomas Gempp, Dr. Reto Schoeb, Peter Seitz, Monica Kohn, Yonne Schynder-Lieberherr, Prisca Maurantonio, Nadine Wacha and Roswitha Coccia. A special thanks also goes to the workshops at D-ITET, ETH Zurich, and Levitronix GmbH for their very skillful manufacturing of prototype parts.

Furthermore, I would like to thank deeply all extremely talented PES students whom which I was honored to work with as a main supervisor during my doctorate; Lukas Blassnig, Daniel Paisdor Paimes, Stefan Erismann, Florian Henzer, Christian Blaser, Leon Kroll, Ricco Eberhard and Cyrill Mast. I am very happy seeing them pursuing their own successful career in industry.

The work with the excellent teaching assistants, Bruno Kola and Matej Durjaika, for the newly established lectures ”Fundamentals of Electric Machines” and ”Design and Control of Electric Machines” was a great pleasure.

I would like to express my gratitude also to ap. Prof. Dr. Marcus Granegger, who encouraged and supported me to pursue a doctorate and prepared me very well for it during my master thesis at his mechanical circulatory support laboratory.

I would additionally like to thank everyone, which behind scenes gave support, and is not mentioned by name or organization.

Without the continuous condition-less support of my family and close circle, my doctorate would not have been possible. I would like to thank my dear parents Katharina and Hanspeter, and my dear sister Magdalena for their continuous support and encouragement. Furthermore, I would like to thank Farida ElHarouni for her great support during this challenging journey.

Zurich, January 2025

Emanuel J. Hubmann

Abstract

The production of new vaccines for infectious diseases and innovative gene therapies demands purification systems, that are operational within a very short time and achieve exceptionally high levels of purification. Ultracentrifuges deliver excellent results on a research laboratory scale for the purification of active ingredients in the pharmaceutical industry. However, due to technological limitations, such as speed and thus separation performance limitation by rotary seals, contamination risk, and complexity, ultracentrifuges are being displaced by chromatography methods on a production scale. In this dissertation, these technological drawbacks are addressed and a new sealless production ultracentrifuge concept is proposed.

The newly proposed openable magnetic self-bearing motor and openable burst armor allow the rapid exchange of a completely hermetically sealed pre-sterilized production ultracentrifuge process chamber including the rotor, without loss of sterility. Technical challenges such as the implications of the unavoidable yoke air-gaps between the motor halves, a scalable passive stator heat extraction method for toroidally wound slotless self-bearing high-speed motors, a sealless rotor fluid path, stable active magnetic rotor suspension during dynamic filling of the rotor during rotation, and the achievement of rotational speeds with openable self-bearing motors of over 100 krpm are successfully solved. The principal effectiveness of the proposed concept is validated experimentally by the sedimentation of whey proteins. To prevent system failure during its service life with high damage potential by the very high rotor energy, a diagnosis capability is required at rotor standstill. The magnetically self-bearing functionality enables new system diagnostic methods as an excitation source, allowing the measurement of system responses. The magnetic bearing rotor displacement measurement is identified as being limited in detecting structural resonances in the system. Therefore, a supplement with a microphone as an acoustic sensor is proposed, and examples are shown, of how system faults can be detected, even when the rotor is magnetically levitating, but at standstill.

In summary, this dissertation proposes and validates a new sealless production ultracentrifuge concept, that provides solutions to the limitations of today's production ultracentrifuges. It is available as a platform for pharmaceutical and biotechnology research for refining the new concept's process chamber and rotor internal structure to specific pharmaceutical purification method needs. The presented sealless ultracentrifuge concept has the potential to enable new high quality, high through-put, guaranteed contamination free pharmaceutical purification processes with extremely small batch changeover time.

Kurzfassung

Für die Herstellung von neuen Impfstoffen gegen ansteckbare Krankheiten und für neue Gen-Therapieformen werden schnell einsatzbereite Purifikations-Anlagen benötigt, die extrem hohe Reinheitsgrade erreichen. Ultrazentrifugen liefern im Forschungs-Labormassstab hervorragende Ergebnisse für die Purifikation von Wirkstoffen in der pharmazeutischen Industrie. Aufgrund von technologischen Nachteilen wie der Drehzahl- und somit Trennleistungs-Limitierung durch Rotationsdichtungen, dem Kontaminationsrisiko, und der Komplexität werden Ultrazentrifugen im Produktionsmassstab jedoch von Chromatographie-Methoden verdrängt. Durch das im Rahmen dieser Dissertation vorgeschlagene neue dichtungslose Produktions-Ultrazentrifugen-Konzept werden diese technologischen Nachteile vermieden.

Der vorgeschlagene aufklappbare, magnetisch selbstgelagerte Motor mit einem ebenfalls aufklappbaren Berstschutz erlaubt neu das rasche Auswechseln einer vorsterilisierten, komplett hermetisch verschlossenen Produktions-Ultrazentrifugen-Einheit. Dabei auftretende technische Herausforderungen wie die Implikationen der unvermeidbaren Magnetkreis-Joch-Luftspalte, die skalierbare passive Stator Wärmeabfuhr eines toroidal gewickelten, nutenlosen selbstgelagerten Hochgeschwindigkeits-Antriebs, eine Rotorfluid-Führung ohne Dichtungen, die stabile magnetische Lagerung während des Füllvorgangs des Rotors bei Drehzahl, und das Erreichen von Rotationsgeschwindigkeiten des aufklappbaren selbstgelagerten Antriebs von über 100'000 U/min werden erfolgreich gelöst. Die Wirkungsweise des vorgeschlagenen Konzepts wird experimentell durch die Sedimentation von Molke-Proteinen nachgewiesen.

Um einen Systemversagen während seiner Lebensdauer mit hohem Schadenspotenzial durch die sehr hohe Rotorenergie zu verhindern, ist eine Diagnosefähigkeit noch im Stillstand erforderlich. Die magnetische Lagerung ermöglicht neue Systemdiagnose-Methoden durch Nutzung der Magnetlager als Anregungsquelle und Messung der Systemantwort. Die Detektion struktureller Resonanzen in der Anlage durch die Verschiebungsmessung des Rotors wird als limitiert identifiziert. Hierfür wird eine Ergänzung mit einem Mikrophon als akustischen Sensor vorgeschlagen und in Beispielen aufgezeigt, wie bereits bei schwebendem aber noch stillstehendem Rotor Systemfehlzustände erkannt werden können.

Zusammenfassend wird im Rahmen dieser Dissertation ein neues dichtungsloses Produktions-Ultrazentrifugen-Konzept vorgeschlagen und validiert, das Lösungen für die Limitierungen der heutigen Produktions-Ultrazentrifugen präsentiert. Somit steht eine neue Plattform für pharmazeutische und biotechnologische Forschung zur Verfügung für die Verfeinerung der Konstruktion der Prozesskammer und des Rotors für die spezifischen pharmazeutischen Purifikations-Bedürfnisse abhängig vom Wirkstoff. Das vorgeschlagene Produktions-Ultrazentrifugen-Konzept hat das Potential, qualitativ hochwertige, mit hohem Durchsatz betreibbare und garantiert kontaminationsfreie pharmazeutische Purifikationsprozesse mit extrem kleiner Chargenumstellungszeit zu ermöglichen.

Contents

1 Introduction

Modern societies are susceptible to outbreaks of new communicable diseases. Communicable diseases can today spread very quickly worldwide due to human mobility behavior, for example in large densely populated cities, at major public events or with international air traffic. The outbreak of the COVID-19 pandemic has brought the risks of communicable diseases back to the fore at a societal level. The health, social and economic consequences of outbreaks can be severe. Possible future outbreaks can be of natural origin, but can also be caused by human made threats, for example through laboratory accidents, the use of bio-weapons in conflicts or bio-terrorism [1]. The pharmaceutical industry is therefore called upon to improve technologies to be able to respond more quickly to limit the damage in such scenarios. After detection of an outbreak, research and industry are required to be able to develop suitable vaccines and to produce them on a large scale for the world's population need in very short time frames.

With the increasing life expectancy of society, diseases which are more prone to appear later in life, such as cancer, are becoming more relevant. Many of these diseases lack an option for treatment today. Furthermore, new production processes are required for new types of treatment options, as e.g. for viral vector-based gene therapies. In the pharmaceutical industry, purification processes, that ensure an extremely high degree of purity are required. Co-produced species in cell cultures, that are similar to the intended product, but have no therapeutic effect, such as empty capsids in viral vectors are undesired. Removal from the substance intended for medical use is necessary, because they lead to unnecessary immune reactions in patients [2], [3].

Fig. 1.1 illustrates a simplified biotechnological production process workflow. The substance of interest is produced in the upstream process. After

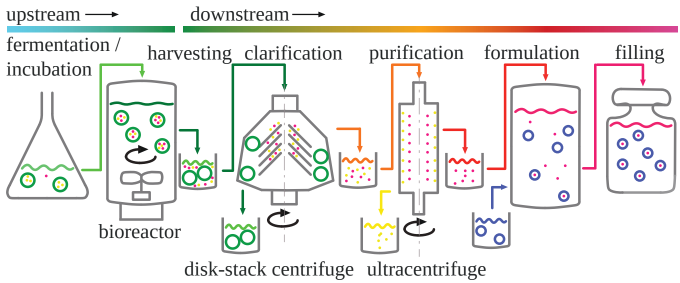

Fig. 1.1: Simplified biotechnological production process with centrifuges for separation. Producing the substance of interest in the upstream process. After harvesting followed by the downstream process, clarifying, purifying, formulation and filling, the substance of interest is isolated and prepared, ready to be supplied to the patient. To reduce filter area, the application of centrifuges for clarification and ultracentrifuges for purification is desired.

harvesting, everything other than the substance of interest has to be separated. A clarification step removes larger particles like cell debris. Purification removes remaining impurities other than the substance of interest. Formulation and filling conclude the process. In an attempt to reduce the amount of required filter area, for clarification, disk-stack centrifuges can be employed, while for purification if based on the centrifuge principle, ultracentrifuges are needed.

To investigate the main factors of influence on the separation process, the sedimentation process within a centrifuge or ultracentrifuge is analyzed as follows. The drag force F_d on a small sphere shaped particle with radius r_p in a fluid with dynamic viscosity η_f, sedimenting slowly with the velocity u_p according to Stokes Law [4] is

$$F_\mathrm{d} = 6\pi\eta_\mathrm{f} r_\mathrm{p} u_\mathrm{p}. \tag{1.1}$$

During sedimentation, F_d is equal to centrifugal force F_c subtracted by the buoyancy force F_d,

$$F_\mathrm{d} = F_\mathrm{c} - F_\mathrm{b}, \tag{1.2}$$

with the centrifugal force F_c based on the particle density ρ_p, particle volume V_p, radius of the centrifuge r_CF (simplified to be constant), and the rotational speed Ω of the rotor, equal to

$$F_\mathrm{c} = \rho_\mathrm{p} V_\mathrm{p} r_\mathrm{CF} \Omega^2, \tag{1.3}$$

and the buoyancy force equals to

$$F_\mathrm{b} = \rho_\mathrm{f} \mathrm{g} V_\mathrm{p}, \tag{1.4}$$

with the fluid density ρ_f, and gravitational constant g. With the ratio R_ρ of particle to fluid density,

$$R_\rho = \frac{\rho_\mathrm{p}}{\rho_\mathrm{f}} \tag{1.5}$$

the drag force becomes

$$F_\mathrm{d} = V_\mathrm{p} \rho_\mathrm{f} \left(R_\rho r_\mathrm{CF} \Omega^2 - \mathrm{g} \right). \tag{1.6}$$

With the relative centrifugal acceleration C defined as

$$C = \frac{r_\mathrm{CF} \Omega^2}{\mathrm{g}}, \tag{1.7}$$

the drag force becomes

$$F_\mathrm{d} = V_\mathrm{p} \rho_\mathrm{f} \mathrm{g} \left(R_\rho C - 1 \right). \tag{1.8}$$

This can be solved for the sedimentation velocity:

$$u_\mathrm{p} = \frac{V_\mathrm{p} \rho_\mathrm{f} \mathrm{g} \left(R_\rho C - 1 \right)}{6 \pi \eta_\mathrm{f} r_\mathrm{p}}. \tag{1.9}$$

The sedimentation time t_s results as the fraction of the path length l, which is a process design parameter, and the sedimentation velocity:

$$t_\mathrm{s} = \frac{l}{u_\mathrm{p}} \tag{1.10}$$

$$t_\mathrm{s} = \frac{l 6 \pi \eta_\mathrm{f} r_\mathrm{p}}{V_\mathrm{p} \rho_\mathrm{f} \mathrm{g} \left(R_\rho C - 1 \right)}. \tag{1.11}$$

With the particle volume of

$$V_\mathrm{p} = \frac{4}{3} \pi r_\mathrm{p}^3, \tag{1.12}$$

the sedimentation time t_s results as

$$t_\mathrm{s} = \frac{9 l \eta_\mathrm{f}}{2 \mathrm{g} r_\mathrm{p}^2 \rho_\mathrm{f} \left(R_\rho C - 1 \right)}. \tag{1.13}$$

The sedimentation time t_s is therefore in this simplified analysis proportional to the path length l and fluid viscosity η_f. While the fluid choice is more influenced by the desired fluid density or density gradient and bio-compatibility, the viscosity cannot be chosen freely. The path length l is a process design parameter. A small l leads to shorter sedimentation time, however it reduces the processing volume. In a process design, l is therefore an optimization parameter which can be varied for a fixed rotor diameter with corresponding rotor inserts. The sedimentation time t_s is inversely proportional to the square of the particle radius r_p. This shows the increasing difficulty to separate particles with decreasing particle size. The inverse proportionality to the relative centrifugal acceleration C with the quadratic dependence of C on the rotational speed Ω and proportionality to the centrifuge rotor radius r_{CF} shows the fundamental importance of high rotational speeds. A centrifuge with extremely high $C > 100'000\,\mathrm{g}$, i.e. an ultracentrifuge, allows the separation of extremely small particles despite their very small density difference.

Laboratory scale research ultracentrifuges are used successfully for purification [2]. The global demand of active ingredients requires large scale industrial production ultracentrifuges (PUCFs). However, today's PUCFs have disadvantages, that prevent their widespread use.

The rotary seals between the rotor and fluid inlets and outlets, intended as a contamination barrier, pose a risk of contamination in both directions. There is therefore a risk of infectious aerosols generation [2], [5], and of contamination or impurity of the product to be purified. Furthermore, the rotary seals limit the speed to approx. 40 krpm, which limits the relative centrifugal acceleration C and thus process speed. The mechanical bearings lead to complexity of the systems and complexity in operation. To exchange the rotor, the motor and rotor assembly must be lifted away in an axial direction and the rotor must be removed axially from the bearing and seal, exposing the rotor to the production facility environment. Hence, there is no hermetic containment of the wetted parts. Extensive cleaning and sterilization procedures are required. Presumably due to the complexity of today's PUCF systems, there are very few manufacturers and few available PUCF systems.

For these reasons, it is considered difficult to scale up manufacturing processes for active ingredients from research laboratory scale to industrial production scale with PUCFs. Therefore, chromatography is mainly used for production processes nowadays [2].

Nevertheless, chromatography shows difficulties in separating particles, that are externally identical or very similar, but differ internally [2]. PUCFs can separate particles based on their density. If the aforementioned problems of PUCFs could be solved, PUCFs would have the potential to play a major role in purification processes again, or to supplement chromatography as a subsequent polishing step. This would potentially solve the problem of unwanted immune reactions due to insufficient purification levels of currently existing methods.

The origins of UCFs lie in chemistry research. Analytical UCFs were developed to determine physical properties such as the size and weight of particles such as proteins. The sedimentation process is observed optically in real time through windows in the rotor. The samples are placed in sealed containers within the rotor. To determine particle sizes and distributions, Svedberg built a centrifuge with a relative centrifugal acceleration of $C = 7'000$ and rotational sped of $12'000$ rpm, which they for the first time called ultracentrifuge, in this dissertation abbreviated as UCF [6].

Reference [7], reached with a later analytic UCF a relative centrifugal acceleration of $C = 100'000$ g at $42'000$ rpm, powered by an oil turbine. Svedberg was later awarded the Nobel Prize for his work with analytical ultracentrifuges [6]. This laid the foundations for UCFs. However, these analytical centrifuges with sealed samples in the rotor are neither intended nor suitable for the production of active ingredients. Later, preparative UCFs were developed to carry out purification processes on a laboratory scale for small quantities. Individual small, sealed tubes are inserted into a rotor, centrifuged, and then removed again.

PUCFs intended for the production on a large scale were first developed by Jesse Beams as part of the Manhattan Project for uranium gas enrichment, but discarded for this purpose. The first practical magnetic bearing suspension for rotors was realized by Beams [8] in this process. The aim of his first applied magnetic bearing was to hold the weight of the vertically oriented rotor. The first zonal UCF rotor was built in 1954 by reference [9] for the application of liquid suspensions for pharmaceutical use at the Oak Ridge Laboratory [10]. However, magnetic bearings did not gain a foothold for pharmaceutical PUCF applications. These activities in PUCF research gave rise to the k-series PUCFs [11], [12], [13], [14], [15]. Initially, these PUCF types were driven by turbines. Nowadays, high-speed electric motors are offered. These types are still in use with modifications and improvements: "K centrifuges have come into worldwide use for large-scale virus isolation and have been commercially available with little rotor modification for the last 35 years. Approximately 200 such systems have been constructed [16]. A tubular PUCF suspended by self-bearing motors was presented in [17] for the production of nano-particles. However, a potential translation of this solution into a pharmaceutical application still keeps the problem of loss of sterility during rotor exchange unsolved. There is up to now no apparent solution to the problems of current PUCFs.

1.1 Aims

The industrial purification of active ingredients requires a safe, reliable method without contamination risk, which can separate particles of only smallest differences in density with extremely small process batch changeover time. State of the art PUCFs cannot fulfill this requirement. A new possible solution is therefore proposed and investigated within this dissertation: a sealless production ultracentrifuge (SL-PUCF) with openable magnetically self-bearing motors (O-SBMs). This concept aims to allow for fast exchange of a hermetically sealed process chamber including the rotor and the already connected inlets and outlets. No wetted components, which are potentially contaminated by the process, need to be exposed to the clean room environment during the exchange. Opening the O-SBMs enables the hermetically contained process chamber including the rotor to be replaced in radial direction extremely quickly. The rotor suspension is contact-free due to the magnetic self-bearing motor functionality. By eliminating the rotary seal, its speed limitation is no longer present. Together with the elimination of mechanical bearings, lubrication and damping elements, the complexity of the PUCF is substantially reduced. Furthermore, heat generation due to friction in the seals and the need for maintenance on seals, bearings and damper elements becomes obsolete. In addition to time savings due to the very fast set-up time and the potential for faster processes thanks to the possible higher speed, hermetic containment also reduces the risk of contamination in both directions and thus the risk of process failure. The fact that the pre-sterilized, hermetically enclosed exchangeable rotor units can be pre-certified also helps to ensure a fast response time in pandemic cases. This eliminates the need for a lengthy on-site validation process, specific to each system to be installed. Failure of a PUCF system causes severe system damage associated with high cost and has therefore to be avoided with the highest certainty by detection of the fault before speed ramp up of a faulty system. In addition to safe design and control, a monitoring capability is therefore desirable to assess the systems health status already at standstill. The magnetic suspension opens up new possibilities for system diagnostics thanks to their ability to excite the system for frequency response measurement purposes. It is therefore investigated additionally in this work, to which extent excitation by magnetic bearings can be used to obtain information for system diagnostics. The magnetic bearing displacement data is investigated, and limitations are identified. It is therefore proposed to circumvent this limitation by adding a microphone as an acoustic sensor.

1.2 Thesis Outline

The challenges to be solved in this dissertation to achieve the aforementioned aims are structured into the following chapters:

1.2.1 Outline of Chapter 2: 100 krpm Openable Self-Bearing Motor

- A suitable self-bearing motor topology is required for the proposed novel openable self-bearing motor functionality.
- The opening functionality requires a corrosion protection of the exposed motor yoke surfaces, which magnetically results in yoke air-gaps. They affect the motor and magnetic bearing performances.
- The rotor dynamics, especially the flexural rotor bending modes restrict the system design.
- Very high rotational speeds of 100 krpm are required for future PUCFs for short batch processing times.

1.2.2 Outline of Chapter 3: Sealless Production Ultracentrifuge and its Openable Self-Bearing Motors

- Potential applications of the proposed technology need to be identified.
- The axial magnetic bearing resonance needs to be surpassed.
- A new solution for a rotor fluid path without rotary seals is required.
- Rotor imbalance due to unequal rotor internal fluid distribution is a risk.
- Appropriate heat extraction of the motor losses needs to be ensured to avoid system overheating to ensure safe temperatures of the processed biological materials.

- An openable burst armor is required to ensure rotor fragment containment and opening capability for fast rotor exchange.

1.2.3 Outline of Chapter 4: Acoustic Diagnosis

- The risks associated with the large kinetic energy stored in the very high speed PUCF rotor ask for a method to diagnose the PUCF system's health status before the speed is ramped up.
- The extent, to which magnetic bearings are capable to measure mechanical system resonances is unknown and therefore also their capabilities for system diagnosis.
- The proposed concept of extending the sensing capability with a microphone as an acoustic sensor needs to be extremely sensitive to be able to sense minor defects in the system.

1.3 List of Publications

Key insights presented in this dissertation have already been published or will be published in international scientific journals and conference proceedings. The publications created as part of this dissertation, or also in the scope of other projects, are listed below.

1.3.1 Journal Papers

- **E.J. Hubmann**, R. Eberhard, C.F. Blaser, S. Erismann, D. Steinert, T. Nussbaumer and J.W. Kolar, "Magnetically self-bearing drive system for ultracentrifugation: Towards 100'000 rpm and 200'000 g," *IEEE Transactions on Industry Applications,* vol. 60, no. 1, pp. 321-331, January 2024.
- **E.J. Hubmann**, D. Steinert, T. Nussbaumer and J.W. Kolar, "Sealless production ultracentrifuge and its magnetically self-bearing openable motors for purification in viral nanotechnology," *IEEE Access (Early Access),* January 2025.
- **E.J. Hubmann**, F. Weissofner, D. Steinert, T. Nussbaumer and J.W. Kolar, "Novel acoustic failure prediction method for active magnetic bearing systems," *IEEE/ASME Transactions on Mechatronics,* vol. 29, no. 2, pp. 1181-1192, April 2023.

1.3.2 Conference Papers

- **E.J. Hubmann**, C. F. Blaser, S. Erismann, D. Steinert, T. Nussbaumer and J. W. Kolar, "Magnetically self-bearing drive system for ultracentrifugation: Towards 100'000rpm and 200'000g," *in Proc. of 24th International Conference on Electrical Machines and Systems (ICEMS),* pp. 88-94, 2021.
  (Best Paper Award)

1.3.3 Further Scientific Contributions

- **E.J. Hubmann**, D. Bortis, M. Flankl, J. W. Kolar, M. Granegger and M. Hübler, "Optimization and calorimetric analysis of axial flux permanent magnet motor for implantable blood pump assisting the Fontan circulation," *in Proc. of 22nd International Conference on Electrical Machines and Systems (ICEMS), Harbin, China,* pp. 1-8, 2019.
  (Best Paper Award)

- A. Escher, C. Strauch, **E.J. Hubmann**, M Hübler, D. Bortis, B. Thamsen, M. Mueller, U. Kertzscher, P.U. Thamsen, J.W. Kolar, D. Zimpfer and M. Granegger, "A cavopulmonary assist device for long-term therapy of fontan patients," *Seminars in Thoracic and Cardiovascular Surgery,* vol. 34, no. 1, pp. 238-248, 2022.

2
100 krpm Openable Self-Bearing Motor

This chapter summarizes the most relevant findings regarding the concept, design and realization of a 100 krpm openable self-bearing motor , which are also published in:

- **E.J. Hubmann**, R. Eberhard, C.F. Blaser, S. Erismann, D. Steinert, T. Nussbaumer and J.W. Kolar, "Magnetically self-bearing drive system for ultracentrifugation: Towards 100 krpm and 200'000 g," *IEEE Transactions on Industry Applications,* vol. 60, no. 1, pp. 321-331, September 2023.

Chapter Abstract

A novel magnetically double self-bearing drive system for ultracentrifugation in pharmaceutical and chemical industry is presented, built as a prototype and operated. The prototype successfully reached its operating speed of 100 krpm. It features an opening stator functionality allowing for fast removal of the ultracentrifuge rotor while enabling future centrifugal acceleration levels of 200′000 g. The openable stators require a stator encapsulation, provoking unavoidable stator yoke air-gaps. Parasitic induced phase-currents were identified, a current-control strategy proposed to diminish them and successfully implemented and operated on the prototype.

2.1 Introduction

In biochemistry, fundamental processes are the separation of components of heterogeneous mixtures and purification with ultracentrifuges. Typical ultracentrifuge rotors today are mechanically suspended. Mechanical suspension at high speeds impairs rotor accessibility, requires complicated sealing, causes bearing losses, requires lubrication, generates wear, poses a contamination risk and leads to limited life-time or maintenance needs. These are all limitations of the current technology applied in industry. In [18], the feasibility of a novel system solving these problems was conceptually shown. This chapter now presents the new fully established working hardware. Furthermore, solutions to problems and challenges related to current control and rotor dynamics which were not yet anticipated in [18] are shown.

In [17], a magnetic levitation based continuous flow ultracentrifuge (UCF) prototype was presented, reaching a centrifugal acceleration C of up to $C = 10^5 g$ and a flow rate of $Q = 0.4\,\mathrm{L/min}$ with a rotational speed higher than 64 krpm. However, the access to the UCF rotor for e.g. cleaning is difficult for the operators due to the self-bearing motor stators fully enclosing it.

This chapter presents a novel magnetically self-bearing openable drive system, omitting these limitations.

Fig. 2.1 shows a conceptual illustration thereof. Two self-bearing motors (SBMs), forming a double self-bearing motor, drive the UCF rotor and keep it contact-less in place. As a special feature, a joint between the self-bearing motor modules allows access to the rotor and simple insertion or removal thereof.

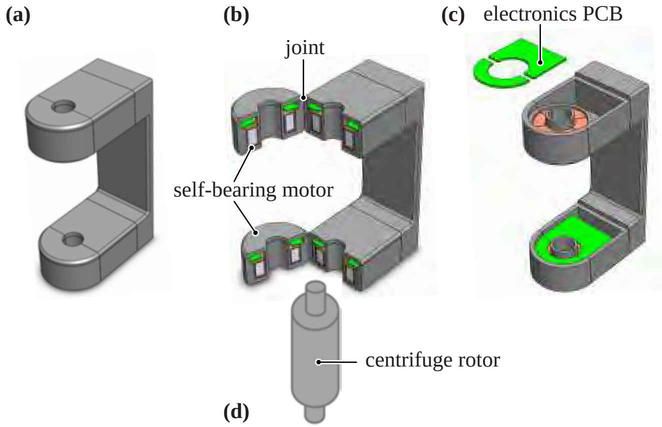

Fig. 2.1: **(a)** Conceptual illustration from [18] of the novel magnetically self-bearing drive system for the targeted 100 krpm and 200′000 g ultracentrifugation. **(b)** Accessible ultracentrifuge rotor for insertion or removal by operators. **(c)** Possible placement of the power electronics. **(d)** Conceptual illustration of the ultracentrifuge rotor.

Compared to modularly assembled stators during motor manufacturing (e.g. shown in [19]), which are and remain inevitably closed after assembly, the presented self-bearing motors need to be openable by the UCF operators in industry.

This chapter presents a new hardware UCF drive-system prototype fulfilling the target performance for the industrial UCF application. It furthermore presents solutions to the faced technical challenges in the previously unknown current control strategy of novel openable motors and the rotor-dynamics of the UCF.

In Fig. 2.2(a) the realized prototype of the double self-bearing UCF drive system is shown. It is in the closed ready-to-operate state. Fig. 2.2(b) shows the unique novel ability to unfold in an open state for removal or replacement of the UCF rotor. The indicated system dimensions in Fig. 2.2 are specified in Tab. 2.1

This chapter is structured as follows. In Section 2.2, two key design challenges are discussed: on the one hand the requirement to have a stator that can be opened and on the other hand the requirement to realize a rotor with bending resonance frequencies above 100 krpm, outside the speed operating range. In Section 2.3, the topology choice and its working principle is explained. In Section 2.4, the realized motor prototype is presented,

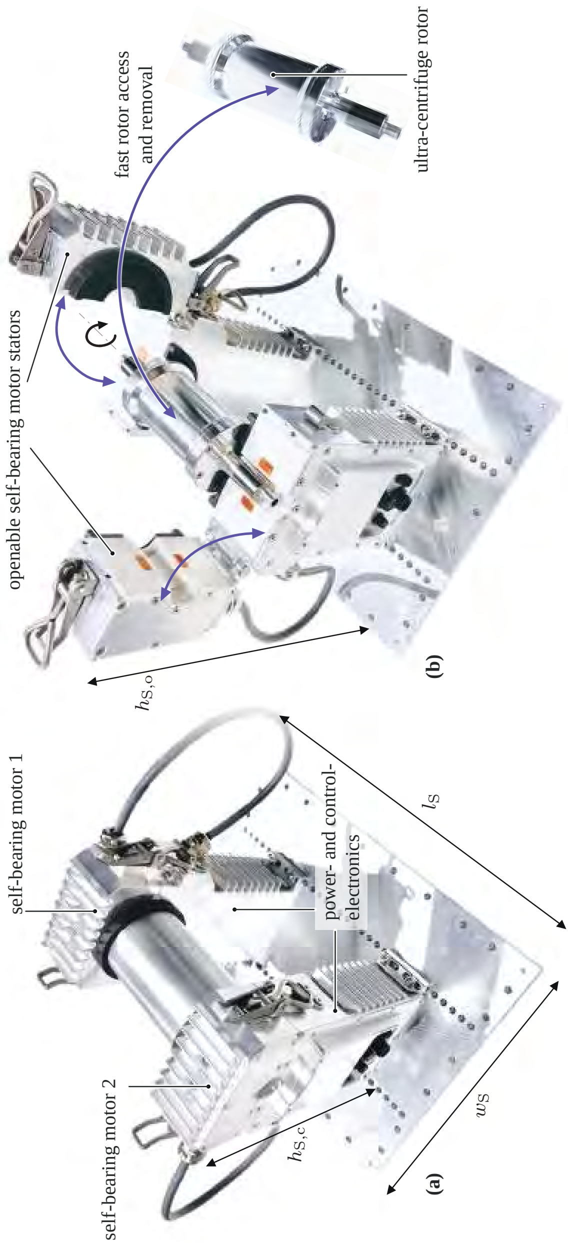

Fig. 2.2: (a) Dual self-bearing motor ultracentrifuge drive system prototype in closed ready-to-operate state. **(b)** Unique novel self-bearing motors being able to unfold into an open state for removal or replacement of the ultracentrifuge rotor by operators. (Indicated system dimensions specified in Tab. 2.1).

and a fundamental challenge for novel openable motors unveiled. Necessary encapsulation of the stator halves leads to unavoidable yoke air-gaps. The occurrence of resulting flux variations in the stator during operation causes parasitic phase-currents. Therefore, the usage of an $L-$filter and a voltage feed-forward compensation current control scheme is proposed. In Section 2.5, the rotor bending resonances are investigated and sub-critical rotor behavior is shown using 3D-FEM simulation and an acoustic impulse response experiment. The new UCF drive system prototype was successfully commissioned and operated with the proposed current control scheme up to 103′000 rpm. An experimental proof of that high-speed operation and the working of the proposed control method is shown in Section 2.6. The findings are finally summarized in Section 3.8 and an outlook is provided.

2.2 Key System Design Challenges

In [18], the competing system design relationships for a drive system for UCF application were revealed. On the one hand, the rotor diameter of the UCF and its operating speed must be selected such that the desired centrifugal acceleration is achieved (200′000 g in this chapter). On the other hand, the drive system must be able to provide necessary mechanical power to the rotor to overcome the air friction losses resulting from the rotor speed, diameter and length. The denser the rotor material, the higher the material load and thus its strength requirement. The rotor material must therefore have a suitable combination of low material density and high strength. In turn, the rotor design must have sufficiently high bending resonance frequencies, determined by the weight and stiffness combination, such that they are not excited during operation.

In the following, the two key challenges are highlighted: on the one hand the requirement for the self-bearing drive system to have an openable stator, on the other hand, the requirement for a sub-critical rotor design for the target speed of 100 krpm.

2.2.1 Self-Bearing Motor Opening-Capability

To allow for fast insertion and removal of the UCF rotor by operators in an industrial manufacturing plant, the novel UCF drive-system requires a stator which is split in two separate segments and therefore can be mechanically opened as shown in Fig. 2.3(a).

While open, the stator-halve interface is exposed to the outside production facility/laboratory-environment conditions. It therefore must be protected from external influences such as contact with process fluids, cleaning agents or unintentional mechanical impacts. Especially the stator core requires special protection. For this purpose, a 0.1 mm thick protective paint coating is envisaged on the exposed stator core separation surfaces. Such a coating behaves magnetically like air, and is therefore referred to in the following as a yoke air-gap in a magnetic sense.

Due to this, in total 0.2 mm thin, yoke air-gap in the stator separation plane, harmonic field content is introduced, and the current control needs to be able to counteract resulting induced voltage harmonics.

2.2.2 Rotor Dynamics

To avoid excessive vibration or instabilities of the magnetically levitated rotor, the first (and thus lowest) rotor bending resonance frequency, as shown in Fig. 2.3(b), should be above the maximum frequency of the rotational speed (sub-critical operation). However, higher order synchronous excitations will hit rotor bending modes, and the resulting rotor resonance behavior needs to be stabilized by the control system. The control scheme must furthermore be capable of operating the novel UCF drive system, despite its new unique properties, including yoke air-gaps in the stator magnetic circuit, which is shown in Section 2.4.

Summarizing, specific design is needed both for the motor as described in Section 2.3, Section 2.4, and for the rotor as presented in Section 2.5, the validation is in Section 2.6.

2.3 Slotless Double Self-Bearing Openable Motor

Self-bearing motors (SBMs) have the unique capability of taking over both the driving and magnetic bearing functionality. This simplifies the drive system architecture, as no separate magnetic bearing units are required.

A wide range of SBM applications and accordingly specialized technical solutions are reported in literature. In [20] an overview over the current state of the technology of SBMs with significant power output is provided. A review of the working principles and topologies of SBMs is published in [21].

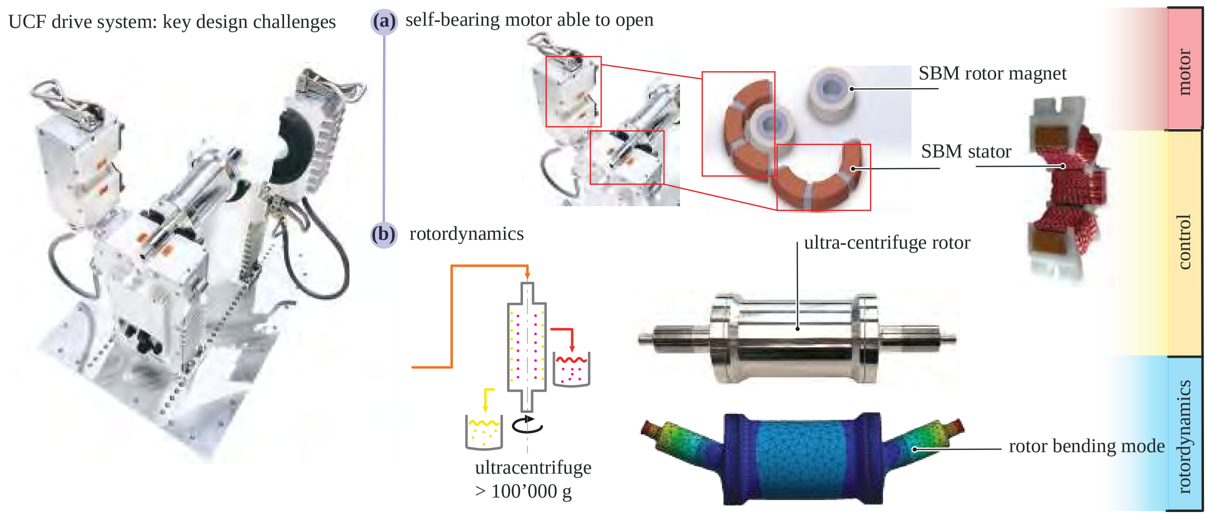

Fig. 2.3: Key design challenges: **(a)** Openable stator for good access to the rotor by UCF operators. Necessary encapsulation of the stator for protection against environmental influences. This leads to unavoidable interruption of the magnetic circuit with corresponding problems for the current-control. **(b)** Rotor design such that the first bending mode can never be excited by frequencies corresponding to the rotational speed.

The field of SBM research is very active. Current trends include reduction of permanent magnet material usage [22] and new SBM topologies to reduce the complexity of the needed power electronics [23]- [24]. Earlier SBMs had typically separate winding sets for bearing force and torque generation. For combined winding topologies as used in this chapter, current research addresses their design and operation [25], optimal current utilization strategies [26] and new parallel winding topologies [27]- [28]. General SBM design-guidelines were recently proposed e.g. in [29]- [30], control strategies are active research topics as well, with e.g. [31] investigating the passing through critical speeds and [32] investigating state observers to improve position control. The field of high-speed SBMs experiences continuous attention with recent publications of systems operating at 30 krpm of [33] and [34], at 60 krpm of [35] and at 100 krpm of [36], [37].

However, to the author's knowledge, the possibility to open high-speed SBM stators in the industrial application by operators, leading to unavoidable yoke air-gaps and their implications on the control, was not reported in literature so far. These aspects are therefore investigated in the following.

2.3.1 Topology for Openable UCF SBMs

For the desired UCF application with openable SBM stators, the topology of slotless SBMs with combined windings in toroidal realization as shown in Fig. 2.4 exhibits several advantages. It allows for the separation of the stator in two separate stator modules.

Furthermore, it leads to a low general and especially rotor loss potential for very high speeds. In contrast, the typical high rotor losses of slotted designs at very high speeds are caused by stronger and higher order harmonics in the air-gap field due to the teeth interaction with the field [38], [39]. Slotless SBMs can exhibit an almost sinusoidal air-gap field for the rotor pole-pair number $p = 1$ [40], which is ideal for highspeed applications with low rotor losses. It results in very low harmonic field content, and $p = 1$ leads to the lowest possible fundamental electrical frequency for a given mechanical speed. This results again in low losses. Therefore, for openable UCF SBMs, a slotless stator topology with rotor pole pair number equal to one is very promising.

In SBMs, drive and bearing currents create fields in the same air-gap. The magnetic bearing forces can either be generated with the aid of separate bearing windings, or with the aid of a mathematical superposition of bearing and drive currents in combined windings, as shown in e.g. [41]. The stator field and related forces acting on the rotor are created by superimposed currents of drive and bearing action, as shown in e.g. [42]. Combined windings for bearing forces and torque generation lead to equal loading of all coils and full utilization of the winding copper cross-section. If the bearing currents were in separate bearing coil sets, this would not be the case. Therefore, also all semiconductors of the connected power electronics benefit from equal current loading. Additionally, in [40] it was shown that the usage of combined windings lowers the higher order field harmonics induced by the stator drive and bearing currents, additionally reducing the current induced losses at high speeds.

In Fig. 2.4(d) the winding scheme of the resulting UCFs SBM topology is presented. It consists of two three-phase systems a and b with phase connections u_a, v_a, w_a and u_b, v_b, w_b respectively. The two three-phase systems are star-connected at the star-points Y_a and Y_b respectively.

To electrically connect the fixed and the movable stator module in Fig. 2.4(c), a flexible cable connection with a high enough bending radius for repeated bending is envisaged Fig. 2.4(d).

2.3.2 Self-Bearing Motor Working Principle

In Fig. 2.4 the working principle for the UCF SBM torque (a) and force generation (b) is shown. For the torque generation, in Fig. 2.4(a), a stator field with the same pole-pair number as the rotor is generated commonly with all six windings. It is 90° ahead of the rotor's permanent magnet field, which leads to maximum torque generation. To create bearing forces as shown in Fig. 2.4(b), the same six windings generate a two-pole pair stator field which generates together with the rotor field bearing forces with controllable amplitude and direction.

2.4 Self-Bearing Motor with Yoke Air-Gaps

Fig. 2.5(a) shows the stator halves with soft magnetic composite (SMC) cores of one of the realized 100 krpm 48 $\mathrm{V_{DC}}$ fed 0.25 kW (each) drive system prototypes of the previously discussed topology for UCF application. The main UCF SBM prototype specifications are listed in Tab. 2.2 and the used materials of the prototype in Tab. 2.3.

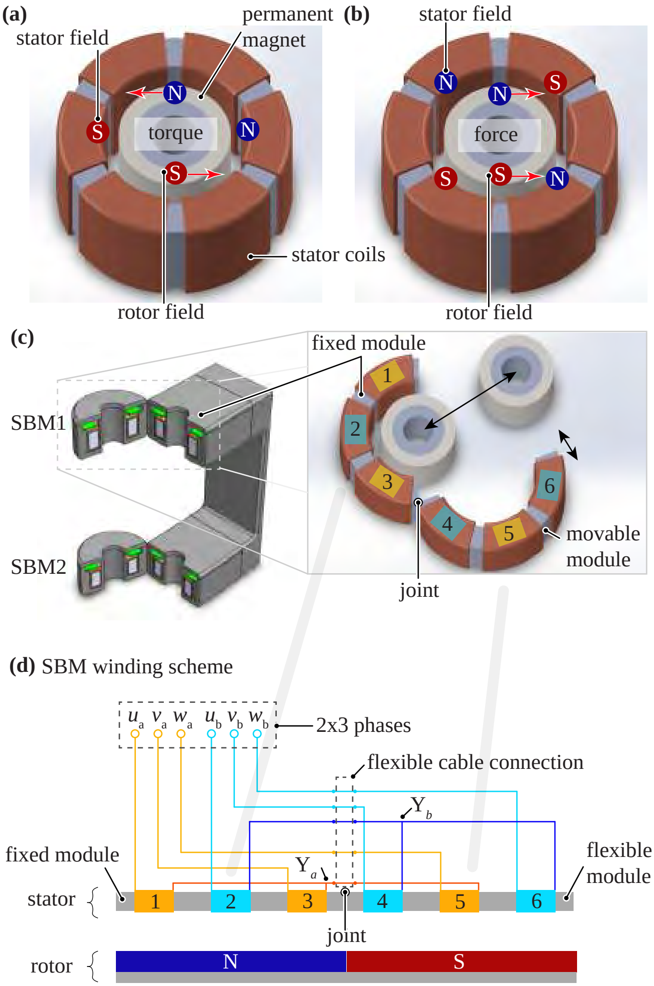

Fig. 2.4: From [18]: working principle of the slotless SBMs: **(a)** driving torque, and **(b)** bearing force generation. **(c)** Possibility to open the stators of the proposed UCF SBMs enabling access and removal of the UCF rotor. **(d)** SBM winding scheme of the proposed topology.

2.4.1 Yoke Air-Gap Induced Flux Variation

In Fig. 2.5(b) a 3D-FEM electromagnetic simulation of the magnetic flux density is shown. The yoke air-gaps introduce harmonic field content as shown in Fig. 2.5(b1)-(b2), due to reduced reluctance for $\varphi = \{0,\ \pi\}$ with no flux crossing over the yoke air-gaps, and increased reluctance with flux crossing over the yoke air-gap for $\varphi = \{\pi/2,\ -\pi/2\}$.

The resulting linked rotor permanent magnet fluxes $\phi_1 - \phi_6$ in the six coils (per turn) are shown in Fig. 2.5(c). The center coils 2 and 5 of the stator limbs experience a slightly higher flux amplitude increased by ϕ_Δ. The flux in each phase can therefore be stated as:

$$\begin{aligned} \phi_\mathrm{u}(t) &= \left(\hat{\phi} + \phi_\Delta\right) \cdot \cos\left(p\Omega t\right) \\ \phi_\mathrm{v}(t) &= \hat{\phi} \cdot \cos\left(p\Omega t - \frac{2\pi}{3}\right) \\ \phi_\mathrm{w}(t) &= \hat{\phi} \cdot \cos\left(p\Omega t + \frac{2\pi}{3}\right), \end{aligned} \tag{2.1}$$

where Ω stands for the rotational speed.

Fig. 2.5(d) shows the dq-transformed fluxes. Both d- and q-flux show a second harmonic flux variation with approx. 4 % of the d-flux amplitude, as also analytically can be shown by applying the dq-transform on the previous equations, on the one hand for the d-component:

$$\begin{aligned} \frac{3}{2}\phi_\mathrm{d}(t) &= \frac{3}{2}\hat{\phi} + \phi_\Delta \cdot \cos^2\left(p\Omega t\right) \\ &= \frac{3}{2}\hat{\phi} + \frac{1}{2}\phi_\Delta + \frac{1}{2}\phi_\Delta \cdot \cos\left(2p\Omega t\right) \end{aligned} \tag{2.2}$$

and similarly for the q-component:

$$\begin{aligned} \frac{3}{2}\phi_\mathrm{q}(t) &= \phi_\Delta \cdot \cos\left(p\Omega t\right) \cdot \sin\left(p\Omega t\right) \\ &= -\frac{1}{2}\phi_\Delta \cdot \sin\left(2p\Omega t\right) \\ &= \frac{1}{2}\phi_\Delta \cdot \cos\left(2p\Omega t - \frac{\pi}{2}\right). \end{aligned} \tag{2.3}$$

By extracting the time-varying parts of the dq-fluxes $\phi_{\mathrm{d},\Delta}(t)$ and $\phi_{\mathrm{q},\Delta}(t)$:

$$\begin{aligned} \phi_{\mathrm{d},\Delta}(t) &= \frac{1}{3}\phi_\Delta \cdot \cos\left(2p\Omega t\right) \\ \phi_{\mathrm{q},\Delta}(t) &= \frac{1}{3}\phi_\Delta \cdot \cos\left(2p\Omega t - \frac{\pi}{2}\right), \end{aligned} \tag{2.4}$$

it is revealed that these time varying components both share the same amplitude, and show the same twofold frequency compared to the rotational speed Ω. They create a 2D-circle in the dq-plane. The same result can be seen by transforming the 3D-FEM obtained fluxes to the dq-plane. It leads to a rotating flux variation space vector $\underline{\phi}_{\Delta}$, presented in Fig. 2.5(e).

In the following, the implications, problems and a solution to the discovered flux variation in SBMs with yoke air-gaps are unveiled. The presented current-control solution is also realized in the hardware prototype.

2.4.2 Parasitic Induced Rotating Current and L-Filter Impact

The separation of the stator into two halves for the stator opening-functionality leads to a parasitic magnetic flux variation. It shows three times the rotational frequency in the stationary frame of reference, and in the moving dq-frame of reference two times the rotational frequency. This leads to an induced voltage space vector $\underline{U}_{\mathrm{g}}$ of corresponding frequency. An equivalent circuit of the stator incorporating $\underline{U}_{\mathrm{g}}$ is shown in Fig. 2.7(a).

The parasitic induced voltage amplitude $|\underline{U}_{\mathrm{g}}|$ can be written as:

$$|\underline{U}_{\mathrm{g}}| = p \cdot N \cdot \phi_{\Delta} \cdot \Omega. \tag{2.5}$$

Without further measures, $\underline{U}_{\mathrm{g}}$ leads to a parasitic current space vector $\underline{I}_{\mathrm{g}}$ rotating with the same frequency as $\underline{U}_{\mathrm{g}}$ as shown in the space vector diagram Fig. 2.7(b). $\underline{U}_{\mathrm{g}}$ therefore leads to parasitic d- and q-currents. In the space vector diagram, the voltage drop across the stator resistance R_{S} is neglected, as for high efficiency motors $|\underline{U}_{\mathrm{p}}| >> |\underline{U}_{\mathrm{R}}|$. The parasitic current amplitude $|\underline{I}_{\mathrm{g}}|$ calculates as:

$$|\underline{I}_{\mathrm{g}}| = \frac{p \cdot N \cdot \phi_{\Delta} \cdot \Omega}{\sqrt{R_{\mathrm{s}}^2 + (3\Omega)^2 \cdot L_{\mathrm{d}}^2}}. \tag{2.6}$$

At low rotational speeds, its amplitude $|\underline{I}_{\mathrm{g}}|$ is limited by the stator resistance R_{S} to an initially linear rise with the speed. At high speeds, it is limited by the motor inductance L_{d} (rotor is non-salient, i.e. L_{d}=L_{q}) consisting of an optional phase L-filter inductance L_{f} and the stator synchronous inductance L_{S}, with $L_{\mathrm{d}} = L_{\mathrm{F}} + L_{\mathrm{S}}$

$$|\underline{I}_{\mathrm{g}}| = \frac{p \cdot N \cdot \phi_{\Delta} \cdot \Omega}{\sqrt{R_{\mathrm{s}}^2 + (3\Omega)^2 \cdot (L_{\mathrm{F}} + L_{\mathrm{S}})^2}}. \tag{2.7}$$

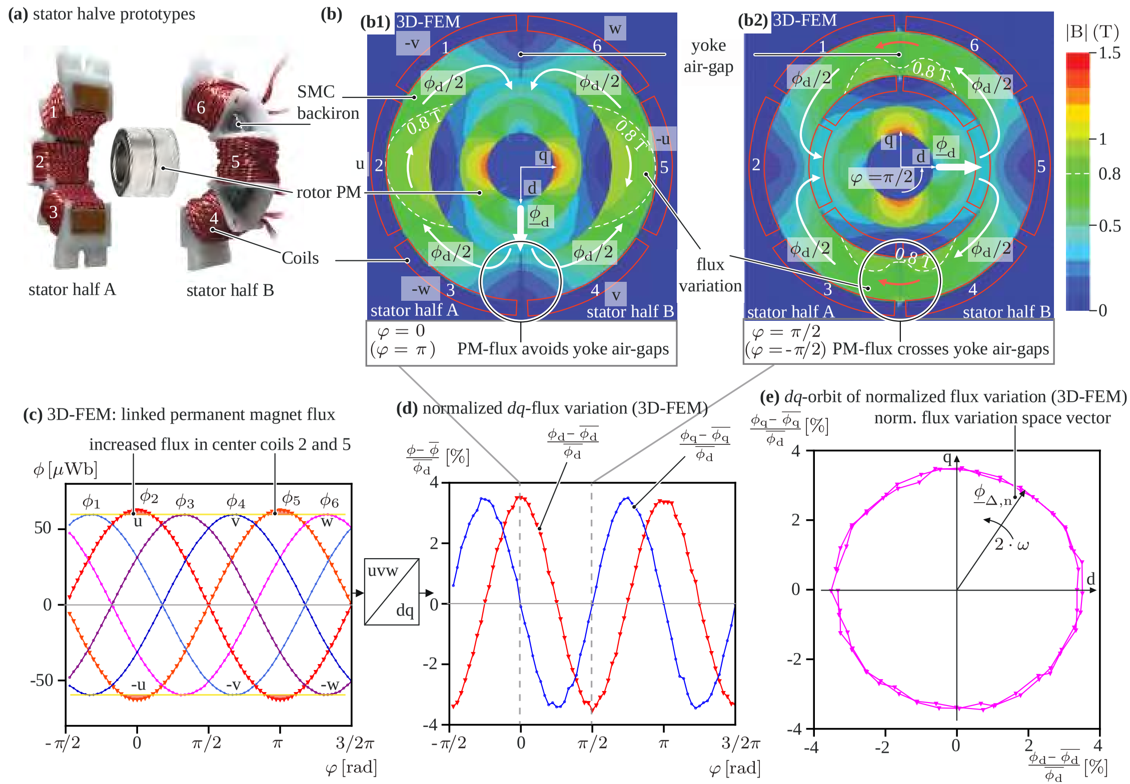

Fig. 2.5: (a) Stator of the realized double self-bearing slotless openable motor prototype. **(b)** 3D-FEM magnetic field simulation of the prototype motors. Thin yoke air-gaps for durable anti corrosion coating (0.1 mm on each side) in the separation plane. Resulting yoke air-gap introduced harmonic field content **(b1)-(b2)**, due to increased reluctance and flux crossing for $\varphi = 0, \pi$ and reduced reluctance for $\varphi = \pi/2, -\pi/2$. **(c)** Resulting linked rotor permanent magnet fluxes $\phi_1 - \phi_6$ in the six coils (per turn). **(d)** Transformed to dq-quantities, both d- and q-flux show a second harmonic flux variation with approx. 4 % of the d-flux amplitude. **(e)** In dq-plane this leads to a rotating flux variation space vector.

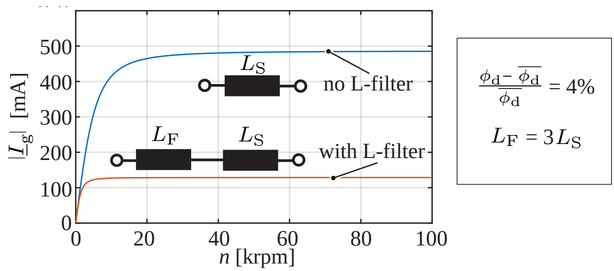

Fig. 2.6: Analytically calculated parasitic current amplitude $|\underline{I}_g|$ for the self-bearing motors of this chapter given a relative flux variation w.r.t. the d-flux amplitude of 4 % once without L-filter and once with a filter inductance of $L_F = 3 \cdot L_S$.

For high speeds, the parasitic current amplitude $|\underline{I}_g|$ tends asymptotically towards the finite value $|\underline{I}_{g,lim}|$:

$$|\underline{I}_{g,lim}| = \frac{p \cdot N \cdot \phi_\Delta}{3\,(\cdot L_F + L_S)}\ . \tag{2.8}$$

If the stator winding synchronous inductance L_S is very low, as it is usually the case with high-speed motors, the parasitic current amplitude $|\underline{I}_g|$ can assume large values without additional filter inductances L_F.

Fig. 2.6 shows for the UCF SBMs of this chapter the analytically calculated parasitic current amplitude $|\underline{I}_g|$ based on (2.7) for a relative flux variation w.r.t. the d-flux amplitude of 4 %. It is shown once without L-filter and once with a filter inductance of $L_F = 3 \cdot L_S$. It should be noted, that in the shown 3D-FEM simulation in Fig. 2.5(b), a perfectly manufactured yoke air-gap geometry is assumed. In a real hardware, especially for SMC stator material, the stator edges are imperfect, or need to be rounded slightly, thus increasing the effective yoke air-gap and therefore also the parasitic induced currents $\underline{I}_g$, especially for small motors where the non-ideal edge geometry has an even larger influence.

2.4.3 Yoke Air-Gap Design

To allow the opening of the SBMs by the industrial operators, the stators are separated in two halves. Necessary protective coating leads unavoidably to at least two yoke air-gaps.

From a magnetic standpoint, it seems attractive to place three yoke air-gaps offset by 120° each to achieve a symmetry w.r.t. the three-phase winding.

However, the cost and complexity of an industrial system with three stator units, each of them encapsulated and connected by shielded cables leads to the preference of only one separation plane. Additionally, each introduced air-gap increases the unwanted stator reluctance.

The yoke air-gaps should be kept as thin as possible, to reduce adverse effects. However, appropriate durable coating for an industrial environment will always require a certain thickness.

To further reduce the effect of the yoke air-gap between the stator halves, geometric measures are conceivable in the future. On the one hand, the area over which the magnetic flux is transmitted between the stator halves could be increased. On the other hand, if not all coils require the same number of turns for production reasons, the middle coil of each stator segment can have a slightly lower number of turns in order to have the same amount of linked flux in all coils. However, an exact matching, also due to tolerances, seems unlikely. Therefore a current control strategy is always needed.

2.4.4 Adverse Effects of Parasitic Induced Rotating Current

The parasitic induced current $\underline{I}_{\mathrm{g}}$ generates a parasitic stator field with pole pair number $p = 1$, rotating with a frequency of $3 \cdot \Omega$ in the stator frame of reference, i.e. an asynchronous field. The self-bearing motors of this chapter generate bearing fields with number of bearing poles $P_{\mathrm{bng}} = P_{\mathrm{drv}} + 2 = p \cdot 2 + 2 = 4$. They are therefore according to [43] of type $P_{\mathrm{bng}} = P_{\mathrm{drv}} \pm 2$. This implies, that the parasitic field cannot generate parasitic bearing forces. However parasitic torque ripple $\hat{T}_{\mathrm{Ig}}$ of the frequency $2 \cdot \Omega$ is generated. The resulting speed ripple amplitude $\hat{\Omega}_{\mathrm{Ig}}$ is kept limited by the rotor inertia J as $\dot{\Omega} = T/J$ and increasingly attenuated with increasing speed Ω by the PI-speed control with low-pass closed-loop characteristic. For the envisaged UCF application, the speed ripple should be as small as possible to avoid re-mixing of the separated media.

$\underline{I}_{\mathrm{g}}$ furthermore creates additional parasitic motor losses. On the one hand, $\underline{I}_{\mathrm{g}}$ causes additional SMC stator core and rotor losses due to the asynchronous parasitic stator field (with an angular frequency of $3 \cdot \Omega$ in the stator frame of reference). On the other hand, additional copper losses in the windings are generated.

Compared to the rotor PM-field, the parasitic stator field is of less strength, but its threefold frequency of $3 \cdot \Omega$ implies, that SMC core loss terms from the Steinmetz equation [44] with quadratic frequency dependence are multiplied by $9 \cdot \Omega^2$. Furthermore the parasitic field is superimposed to the rotor PM-field and the stator fields for torque and bearing force generation. Thus, the parasitic field is added on top, increasing the loss generation potential, as the core losses are non-linear with the flux density and sensitive to field bias [45]. A detailed investigation of the complex mechanisms of this loss generation would go beyond the scope of this chapter and may be subject of future work. This chapter focuses instead on the root cause of $\underline{I}_\mathrm{g}$ and presents and experimentally validates a first approach to mitigate it.

2.4.5 Yoke Air-Gap Parasitic Current Feed-Forward Control

A voltage compensation by feed-forward control of the parasitic induced voltage $\underline{U}_\mathrm{g}$ on the nominal applied stator voltage $\underline{U}_\mathrm{s,nom}$ is proposed as shown in Fig. 2.7(c) and implemented on the presented prototype. The corresponding control circuit diagram is shown in Fig. 2.8.

With the presented voltage feed-forward current control strategy, the adverse effects of the yoke air-gaps can be counteracted.

2.5 Rotor Dynamics

The conceptual feasibility of an UCF rotor for the drive system presented in this chapter was shown in [18]. The continuing step from concept to prototype taken in this chapter requires an investigation of the rotordynamics behavior of the actual design.

Compared to the rotor stiffness, the magnetic bearing stiffness is very small. Therefore, as an analytic approximation for the bending modes, the unsupported free vibration of a Euler-Bernoulli beam can be applied. The first bending mode resonance frequency $f_\mathrm{res,1}$ of a freely vibrating Euler-Bernoulli beam according to [46] is

$$f_\mathrm{res,1} = \frac{22.37}{2\pi L^2}\sqrt{\frac{E \cdot I_x}{\rho \cdot A}}\,, \tag{2.9}$$

with the length L, Young's modulus E, second moment of area I_x, density ρ and cross-section A. The rotor is modeled as an annulus with inner and outer radii r_1 and r_2 and thickness $t = r_2 - r_1$. With the second moment of area I_x of

$$I_x = \frac{\pi}{4}(r_2^4 - r_1^4)\,, \tag{2.10}$$

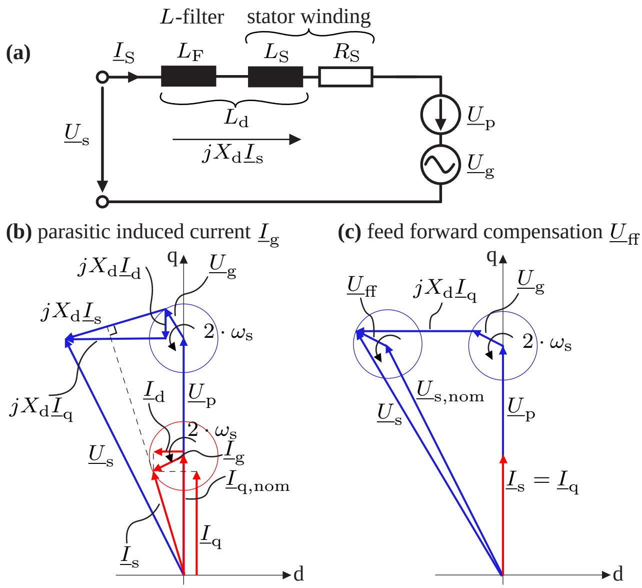

Fig. 2.7: **(a)** Stator equivalent electric circuit with parasitic induced voltage $\underline{U}_g$ due to yoke-air-gap flux variation. **(b)** Space vector diagram with resulting current harmonics $\underline{I}_g$. **(c)** Proposed feed-forward voltage space vector $\underline{U}_{ff}$ compensation.

$f_{res,1}$ can be rewritten as

$$f_{res,1} = \frac{22.37}{2\pi L^2}\sqrt{\frac{E}{\rho} \cdot \frac{(r_1 + t)^2 + r_1^2}{4}}\,. \tag{2.11}$$

To achieve a high $f_{res,1}$, a short rotor length L, high Young's modulus E, low density ρ, large inner radius r_1 and large thickness t (for given r_1) are beneficial. Therefore these parameters can be varied and the rotor material chosen accordingly, in alignment with the rotor strength and air friction power consumption constraints, as shown in [18]. Knowing these influences, 3D-FEM rotor dynamics simulations can be performed in iterative manner until the desired $f_{res,1}$ is achieved.

Within the scope of this chapter, two rotor designs were investigated. On the one hand, a test rotor shown in Fig. 2.9(a1) was designed to verify the drive system with respect to magnetically self-bearing and drive functionality. On the other hand, an UCF rotor prototype displayed in Fig. 2.9(a2) was designed

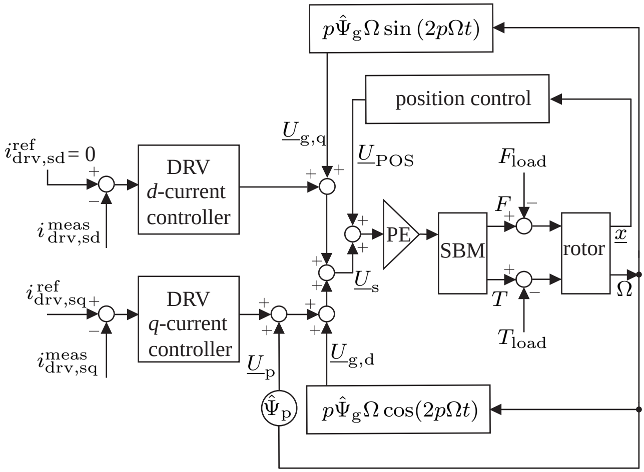

Fig. 2.8: Proposed current control scheme for the self-bearing openable motors with feed-forward control of the parasitic induced voltage $\underline{U}_g$. The power electronics (PE) apply the resulting voltages from drive current-control and position-control to the combined windings of the SBMs.

to prove that the rotordynamic UCF requirements can be fulfilled. The rotor dimensions of both rotors are specified in Tab. 2.4.

For this purpose, 3D-FEM rotor dynamic simulations of the rotor bending modes were performed for both rotors and presented in Campbell diagrams in Fig. 2.9(b1) and Fig. 2.9(b2) respectively. For both rotors, in the speed operating range, the first bending resonance is above the synchronous first-order excitations (EO = 1) and thus, it is not excited by them during operation. Excitations of higher order (EO > 1) can in principle excite bending modes if they hit their resonance frequency (critical frequencies). However, successful run-up tests in Section 2.6 show that these critical frequencies can be passed with the present drive system. Due to the larger rotor diameter compared to the test rotor, the UCF rotor has a higher stiffness and a large reserve with respect to separation of EO = 1 and the first bending resonance. To verify the 3D-FEM results, the test rotor was struck with a mechanical impulse while resting stationarily and the acoustic frequency response was measured with a microphone as described in [47] and is shown in Fig. 2.9(c). The provided normalized sound pressure levels p_{rel} are normalized by $p_0 = 20\ \mu$Pa (calibrated at 400 Hz with the sound pressure level measurement unit of [48]).

The resonance frequencies determined acoustically and with 3D-FEM agree well, although the deviation is greater for the higher second bending mode. This can be due to the fact, that in the simulation all rotor components were modeled as firmly bonded, resulting in higher stiffness and lower damping than in the prototype with glued components. Thus, the 3D-FEM bending mode simulation was verified acoustically by experiment.

2.6 103 krpm Drive-System Test-Operation

The UCF drive system presented in this chapter was successfully commissioned and operated at a speed of 103 krpm with the test-rotor. Thus, the target speed of 100 krpm was reached.

In Section 2.4.2 the appearance of parasitic induced currents due to the yoke air-gaps was predicted with the aid of 3D-FEM and analytic derivations. The experimental confirmation thereof is shown in Fig. 2.10. In Section 2.4.5 a feed-forward control compensation was proposed. Its effectiveness is experimentally shown in Fig. 2.10. Despite the application of $L-$filters, the parasitic current was found with an amplitude of approx. 0.8 A at 30 krpm to be higher then expected from the FEM-simulations (> 10% of the nominal UCF operation drive current $\hat{I}_{\mathrm{q,nom}}$). This can be a consequence of the non-ideal geometry of the brittle SMC cores with broken off edges, making the interface area between the two core halves smaller then in the ideal simulation geometry. The manufacturing process should therefore be improved in the future. Fig. 2.10 further shows the achieved reduction of the parasitic currents by approx. 70 % with the proposed feed-forward control scheme. Tuning of the feed-forward gain while running levitated at 30 krpm as shown in Fig. 2.10 allowed to find the optimal gain.

The measured parasitic current amplitude of 0.8 A at 30 krpm leads to a 3D-FEM obtained cross-section average parasitic stator-core flux density component amplitude of 20 mT. The appearance of resulting parasitic current induced loss is proven by measurement. The increase in steady state motor temperature for varying the feed-forward compensation gain from full (100%) to zero and negative compensation (−33%) is shown in Fig. 2.11 at 20 krpm and 25 krpm. It was found as predicted, that the relative motor temperature, and therefore the parasitic motor loss, grows on the one hand with reduced feed-forward compensation, and on the other hand with increasing speed.

The non-linear growth of the parasitic motor losses with speed as discussed in Section 2.4.4 implies the necessity for this 100 krpm self-bearing motors to compensate the parasitic currents.

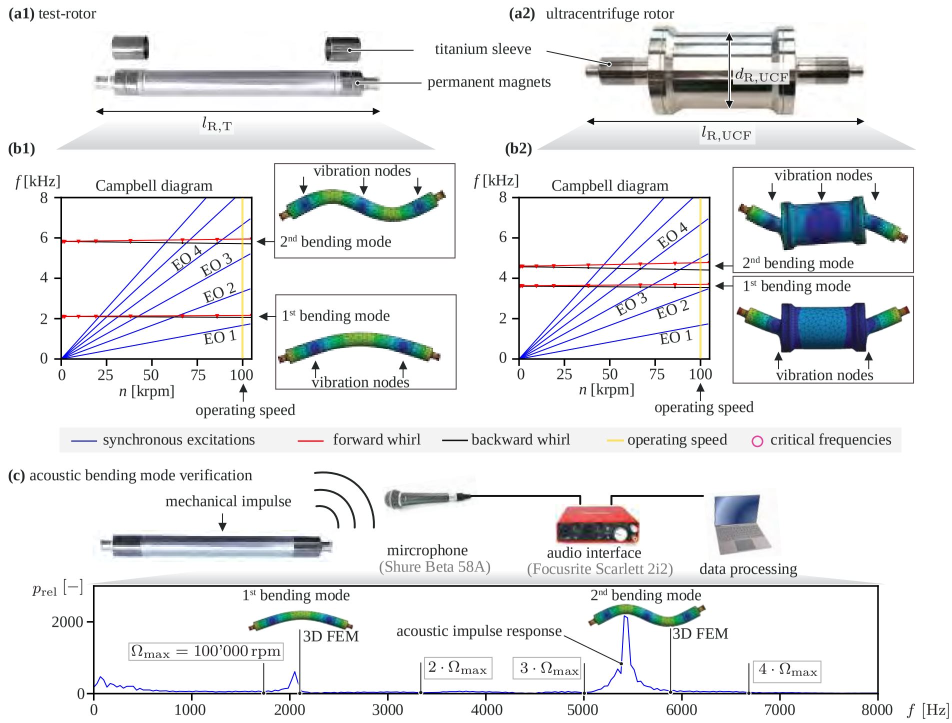

Fig. 2.9: (a1) Test-rotor and **(a2)** UCF rotor. **(b1)-(b2)** Corresponding 3D-FEM obtained Campbell diagrams with rotor bending modes. For both rotors, the synchronous excitation with excitation order (EO) equal to one has no intersection with the first bending mode, suggesting the absence of major vibration problems. **(c)** Acoustic impulse response measurement validation of the test-rotor bending resonance frequencies. The indicated rotor dimensions are specified in Tab. 2.4.

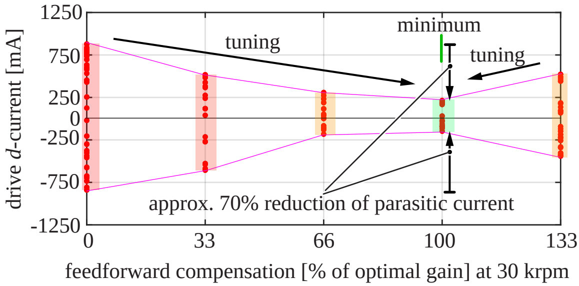

Fig. 2.10: Tuning of the parasitic induced voltage feedforward compensation gain conducted at 30 krpm and achieved drastic reduction of the parasitic currents.

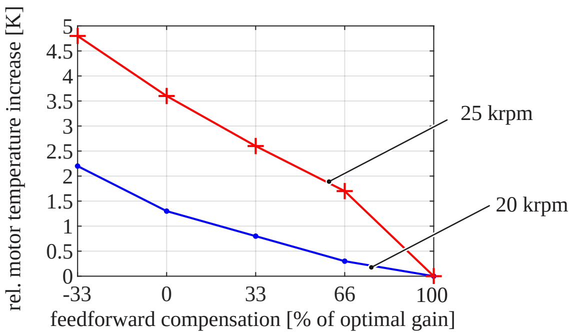

Fig. 2.11: Relative motor temperature increase for different parasitic induced voltage feed-forward compensation levels (from negative to full compensation) and two speed levels, 20 krpm and 25 krpm.

With the aid of the L−filter and the proposed feed-forward control method it was achieved to reduce the parasitic currents to an acceptable level despite non-ideal stator core manufacturing. With the mechanisms of the generation of the parasitic currents unveiled in this chapter, the doors are open to test or combine other control methods to counteract the parasitic currents. Work being reported for current regulators in active filters as reviewed in e.g. [49] could be a starting point for future investigations. Fig. 2.12 shows an oscilloscope screenshot of the rotor angle sensor signal measurement at 103 krpm. Since the rotor has one pole-pair, the fundamental frequency of the shown wave-form of 1.73 kHz corresponds to 103 krpm.

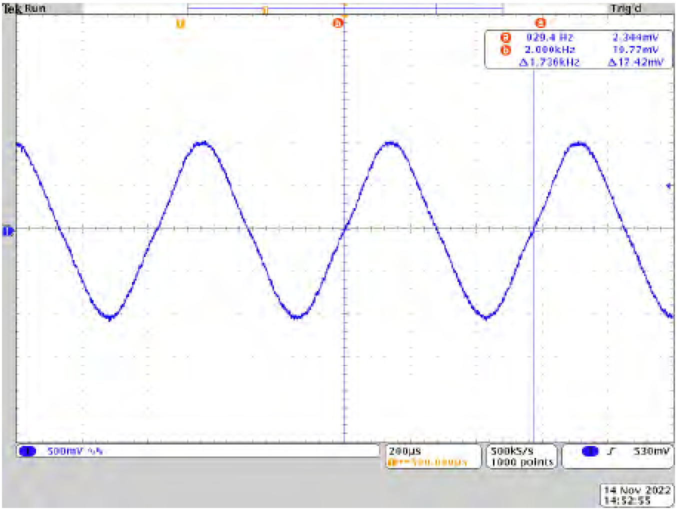

Fig. 2.12: Oscilloscope measurement of the rotor angle sensor signal (rotor number of pole pairs equal to one), as a proof of the system operation at 103 krpm.

Having reached the target speed, implies that the critical frequencies due to higher order excitations (EO > 1) were successfully passed. Fig. 2.13 shows the radial displacement waveforms over one rotor-revolution of the rotor angle ϑ. While at 10 krpm some rotor vibrations are visible in Fig. 2.13(a), at 100 krpm in Fig. 2.13(b) the rotor is extremely steady. Fig. 2.13(c) shows the average radial displacement radius $|\underline{x}_r|_{avg}$ for a speed run-up from 10 – 100 krpm. Crossings of higher order excitations (EO > 1) with the test-rotor bending-modes resulted in visible displacement radius peaks. However, these zones can be successfully passed with the prototype. For unrestricted long-term operation, rotor orbit radii are recommended according to standard [50] to be smaller than 30% – 40% of the minimal rotor-stator clearance. With 600 μm clearance, the average rotor orbit radius during speed ramp-up $|\underline{x}_r|_{avg}$ in Fig. 2.13(c) was at resonances always below 12% of the clearance. At the envisaged operating point of 100 krpm it was below 1%. Therefore, this recommendation is met and the rotor vibrations sufficiently damped over the whole operating range and the drive system successfully experimentally validated.

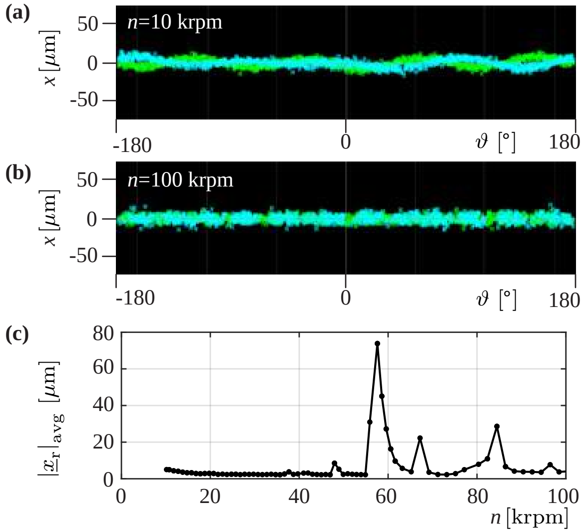

Fig. 2.13: Radial rotor displacements of both self-bearing motors over one rotor-revolution **(a)** at 10 krpm and **(b)** at 100 krpm. **(c)** Averaged radial displacement amplitude during a speed ramp-up.

2.7 Conclusion & Outlook

The novel magnetically double self-bearing drive system concept for ultra-centrifugation with stator opening functionality for easy rotor removal and performance specifications of 100 krpm and 200′000 g introduced by the author in [18] was realized as a prototype. The needed stator encapsulations provoked stator yoke air-gaps were found to lead to parasitic currents if not controlled accordingly. The usage of $L-$filters and a voltage feed-forward current control-strategy to diminish these effects was proposed and successfully implemented and tested on the newly built prototype. The working of the novel self-bearing openable stator drive-system was experimentally verified. Future work will focus on operating the system in UCF separation-mode, continuing the path towards 200′000 g.

Tab. 2.1: System Dimensions.

Dimension	Variable	Value
System length	l_S	340 mm
System width	w_S	260 mm
System height in closed state	$h_{S,c}$	227 mm
System height in opened state	$h_{S,o}$	260 mm

Tab. 2.2: SBM Prototype Specifications.

Dimension	Variable	Value
Number of pole pairs	p	1
Number of phases	m_S	6
DC-Link voltage	U_{DC}	48 V
Design max. power per SBM	P_{max}	0.25 kW
Stator synchronous inductance	L_S	36 μH
Phase filter inductance	L_F	100 μH

Tab. 2.3: Drive-System Prototype Materials.

Component	Material
Stator yoke	SMC
Rotor PM	NdFeB
Rotor bodies	EN AW-7075 (AlZnMgCu1,5)
Rotor sleeve	Titanium

Tab. 2.4: Rotor Dimensions.

Dimension	Variable	Value
Test-rotor length	$l_{R,T}$	202 mm
Ultracentrifuge diameter	$d_{R,UCF}$	50 mm
Ultracentrifuge length	$l_{R,UCF}$	202 mm

3

Sealless Production Ultracentrifuge and its Openable Self-Bearing Motors

This chapter summarizes the most relevant findings regarding the concept, design and realization of a sealles production ultracentrifuge and its openable self-bearing motors, which are also published in:

- **E.J. Hubmann**, D. Steinert, T. Nussbaumer and J.W. Kolar, "Sealless Production Ultracentrifuge and its Magnetically Self-Bearing Openable Motors for Purification in Viral Nanotechnology," *IEEE Access (Early Access),* January 2025.

Chapter Abstract

Viral nanotechnology enables new possibilities for gene therapies and vaccines. However, the manufacturing of viral vectors lacks a satisfactory production capable method for purification of full capsids. Empty or partially empty capsids need to be removed to avoid immunotoxicity. The state of the art production ultracentrifuges (PUCFs) are limited, especially in rotational speed to approximately 40 krpm by rotary seals, by complexity and virus containment. This prevents PUCFs from widespread use in industry for viral vector production. This chapter proposes a novel PUCF type with rotational speed potential towards 100 krpm with a hermetically enclosed process chamber without any rotary seals, i.e. a sealless production ultracentrifuge (SL-PUCF) omitting contamination risk. The openable vertical axis self-bearing motors, the novel sealless flow path design and the needed ultra high-speed potential towards 100 krpm pose new technical problems, for which this chapter proposes and experimentally validates solutions. A SL-PUCF prototype with its vertical axis magnetically self-bearing openable motors (O-SBMs) and openable burst armor (O-BA) are realized, validated and operated as a system. The general working principle of the SL-PUCF system is experimentally validated by whey protein sedimentation. Furthermore, new future smart capability potential of the proposed new SL-PUCF technology suspended and driven by O-SBMs is unveiled as an outlook and examples shown in case studies.

3.1 Introduction

This chapter presents a novel sealless production ultracentrifuge (SL-PUCF) concept and prototype with a fast exchangeable rotor for viral nanotechnology, shown in Fig.3.1. It solves newly identified key problems of the state of the art PUCFs, preventing them currently from broad industry usage in viral nanotechnology. The novel SL-PUCF enables a novel hermetically enclosed sealless vertical axis SL-PUCF rotor, because it is driven and suspended by novel openable magnetically self-bearing motors (O-SBMs) and shielded by a novel openable burst armor (O-BA). This omits contamination risk due to rotary seals. This chapter is a continuation of the research efforts of [18], where to the knowledge of the author for the first time, the principle of O-SBMS was experimentally demonstrated. In the following, the gap in the state of the art is identified.

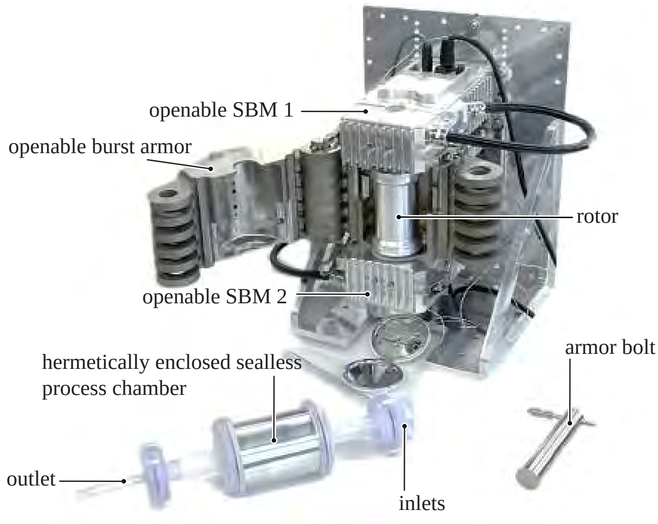

Fig. 3.1: Realized system prototype of a novel lab-scale sealless production ultracentrifuge (SL-PUCF). Two openable self-bearing motors (O-SBMs) suspend and drive the vertical axis SL-PUCF rotor. The O-SBMs and an openable burst armor (O-BA) allow for fast exchange of the hermetically enclosed SL-PUCF process chamber including the rotor.

Viral nanotechnology enables new vaccines [51], [52] and gene therapies for previously incurable genetic diseases [53]. Gene transfer via viral vectors is one possible approach, which is considered in this chapter. The viral vector production process simplified from [2] is as follows: After cell cultivation for viral vectors, the so-called downstream process follows. In the downstream process, the viruses are harvested from the supernatant of the cell culture and from the cells themselves by cell lysis. In the subsequent clarification, producer cells and cell debris are eliminated. This is followed by concentration steps that reduce the equipment size required for further processing. During subsequent purification, contaminants are removed as good as possible. In the next polishing steps, impurities and very closely related species are removed as far as possible. Formulation, sterile filtration, fill and finish conclude the production process.

Remaining impurities and very closely related species lead to unnecessary immune reaction [2], negatively affecting the therapy. For viral vector production, extremely high degrees of purity therefore have to be achieved. For this reason, purification is an absolutely critical production step.

In laboratory scale intended for research (LaS-R), it is state of the art to use laboratory scale research centrifuges (LaS-RCF) for clarification and concentration, and laboratory scale research ultracentrifuges (LaS-RUCF) for purification and polishing with excellent results [2]. However, RUCFs are not suited for up-scaling of a biopharmaceutical production process, as everything is tailored to small limited discrete process volumes.

Fig.3.2(a1) shows a schematic illustration of a typical state of the art PUCF. Mechanical bearings suspend the rotor, and rotary seals aim to maintain the process chamber contamination barrier during the process. An electric motor in the top assembly drives the rotor. To replace the rotor, it is lifted with the top assembly, causing the loss of the contamination barrier, and thus sterility, as shown in Fig.3.2(a2). The proposed SL-PUCF concept of this chapter is illustrated in Fig.3.2(b1), providing a hermetically enclosed process chamber by replacing rotary seals and mechanical bearings by two O-SBMs. The capability of the O-SBMs, to radially open and give way to insert or remove the whole process chamber including the rotor contained insid, allows for exchanging the rotor after a batch without loss of the contamination barrier, as shown in Fig.3.2(b2).

An overview of the current state of the art PUCFs is presented in Tab.3.1. The current state of the art offers PUCFs in the lab- (LaS-PUCF), pilot- (PiS-PUCF), and production scale (PrS-PUCF) for stepwise up-scaling of the industrial pharmaceutic production process. The number of PUCF manufacturers and PUCF products is very limited. Partially, the commercial products are based on many decades old technology. Mostly mechanical bearings are employed, requiring the application of rotary seals between rotor and housing. A new effort towards application of contact free magnetic bearings for PUCFs is reported for nano-particles in [17], however its stators cannot open radially to release the rotor. The system needs to be disassembled axially to remove the rotor, resulting in a loss of the contamination barrier, which would be a problem in applying it for biopharmaceutical applications. The rotors for biopharmaceutical PUCFs are in contrast to [17] oriented vertically. The relative centrifugal acceleration of state of the art PUCFs is limited around $C_{\mathrm{max}} = 120'000\,\mathrm{g}$.

In Tab.3.2, a summary of limitations and disadvantages of the state of the art PUCFs is given. Such limitations prevent their widespread use in viral vector production. The problems from the application perspective are unveiled in Tab.3.2(A) and the technical reasons identified in Tab.3.2(B). The scale up from LaS-RUCF to PrS-PUCF poses therefore unsolved problems. PrS-PUCFs are thus rarely used in the production scale.

Tab. 3.1: Production Ultracentrifuges (PUCFs): state of the art, and design specifications of the presented prototype of this chapter.

Scale	**Company** / *Publication*	**Product**	**Year**	**Bearing**	**Axis**	$d_{fl,a}$ **[mm]**	Ω_{max} **[rpm]**	C_{max} **[g]**	V **[mL]**	**Applications**
LaS-PUCF	Alfa Wassermann	Promatix 1000 [54]	2006	mech.	v	*132	35000	90500	55-230	viruses, VLP, VV
PiS-PUCF	Alfa Wassermann	PKII [54]	(-)	mech.	v	130	40500	121000	-4000	viruses, VLP, VV
PrS-PUCF	Alfa Wassermann	KII [54]	1975	mech.	v	130	40500	121000	-8400	viruses, VLP, VV
PiS-PUCF	Thermo Fisher Scientific	Sorvall CC40SNX	(-)	mech.	v	132	40000	118000	1600	viruses, proteins
PrS-PUCF	Thermo Fisher Scientific	Sorvall CC40NX	(-)	mech.	v	132	40000	98000	8000	viruses, proteins
LaS-PUCF	CEPA	Z11	2014	mech.	v	*49	54000	80000	250	nano-LDH [55]
LaS-PUCF	*Konrath et. al, CEPA, EAAT*	*Research Prototype*	2016	DSBM	h	43	app. 64500	100000	270	nano-particles [17]
LaS-PUCF	*Hubmann et. al (this chapter)*	*Research Prototype*	2024	O-DSBM	v	40	100000	223500	100	viral vectors (VV)

$^*x$: calculated quantity, (-): no information available, mech.: mechanical, v: vertical, h: horizontal.

LaS: lab scale, PiS: pilot scale, PrS: production scale, $d_{fl,a}$: outer fluid diameter in rotor, C_{max}: maximal centrifugal acceleration, V: rotor volume, VLP: virus like particle, VV: viral vector

Tab. 3.2: (A) Limitations of state of the art PUCF products for viral vector production, suspected by literature and the author to be the cause to prevent them from broader usage. **(B)** Technical reasons and **(C)** newly defined system level requirements for the novel proposed SL-PUCF concept.

(A) State of the art: problems from an application perspective	**(B) Technical reasons**	**(C) Newly defined technical system level requirements**
(1) non-zero risk for infectious virus containing aerosols [2], [5]	rotary seals as weak points of contamination barrier	hermetic virus containment (no seals)
(2) complex rotor insertion and removal	mechanical bearings, lubrication, vibration dampers, crane for rotor removal	radially openable magnetically self-bearing motors (O-SBMs) and burst armor allowing for hermetically contained rotor unit exchange
(3) complex cleaning in place (CIP)	system complexity	rotor removable while hermetically contained
(4) non-zero contamination risk from outside	rotary seals as weak points in contamination barrier	pre-sterilized, hermetically enclosed units can be exchanged
(5) long processing times [2]	rotary seals limit rotational speed	no seals, no mechanical bearings
(6) very limited number of production-scale systems [2] (Alfa Wassermann K-types, Thermo Fischer Scientific Sorvall CC40NX series)	presumption: system complexity	lower complexity, smaller entry hurdle

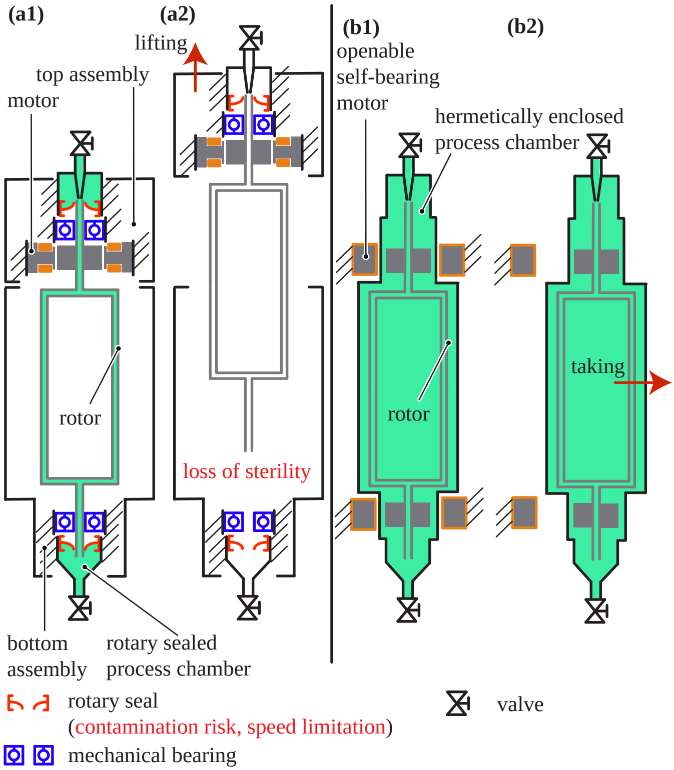

Fig. 3.2: (a1) Schematic illustration of a state of the art PUCF. **(a2)** Replacement procedure of the rotor, causing the loss of the contamination barrier and thus sterility. **(b1)** Proposed SL-PUCF concept providing a hermetically enclosed process chamber, by replacing rotary seals and mechanical bearings by two O-SBMs. **(b2)** Process chamber replacement with O-SBMs by simply taking it out of the opened O-SBMs.

Currently, for production scale production of viral vectors in industry, centrifugation for clarification is replaced by ultrafiltration, while ultracentrifugation for purification is replaced by chromatography and membrane filtration [2] due to the drawbacks listed in Tab.3.2(A).

Chromatography in short works based on the outer surface properties of the particles. This implies, that chromatography shows difficulties in separating particles, which have the same or very similar outer surface characteristics.

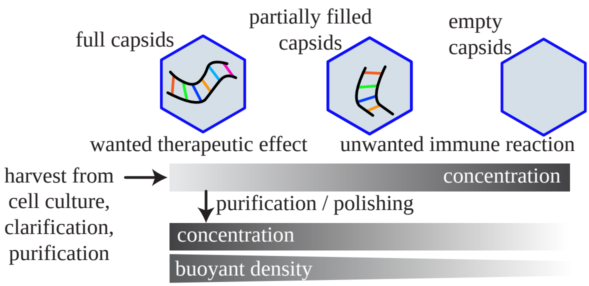

Fig. 3.3: In cell cultures for viral vectors, not only the wanted full capsids are produced, which have the intended therapeutic effect. Also empty or partially filled capsids are produced, which only lead to unwanted immune reaction. The same outer properties make it difficult for chromatography to remove the unwanted capsids. The difference in buoyant density enables ultracentrifuges to take over this task, but a scalable widely accepted solution for production scale is missing.

During the cell-cultivation of viral vectors, only $< 30\%$ of the capsids contain the therapeutic gene of interest, while $> 70\%$ represent empty capsids and $< 10\%$ are only partially filled [3] as conceptually illustrated in Fig.3.3. Unwanted co-produced empty or partially empty capsids show the same outer characteristics as full capsids. They do not contribute to the intended therapy, but trigger unwanted unnecessary immune reaction by immunotoxicity in the patient [3], [2].

According to [2], chromatography shows difficulties to separate full from partially or empty capsids. This failure to remove empty or partially empty capsids leads to an unwanted immune response in vivo.

However, due to buoyant density difference between full and empty capsids, equilibrium density ultracentrifugation can separate them. This is shown successfully with LaS-RUCFs [2], [56]. This shows today's dilemma in viral vector purification: great success is achieved in LaS-RUCF, but problems remain in PrS-PUCF. Reference [2] suggests therefore, to apply ultracentrifugation as a polishing step after chromatography for the removal of closely related contaminating species.

Reference [57] states: "there is a lack of an effective and reproducible platform method for the separation of full capsids from the empty capsids"; [56] regards it as part of the "challenges in downstream purification of gene therapy viral vectors". The principle advantage over chromatography by ultracentrifugation, to be able to separate full and empty capsids by buoyant density, leads to new research activity for PrS-PUCF [58]. But the problems of ultracentrifugation unveiled in Tab.3.2(A) remain unsolved.

For the earlier process step of clarification, the landscape of available commercial PrS centrifuges to reduce filter area is broad; with for example the CARR Biosystems UniFuge and sartorius stedim Ksep and additionally with very new developments: Alfa Laval CultureOne [59] and GEA kytero [60].

However, for ultracentrifugation, today no solution exists, which omits the problems in Tab.3.2(A) and solves the technical reasons in Tab.3.2(B). Based on these identified problems, to overcome them, new system level requirements are defined in Tab.3.2(C).

The main objective of this chapter therefore is to find technical solutions to close today's technology gaps for realizing a SL-PUCF prototype for viral nanotechnology and to provide a first system validation thereof with an outlook on its unique future capability potential.

The proposed and realized SL-PUCF concept in this chapter is presented in Fig.3.4. The concepts realized O-SBM hardware is shown in Fig.3.4(a), allowing to radially open due to the splitting plane, separating the O-SBM halves O-SBM 1a and O-SBM 1b. This enables the placement of a hermetically sealed process chamber shown in Fig.3.4(b). Feed suspension and density gradient media can be fed from above via the inlets. A further connector enables the supply and removal of the process gas surrounding the rotor. During the ultracentrifugation process, the fed particles separate along the density gradient in radial direction and settle at the radius of their corresponding density. An outlet allows the separated particles to be discharged.

In the following, component level requirements RY, which currently show technology gaps Pi, are identified. They have to be overcome to fulfill the system level requirements defined in Tab.3.2(C). The SL-PUCF system is divided into the three main SL-PUCF hardware components Cj: the O-SBMs, C1, the SL-PUCF rotor, C2, and the burst armor, C3, as shown in Fig.3.5.

For C1, O-SBMs were experimentally studied and proven to work for the first time in [18], to the author's knowledge. A solid test-rotor was magnetically levitated and accelerated to a rotational speed of up to 103 krpm with a horizontal axis of rotation.

For the O-SBMs, the first component requirement RA with problems is identified as the need for yoke air-gaps (y-AGs) between the stator halves due to corrosion protection enclosing or coating of the stator yokes in the splitting plane. This combined with compared to [18] newly required vertical rotor axis leads to the new problems P1, the axial stiffness ripple $\Delta k_{\mathrm{B,ax}}$, and

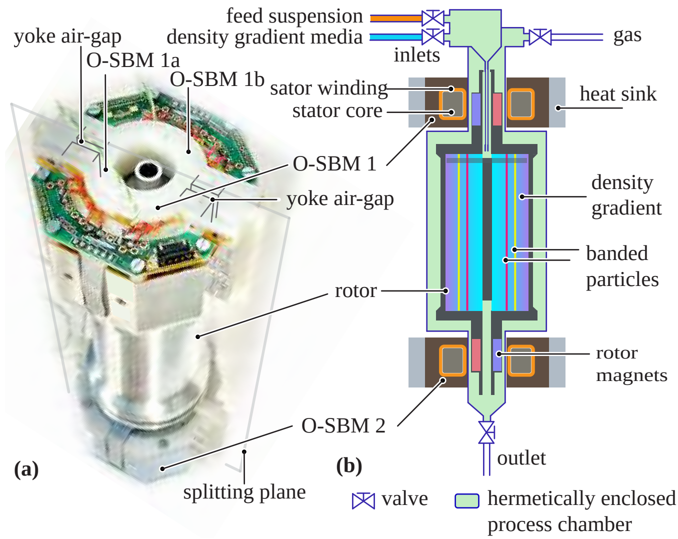

Fig. 3.4: (a) Sealless production ultracentrifuge drive system prototype consisting of two along the splitting plane openable self-bearing motors (O-SBM 1 and O-SBM 2). **(b)** Schematic section view of the proposed sealless production ultracentrifuge concept.

P2, the excitation of an axial rotor displacement $z\prime$. As solutions S1 and S2, a yoke design feature and rotor magnet design guidelines are proposed.

The problem of yoke air-gap induced parasitic currents was solved in [18] with a feed-forward current control scheme and is mentioned here for completeness.

In biopharmaceutical clean-rooms, passive cooling is preferred over active cooling to not disrupt the controlled airflow in the room. It furthermore omits contamination risk by cooling liquid and reduces complexity, especially for the openable part of the O-SBMs. However, this is currently prevented by the problem P3, that the heat extraction from the O-SBM windings at such high rotational frequencies with an aluminum heatsink generates too high eddy current losses, and non-conductive potting material results in too high winding temperature. Therefore, a new passive heat extraction solution S3, which is scalable from LaS-PUCF to PrS-PUCF is required. The solutions S1-S3 for the problems P1-P3 for the component C1, the O-SBMs, are presented in Sec.3.2.

For the component C2, the SL-PUCF rotor, the requirement RC of a sealless fluid path leads to the problem P4, that no seals are available anymore to guide the fluid. As a solution S4, a new internal SL-PUCF rotor topology for guiding the fluid without any rotary seals is proposed. Additionally, the absence of rotary seals leads to the problem P5, that dynamic filling during rotation of the rotor is required, where rotor suspension stability becomes an issue. As solutions, a novel inflow distributor S5a, and novel equalizing channels S5b are proposed. The solutions S4-S5b for the component C2, the SL-PUCF rotor, are presented in Sec.3.3.

The SL-PUCF needs a burst armor, the component C3, to contain rotor fragments in case of a rotor failure. The system requirement of a fast exchangeable rotor and process chamber leads to the component requirement RD of an openable burst armor. The problem P6 arises to contain the high rotational energy despite the potential weak points of the joints. As solution S6, a novel burst armor design is proposed, tailored to contain the high rotational energy while capable to open for rotor exchange, presented in Sec.3.4.

Fig.3.5 shows additionally the interconnection of SL-PUCF components and its design domains including electric, magnetic, thermal, mechanic and fluiddynamic domains, highlighting the interdisciplinary nature of the SL-PUCF system.

Sec.3.5 shows an experimental system validation of the working principle of the proposed novel SL-PUCF concept with a realized LaS-PUCF prototype. Sec.3.6 gives an outlook to the novel future smart capability potential of the SL-PUCF, which is newly possible thanks to the O-SBMs as a drive system. Examples for applications of such capabilities are shown additionally in the form of three case studies. In Sec.3.7, a brief discussion of the findings is given. Sec.3.8 summarizes the findings.

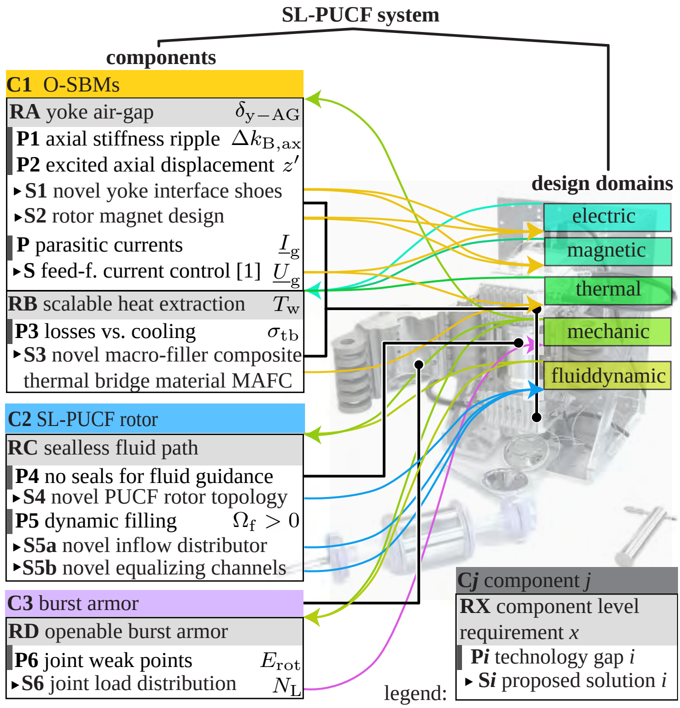

Fig. 3.5: For each of the SL-PUCF components, O-SBMs C1, the SL-PUCF rotor C2, and the burst armor C3, identified problems Pi and solutions Si thereof. Additionally, the interdisciplinary interrelations to the design domains are shown.

3.2 Component C1: Openable Self-Bearing Motors

3.2.1 Technology Gaps due to Component Requirement RA; Yoke Air-Gaps

To enable the SL-PUCF rotor, shown in Fig.3.4, to be emptied at the end of the ultracentrifugation process cycle or for continuous flow processing, the axis of rotation must be vertical. Until now, O-SBMs have only been operated with a horizontal axis of rotation when introduced in [18], as illustrated in Fig.3.6(a). In horizontal operation, the axial passive magnetic reluctance

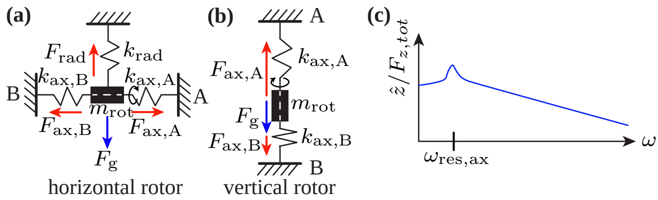

Fig. 3.6: (a) Balanced axial rotor forces $F_{ax,i}$ in horizontal rotor axis operation. **(b)** Vertical rotor axis orientation leads to unbalanced axial rotor forces and therefore to axial excitation by non canceling axial stiffness ripples. **(c)** The passive magnetic axial resonance frequency $\omega_{res,ax}$.

forces $F_{ax,i}$ are in equilibrium, if both rotor magnets are magnetized in the same radial direction (no angular offset), i.e. aligned.

Problem P1: Axial Stiffness Ripple

The new vertical rotor operation with O-SBM, as illustrated in Fig.3.6(b), leads to axially unbalanced $F_{ax,i}$. They are unbalanced due to the weight force F_G of the rotor mass m_{rot}, which needs to be compensated by $F_{ax,i}$. As shown in the following, O-SBMs exhibit a parasitic axial stiffness ripple $\Delta k_{B,ax}$. The combined stiffness ripple is for a vertical axis of rotation unbalanced, whereas its components cancel each other out with a horizontal axis of rotation and aligned magnet orientation.

The passive axial magnetic bearing stiffness $k_{B,ax,i}$ together with m_{rot} lead to a spring-mass system with an axial resonance frequency $\omega_{res,ax}$ as illustrated in Fig.3.6(c).

Overcoming this resonance was not a problem for the O-SBMs in [18], because they were operated with horizontal axis of rotation with resulting cancellation of $F_{ax,i}(\varphi)$. However, this is not the case for vertical axis rotor operation as studied in this chapter. In this case, $k_{B,ax,i}$ excite the axial resonance mode and axial displacement (problem P2), which makes it difficult or impossible to pass through the axial resonance. A state of the art solution for magnetic bearings would be, to install additionally an active axial magnetic bearing. However, this would significantly increase the complexity of both the O-SBM stator and rotor. Additionally, from a process perspective, it would take away system design freedom for the SL-PUCF flow path design in the rotor. For this reason, the mechanisms of the axial excitation are investigated in depth, and the corresponding negative effects are reduced by design measures to enable safe passing through $\omega_{res,ax}$.

Solution S1: Novel Yoke Interface Shoes to counteract Yoke Air-Gap induced Axial Stiffness Ripple

The y-AGs between the stator halves lead to a dependency of the magnetic circuit reluctance on the rotor angle φ.

The question remains, why very small y-AGs of only 0.2 mm as in this chapters prototype lead to a significant adverse effect. This is investigated first. Fig.3.7(a) shows a cross-section of an O-SBM. It shows the cross-sectional areas through which half of the rotor permanent magnet (PM) flux $\phi_\mathrm{d}/2$ has to pass. The y-AG length is much smaller than the total air-gap of the magnetic circuit. However, the y-AG surface is much smaller compared to the air-gap surface shown in Fig.3.7(a). This cross-section area difference explains the surprising substantial influence of the y-AGs.

Fig.3.7(b1) shows the stator yoke prototype made of soft magnetic composite (SMC) material from [18]. It is generally not possible to manufacture sharp edges out of SMC due to its brittleness. There will always be a small radius, which further reduces the y-AG cross-sectional area. For small motors, the problem of the y-AG becomes therefore even more acute.

With the aim of reducing the parasitic effects of the y-AGs, the solution S1 is proposed in this chapter and realized as a prototype: novel yoke interface shoes. The intention is to increase the y-AG surface by widening of the yoke cross-section at the interface as shown in Fig.3.7(b2).

Fig.3.7(c) shows magnetostatic 3D-FEM results of the magnetic flux density B distributions in a O-SBM cross-section with the novel yoke interface shoe. Two distinct angular rotor positions are shown. In the first, the d-axis is perpendicular to the stator splitting plane. Half of the rotor flux $\phi_\mathrm{d}/2$ has to cross each y-AG, as shown in Fig.3.7(c1). The rotor flux utilizes the full widening of the yoke at the novel interface shoes, supporting the theory in Fig.3.7(a). It crosses the widened y-AG surface without substantial fringing flux, in Fig.3.7(c2). This supports the theory in Fig.3.7(a) as well, as apparently half of the rotor flux must indeed pass through the y-AG.

In the second case the d-axis lies in the splitting plane as shown in Fig.3.7(c4). In this case, no rotor flux passes through the y-AG, but enters the yoke through the surfaces facing the rotor as shown in Fig.3.7(c3). This case therefore does not lead to an increase in reluctance. The reluctance of the magnetic circuit varies during rotor rotation between these cases.

Fig.3.7(d) unveils the occurring torque ripple for y-AGs lengths of $\delta_\mathrm{y} = 0.2$ mm and $\delta_\mathrm{y} = 0.4$ mm determined with 3D-FEM. The increase of the torque ripple when doubling the y-AG proves it to be the cause. The new stator yoke with the novel yoke interface shoes shows a reduction in torque ripple of

Tab. 3.3: Solution S1: yoke interface shoes - main result.

S1: problem remedy	main result
axial stiffness ripple $\Delta k_{B,ax}$ RMS reduction for a yoke air-gap of 0.2 mm and a yoke air-gap surface increase of 33%	−39%

21 % for $\delta_y = 0.2$ mm and 20 % for $\delta_y = 0.4$ mm for an increase of the y-AG cross-sectional area by 33 %. Fig.3.7(e) shows the axial stiffness ripple $\Delta k_{B,ax}$ resulting from the y-AGs. However, the new yoke interface shoes allow a RMS reduction of $\Delta k_{B,ax}$ by 39 % for $\delta_y = 0.2$ mm and 27 % for $\delta_y = 0.4$ mm. Tab.3.3 summarizes the main findings of solution S1.

Problem P2: Excited Axial Displacement

An axial displacement z of the rotor leads to an axial restoring force F_z in the stator as shown in Fig.3.8(a), defined by the axial stiffness k. The combination of two O-SBMs with a common rotor leads to a superposition of these axial forces shown in Fig.3.8(b). The combined stiffness k_{tot} depends on the rotor angle φ and the relative magnetization direction offset of the two rotor magnets θ as shown in Fig.3.8(c). Based on the 3D-FEM simulation results of Fig.3.7(e), the axial stiffness k is modeled as a mean value with a superimposed second harmonic caused by the y-AGs:

$$k_A = k_{ax} + k_\Delta \sin(2\varphi + \theta) \tag{3.1}$$

$$k_B = k_{ax} + k_\Delta \sin(2\varphi) \, . \tag{3.2}$$

The rotor displacement in relation to the magnetic center of the rotor is designated by the new coordinate z'. A pre-set offset of the rotor magnets w.r.t. the stators is referred to here as z_{ps}. Fig.3.8(c) shows the combined axial force generation by both O-SBMs, it results as:

$$F_{z,tot}(z') = (z' + z_{ps}) \cdot k_B(\varphi, \theta) + (z' - z_{ps}) \cdot k_A(\varphi, \theta) \, . \tag{3.3}$$

The averaged rotor displacement in axial direction $\bar{z'}$ is determined by the balance of the gravitational force F_g on the rotor mass m_{rot} with the two superimposed averaged axial stiffnesses $\bar{k}_{ax}$:

$$\bar{z'} = -\frac{m_{rot} \cdot g}{2\bar{k}_{ax}} . \tag{3.4}$$

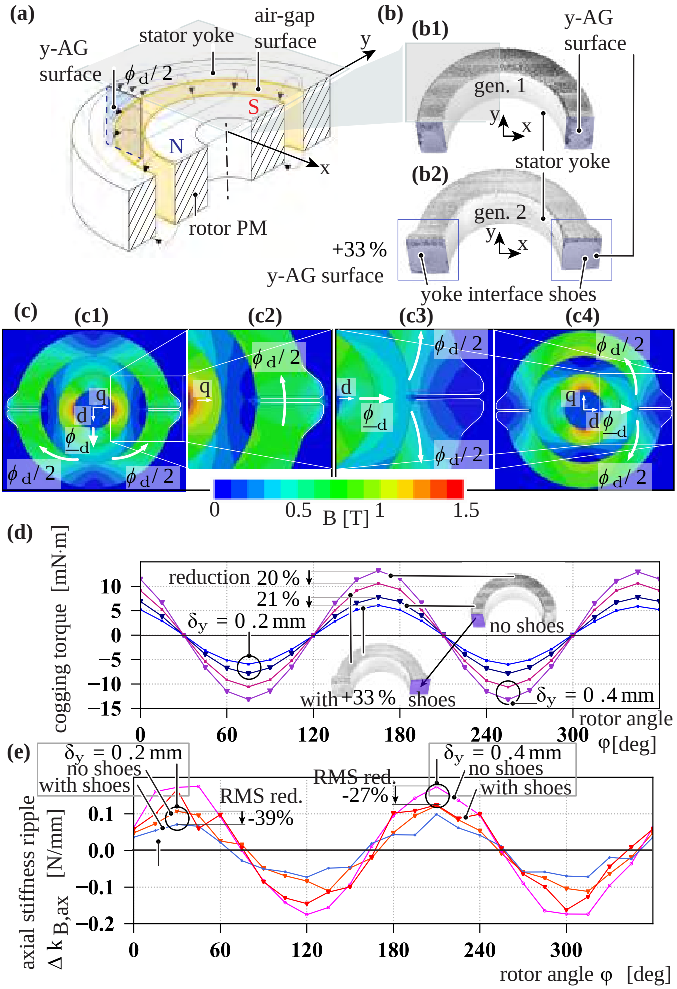

Fig. 3.7: (a) Cross-section through a O-SBM. The yoke air-gap (y-AG) surface is by factors smaller than the air-gap surface. **(b)** Realized stator yokes, **(b1)** first generation openable stator yoke from [18], **(b2)** improved second generation version with solution S1: novel yoke interface shoes. **(c)** Magnetostatic 3D-FEM result of the flux density distribution for the novel yoke interface shoes. **(d)** Yoke interface shoes lower the y-AG induced torque ripple and **(e)** the axial stiffness ripple substantially.

This averaged value turns out to be independent of z_{ps}. The assumption here is, that the axial load capacity limit of the O-SBMs has not yet been exceeded. The axial equation of motion for the rotor is

$$F_{\text{z,tot}}(z') = -m_{\text{rot}} \cdot g + m_{\text{rot}} \cdot \ddot{z}'. \tag{3.5}$$

It shows a resonance frequency of

$$f_{\text{res,ax}} = \frac{1}{2\pi} \cdot \sqrt{\frac{2 \cdot k_{\text{ax}}}{m_{\text{rotor}}}}. \tag{3.6}$$

For high frequencies, i.e. speeds far above f_{res}, the system acts as a low-pass filter and axial vibrations are damped. Therefore, for passing through $f_{\text{res,ax}}$, the low frequencies are relevant. The quasi-static axial rotor displacements are analyzed for this purpose. The quasi-static force equilibrium is as follows:

$$F_{\text{z,tot}}(z') = -m_{\text{rot}} \cdot g. \tag{3.7}$$

Solved for the axial rotor displacement z', the result is:

$$z' = \frac{-m_{\text{rot}} \cdot g - z_{\text{ps}} \cdot k_{\Delta} \left[\sin(2\varphi) - \sin(2\varphi + \theta)\right]}{2k + k_{\Delta} \left[\sin(2\varphi) + \sin(2\varphi + \theta)\right]}. \tag{3.8}$$

The question arises, which relative rotor magnet orientation offset θ should be selected between the two rotor magnets in order to keep the axial vibration levels at low speeds as small as possible. Additionally, the influence of the axial pre-set z_{ps} displacement remains unclear. This is analyzed in the following.

Solution S2: Magnet Design - Novel Guideline for Optimal Choice of Relative Magnet Orientation offset θ

The extreme values of the quasi-static axial vibration amplitudes can be determined for the cases $\theta = 0°$ and $\theta = 90°$ considering the value ranges of the sine values in Eq.3.8:

$$z'_{\theta=0°} = \frac{-m_{\text{rot}} \cdot g}{2 \cdot (k \pm k_{\Delta})} \tag{3.9}$$

and

$$z'_{\theta=90°} = \frac{-m_{\text{rot}} \cdot g \pm 2 z_{\text{ps}} k_{\Delta}}{2k}. \tag{3.10}$$

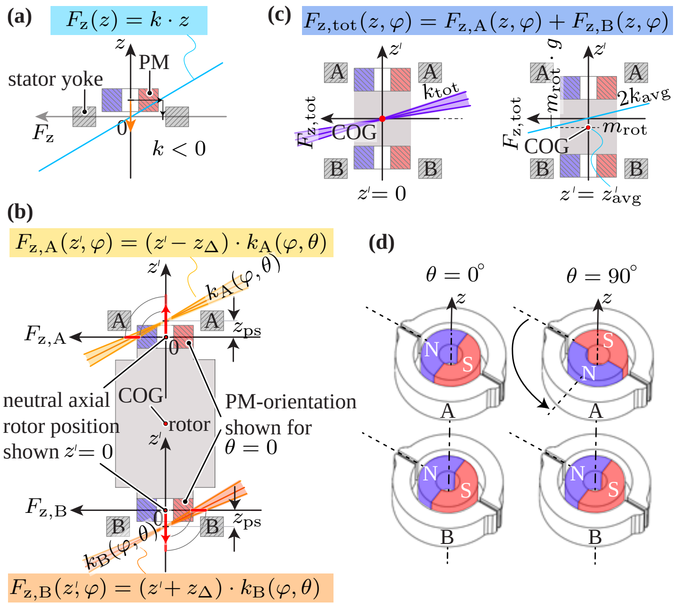

Fig. 3.8: (a) Axial bearing stiffness k of a SBM. **(b)** Individual axial stiffnesses of the two O-SBMs. The rotor is shown with a pre-set offset z_{ps} and axially in neutral symmetric position. The axial stiffnesses k vary during rotation due to the y-AGs. **(c)** Combined axial stiffnesses of the two SBMs and average combined axial stiffness k_{avg} and rotor position. **(d)** The two investigated rotor magnetization orientation combinations.

The resulting quasi-static axial vibration amplitudes are:

$$\hat{z'}_{\theta=0^\circ} = \frac{m_{rot} \cdot g \cdot k_\Delta}{2 \cdot \left(k^2 - k_\Delta^2\right)} \tag{3.11}$$

and

$$\hat{z'}_{\theta=90^\circ} = \frac{z_{ps} k_\Delta}{k}. \tag{3.12}$$

With the introduction of the rotor pre-set axial offset ratio α of the pre-set displacement z_{ps} to the average axial rotor displacement $\bar{z'}$:

$$\alpha := \frac{z_{ps}}{\bar{z'}} \tag{3.13}$$

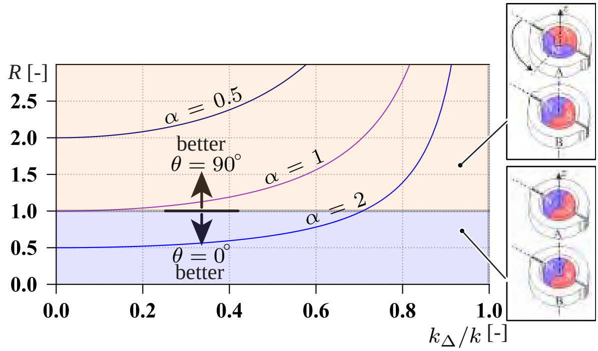

Fig. 3.9: Guideline for the optimal magnet orientation offset θ for a vertical axis double O-SBM system based on the axial offset ratio α, and the stiffness variation. R is the ratio of the quasi-static axial vibration amplitudes of $\theta = 90°$ to $\theta = 0°$. $R > 1$ indicates that $\theta = 90°$ is favorable, while for $R < 1$ $\theta = 0°$ is superior.

the ratio R of the amplitudes for the two θ values can be determined as

$$R = \frac{\hat{z}'_{\theta=0°}}{\hat{z}'_{\theta=90°}} = \frac{m_{\mathrm{rot}} \cdot g \cdot k}{2 \cdot \left(k^2 - k_\Delta^2\right) z_{\mathrm{ps}}} = \frac{1}{\left(1 - \left[\frac{k_\Delta}{k}\right]^2\right) \cdot \alpha}. \tag{3.14}$$

This relationship is shown in Fig.3.9. Depending on α and the ratio k_Δ/k, it is shown, which θ value leads to the lowest quasi-static vibration amplitudes. Thus, it is analytically derived, which θ value is optimal for a given system. According to these results, there is even a case, in which the quasi-static axial vibrations can be completely eliminated: for the case of $\left(z_{\mathrm{ps}} = 0 \;\&\; \theta = 90°\right)$. In the following, however, it is shown why a system with $z_{\mathrm{ps}} > 0$ has other important advantages. The derived design guideline also shows the optimum magnet orientation for such a system.

Solution S2: Magnet Design - Novel Guideline for Rotor Magnet Dimensions

The design of the rotor magnet has an influence both on the motor performance, as well as the magnetic bearing properties. It is therefore also linked to the axial resonance. Fig.3.10(a) shows a to the stator yoke centered magnet whose length l_{m} corresponds to that of the stator yoke, l_{s}. Additionally, an illustration of a potential extension of the magnet, that goes beyond this, is shown. A length extension of the magnet leads to additional torque formation

Tab. 3.4: Solution S2: rotor magnet design - main result.

S2: problem remedy	**main result**
counteracting axial displacement excitation	design guideline for relative rotor magnet orientation offset θ, and for the rotor magnet dimensions

by stray field utilization by the toroidal windings of the stator. Fig.3.10(b) shows the resulting increase in the torque constant k_t and the resulting axial force F_z as a percentage compared to the values of the reference magnet with $l_m = l_s$. There is a very strong increase in k_t with increasing l_m. For the O-SBMs of this chapter, the increase in k_t is more than 30% with a magnet extension of 50%. The magnetic center of the magnet shifts relative to the stator by the distance a in Fig.3.10(a), which leads to the axial restoring force shown in Fig.3.10(b). Fig.3.10(c) shows an additional axial shift b of the rotor magnet. The magnet center is therefore axially shifted by $a + b$. Fig.3.10(d) shows the resulting reduction of k_t. Over the entire stable range of axial stiffness, k_t is higher than in the centered case $l_m = l_s$. Thus, the presented O-SBM design is within the stability limits beneficially largely insensitive to axial shift or rotor weight induced displacement regarding motor performance.

This good-natured behavior allows a short overall length design of the thin rotor shaft that protrudes from the rotor cylinder l_{rs}, which keeps the rotor bending resonance frequency advantageously low. This also facilitates a sufficiently large axial clearance c_{ax} between the rotor and the centrifuge housing to cross $f_{res,ax}$. Therefore, the prototype of this chapter is realized with $z_{ps} > 0$, $\alpha > 1$, and $R < 1$. This leads according to Fig.3.9 to an optimal magnet orientation angle $\theta = 0°$, which is implemented in the prototype. Tab.3.4 summarizes the main findings of solution S2.

3.2.2 Technology Gaps for Component Requirement RB: Scalable Heat extraction

Problem P3: Losses vs. Cooling

Very high-speed slotless motors with toroidal windings generate high-frequency stray fields. They therefore do not allow close contact direct cooling of the stator via an aluminum heat-sink, as it is usually the case for motors, or only with the acceptance of high additional losses [61], [62], [63]. Therefore,

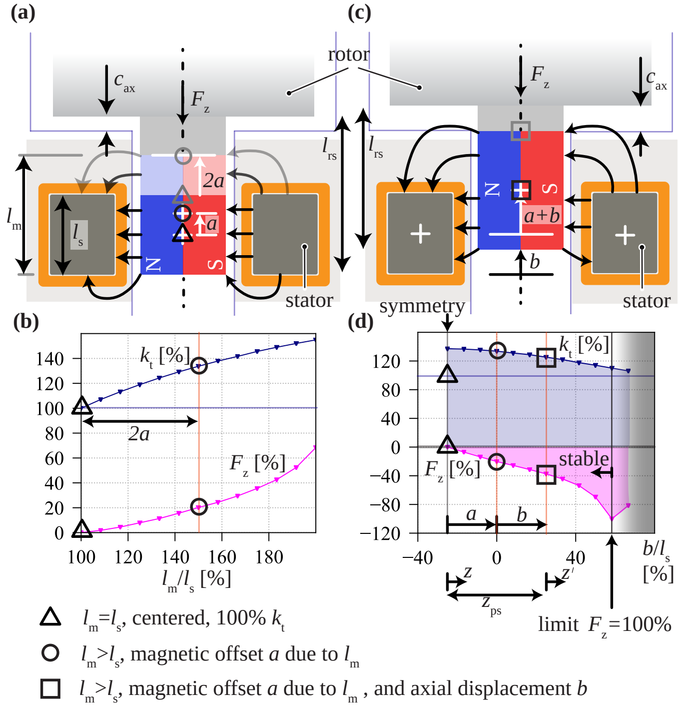

Fig. 3.10: **(a)** Rotor magnet length l_m increase towards the rotor center, exceeding the stator length l_s. **(b)** Resulting increase in torque constant k_t and non-zero axial reluctance force F_z. **(c)** Additional axial displacement b with **(d)** resulting influence on k_t and F_z.

electrically conductive materials in the immediate vicinity of the stator should be avoided.

As a consequence, the heat-sink needs to be placed at distance form the stator. A thermal bridge material is needed to bridge this gap. An ideal thermal bridge material is electrically insulating but highly thermally conductive.

The O-SBMs of this chapter have a design efficiency η_{O-SBM} of 89.2 %, and a peak continuous shaft power to overcome the rotor gas friction at 100 krpm of 280 W, resulting in to be dissipated motor losses of 33.9 W. For a good potting material with a thermal conductivity of 1.2 W/(mK), the thermal resistance of the thermal bridge of these O-SBMs between winding and heatsink analytically calculated is 2.2 K/W. Therefore, the temperature drop from stator winding to heatsink is 74.6 K. For a heatsink temperature of 40°C, the winding surface temperature becomes 114.6°C. This temperature is too high for the close by position sensing electronics.

This type of motor is therefore currently limited in applicability and scalability for high power outputs. However, the scale up is necessary in the biopharmaceutical industry for the process scale up from LaS systems to PiS and further to PrS systems.

Solution S3: Novel Macro-Filler Composite (MAFC) Thermal Bridge Material

As a solution, the disadvantage of the large distance to be bridged thermally is transformed into an advantage. The large distance allows to place few mm large macroscopic filling elements within the potting in the space to be bridged. This is referred to in this chapter as macro-filler composite (MAFC). The advantage over conventional microscopic fillers is, that the heat can be conducted over comparably long distances via the macro-filler instead of through a microscopic mixture of casting compound and filler particles.

In addition, advantageously the cured hardness is high, which is not the case for soft silicone based potting compounds. Furthermore, MAFC are realizable at a substantially lower material cost compared to special potting compounds with micro-fillers. Moreover, the potting compound retains its low viscosity between the macro-fillers, which means that a good bond can be achieved to the stator winding wires and the heat sink surface. This is more difficult with micro-fillers due to the paste-like consistency of the compound. The solution S3 proposed in this chapter is a ceramic macro-filler and epoxy-potting MAFC. Electrically insulating aluminum oxide Al_2O_3 ceramic spheres, which are available on the market in various size classes at very low cost, are proposed as macro-fillers. At 30 W/(mK), they have a thermal conductivity, that is 30...60 folds higher than that of conventional potting compounds. Al_2O_3 is additionally beneficially electrically insulating. The selected sphere size for this chapter is $3 - 7$ mm with costs for small quantities of 30 Euros/kg and for large quantities 16.50 Euros/kg. However, smaller sizes of e.g. $0.75 - 1.5$ mm are also available. The price for the potting compound ER2074 used in this chapter is 84 Euros/kg for large quantities. Although custom manufactured ceramic parts would be thermally even better, the MAFC proposed here is an extremely cost effective solution, which flexibly can be used for arbitrary geometries without expensive manufacturing of ceramic parts.

Solution S3: Theoretical Investigation of MAFC

Fig.3.11(a) schematically shows the proposed SL-PUCF concept. Fig.3.11(b) and (c) show the stator in two versions, both with the aluminum heat-sink placed at a distance. In version (b), the distance between the stator and heat-sink is bridged with conventional potting compound. In the new version (c) below, the novel proposed MAFC is used. Fig.3.11(d) shows conceptually the intended reduction in motor winding temperature T_W. Fig.3.11(e) shows a series thermal resistance model for the conservative estimation of the thermal conductivity λ_c of MAFC. The series model of MAFC is conservative because it neglects beneficial parallel heat paths which are also present in MAFC, which increase λ_c. The series model is therefore a conservative estimate for a lower limit of λ_c. The actual value of λ_c is thus guaranteed to lie above, while neglecting contact resistances at the material interfaces.

The temperature drop ΔT_{tb} over the thermal bridge is according to the serial model in Fig.3.11(e):

$$\Delta T_{tb} = \frac{Q}{A}\left[\frac{L_{tb}}{\lambda_c}\right] = \frac{Q}{A}\left[\frac{v_{mf} \cdot L_{tb}}{\lambda_{mf}} + \frac{(1 - v_{mf}) \cdot L_{tb}}{\lambda_p}\right], \tag{3.15}$$

with the heat flux Q, cross-section A, length of the thermal bridge L_{tb}, volume fraction of the macro-filler v_{mf}, thermal conductivities of the macro-filler material λ_{mf} and potting material λ_p. This results in the thermal conductivity λ_c of MAFC:

$$\lambda_c = \frac{\lambda_{mf}\lambda_p}{v_{mf} \cdot (\lambda_p - \lambda_{mf}) + \lambda_{mf}}. \tag{3.16}$$

The mathematically optimal possible packing density of spheres, i.e. volume fraction in 3D, $v_{s,max}$ assuming spheres of the same size is [64]:

$$v_{s,max} = \pi/\sqrt{18} = 0.7404. \tag{3.17}$$

Based on this theoretical optimum, a MAFC filling quality η_q is defined here, which quantifies the achieved MAFC volume fraction v_{mf} relative to the theoretical optimum $v_{s,max}$,

$$\eta_q = v_{mf}/v_{s,max}. \tag{3.18}$$

This results in the thermal conductivity of MAFC:

$$\lambda_c = \frac{\lambda_{mf}\lambda_p}{\eta_q \cdot v_{s,max} \cdot (\lambda_p - \lambda_{mf}) + \lambda_{mf}}. \tag{3.19}$$

Fig.3.11(f) shows the lower limit of achievable MAFC thermal conductivity λ_c, depending on the MAFC filling quality η_q. The positive effect of MAFC is amplified, the better the conductivity of the potting material, because the Al_2O_3 macro-filler has substantially higher thermal conductivity then the potting material. For the O-SBMs of the SL-PUCF prototype, the selected potting material for the MAFC is ER2074 with a thermal conductivity of 1.25 W/(mK). With a MAFC filling quality of $\eta_q = 0.6 \dots 0.8$, an improvement of over 100 % in thermal conductivity from λ_p to λ_c is thus expected based on the series model.

Solution S3: MAFC Realization and Thermal Conductivity Measurement Units

To experimentally validate the model predicted improvement in λ_c compared to λ_p, thermal conductivity measurement units are designed and built. Fig.3.12(a) shows their working principle. A heat flux Q is generated by the heating resistor R_i. Its dissipated power Q is measured by the DC current through R_i and voltage across R_i. A square copper heat spreader with 32 mm side length enables a uniformely distributed heat flux due to its higher thermal conductivity compared to potting material by two orders of magnitude ($\lambda_{Cu} = 391\,W/mK$). Q is then injected into the medium under test. The heat is conducted to the measurement unit heat sink which is actively cooled by a cooling fan. The temperature difference between the inner surfaces of the heat spreader and the heat sink, $\Delta T = T_c - T_{HS}$, is measured. ΔT is only dependent on Q, the thermal conductivity of the medium under test, and its cross-section. The airflow condition at the measurement unit heat sink therefore has no influence on the measured ΔT. It only changes the absolute temperatures, but not ΔT and is therefore irrelevant for the measurement. In the SL-PUCF system, the heat-sink is comprised of the O-SBM housing including the mounting structure and is dimensioned large enough to ensure a heat sink temperature of not higher than 40° C. The heat sink in the measurement units with the fan is only for the measurement purpose. Fig.3.12(b) shows the hardware realization of a thermal conductivity measurement unit. It additionally shows the filling process with Al_2O_3 MAFC spheres. As a MAFC production method, a repeated layering of potting material, placement of a macro-filler layer, and soft compaction with a soft plastic stick was conducted.

Fig.3.12(c) and (d) show the four realized thermal conductivity measurement units before, and after filling respectively. Two are filled with MAFC and two with potting only, as a comparison. Fig.3.12(e) shows the setup for the thermal conductivity measurement.

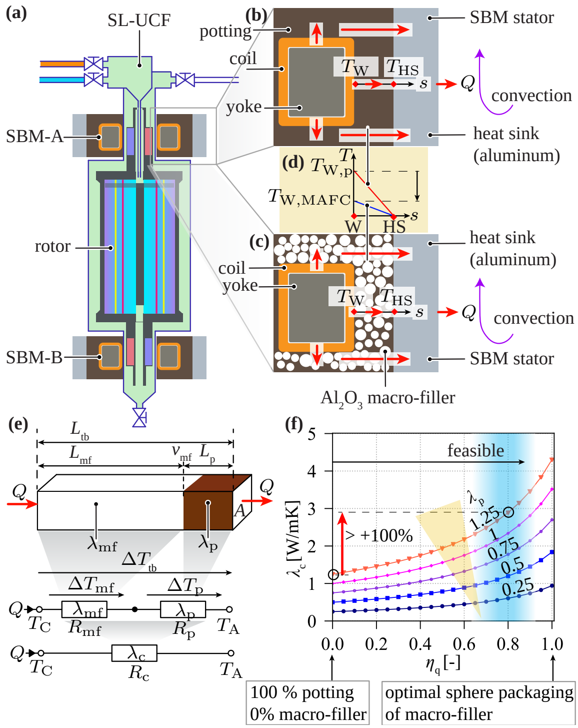

Fig. 3.11: (a) SL-PUCF concept with O-SBMs suspending and driving the SL-PUCF rotor. **(b)** Heat sink at distance to the stator stray fields, with potting material as a thermal bridge. **(c)** Novel macro-filler composite (MAFC) of macroscopic ceramic (aluminum oxide Al_2O_3) spheres surrounded by potting material, forming a substantially better thermally conductive and electrically insulating thermal bridge material. **(d)** Conceptually shown thermal bridge material dependent effect on the winding temperature T_W. **(e)** MAFC thermal resistance conservatively modeled as a series connection of the individual volume share of the two materials. **(f)** Theoretical lower limit of the achievable MAFC thermal conductivity λ_c based on the filling quality η_q and the thermal conductivity of the potting material λ_p.

Solution S3: Experimental Validation of MAFC Thermal Conductivity Improvement

Fig.3.13(a) shows the measured temperature difference ΔT rises for a power input per measurement unit of $P_R = 1.25$ W. The MAFC performs substantially better than the potting alone. This becomes more evident by computing the resulting thermal conductivity, taking into account the leakage heat flux $Q_{\mathrm{leak,ins}}$ through the thermal insulation in the measurement units. $Q_{\mathrm{leak,ins}}$ is determined by measuring the outer measurement unit surface temperature with a contactless infrared thermometer, the thermal conductivity of the polyurethane foam insulation of $0.02\,\mathrm{W/(m\cdot K)}$, and the measured internal temperatures. For the λ_{c} characterization, due to linearity of heat conduction, the specific amount of Q applied and the absolute temperatures T_{c} and T_{HS} are on its own irrelevant. Only the measured thermal conductivity λ_i is relevant and results as:

$$\lambda_{\mathrm{c},i} = \frac{(Q_i - Q_{\mathrm{leak,ins},i}) \cdot L_{\mathrm{t}}}{A \cdot \Delta T_{\mathrm{C-HS},i}}. \tag{3.20}$$

The resulting conductivities are shown in Fig.3.13(b). The measured thermal conductivity for the pure potting with ER2074 of $1.18\,\mathrm{W/(m\cdot K)}$ averaged over two units deviates only 5.6 % from the data sheet value of $1.25\,\mathrm{W/(mK)}$. This validates the experimental measurement procedure. The Al_2O_3 MAFC showed over two units an averaged thermal conductivity of $\lambda_{\mathrm{c}} = 4.0\,\mathrm{W/(mK)}$. The corresponding two paired conductivity measurements of the same material types coincide very well, as shown in Fig.3.13(b). This indicates a good repeatability of the MAFC production method. The achieved production quality of $\eta_{\mathrm{q}} > 0.6$ was determined by measuring the weight of the amount of macro-filler spheres filled. The measured improvement of the thermal conductivity by a factor of 3.4 validates experimentally the theoretically predicted excellent heat conduction capabilities of Al_2O_3 MAFC - while being electrically an insulator.

For the O-SBMs with $\eta_{\mathrm{O-SBM}} = 89.2\,\%$, a peak continuous shaft power at 100 krpm of 280 W and a MAFC with a conductivity of $4\,\mathrm{W/(m\cdot K)}$, the thermal resistance of the thermal bridge between winding and heatsink analytically calculated is $0.66\,\mathrm{K/W}$. Therefore, the temperature drop from the stator winding to the heatsink is reduced to 22.4 K. For a heatsink temperature of 40°C, the winding surface temperature is reduced from 114.6°C with conventional potting to 62.4°C with MAFC. This temperature is acceptable for the close by position sensing electronics.

The solution S3 is therefore validated. Thus, in this chapter, a solution to the in literature known passive cooling problem of ultra high-speed toroidal wound slot-less motors is found, theoretically predicted and experimentally validated. Tab.3.5 summarizes the main findings of solution S3.

Tab. 3.5: Solution S3: novel macro-filler composite thermal bridge material MAFC - main result.

S3: problem remedy	**main result**
increase in stator thermal bridge thermal conductivity	thermal conductivity increase compared to potting material by factor 3.4 to $\lambda_c = 4.0\,\mathrm{W/mK}$ with novel MAFC material

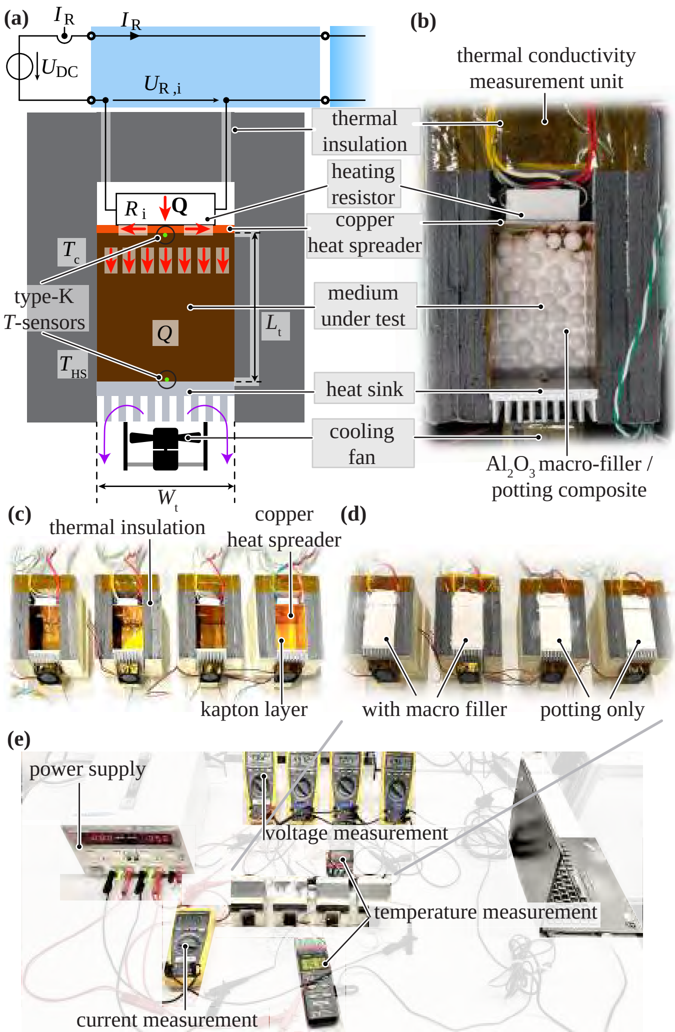

Fig. 3.12: (a) Schematic of the working principle of the purpose built measurement units for the measurement of the thermal conductivity of the novel ceramic macro-filler composite (MAFC) thermal bridge material. **(b)** One out of the four realized measurement units. **(c)** Measurement units before potting. **(d)** Potted units before being covered with a thermal insulation lid. **(e)** Setup for the thermal conductivity measurements.

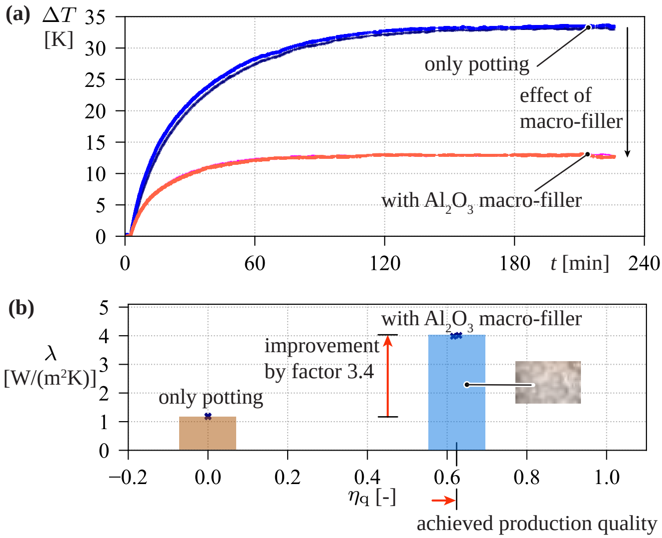

Fig. 3.13: (a) Measured temperature difference rises in the thermal conductivity measurement units for only potting material and for the novel ceramics macro-filler composite (MAFC). **(b)** The measured increase in thermal conductivity of the ceramic macro-filler composite compared to the pure potting material by a factor of 3.4.

3.3 Component C2: SL-PUCF rotor

3.3.1 Technology Gaps for the Component Requirement RC; Sealless Fluid Path

State of the art biopharmaceutical PUCFs have several rotary seals. They have the functions of a) sealing the process chamber from the production facility against contamination in both directions, b) sealing against reduced pressure or near vacuum outside the rotor, c) sealing as a connection between the rotor and both feed and discharge pipes during filling and emptying. However, they pose a contamination risk, generate friction losses and are speed-limited to approx. 40 krpm [65].

Problem P4: No Seals for Fluid Guidance

For the SL-PUCF, the rotary seal is replaced by the hermetically enclosed wall of the process chamber. This eliminates the risk of contamination through the seal. However, the functions of the seals in terms of guiding the fluid flow between the rotor inlet/outlet and the rotor are more difficult to achieve.

Solution S4: Novel PUCF Rotor Topology

The fluid topologies in this chapter should not be compared with the solutions for slow to medium-speed disk stack centrifuges as in [60]. The extremely high speeds of PUCFs require fluid guidance at the smallest possible radii and thus peripheral speeds. In today's PUCFs, the rotor can be filled from below while stationary due to the rotary seals, shown in Fig.3.14(a1). The rotor is accelerated after.

In a sealless concept, the fluid feed must come from above to prevent leaking. Proposed possible rotor topologies that allow the fluid to be automatically discharged from the rotor are shown in Fig.3.14(a). Possible topologies are a discharge pipe from above, Fig.3.14(a2), or a rotor with an integrated outlet valve, Fig.3.14(a3), or a rotor with a bottom outlet, whereby a novel feature, an inflow distributor, ensures that dynamic filling from above is possible without the fluid falling through the rotor while rotating, Fig.3.14(a4).

For sequential operation, i.e. repeated filling, separation and discharge, the topologies in Fig.3.14(a2) and Fig.3.14(a3) appear to be promising candidates, as slow, controlled filling and unloading is possible at standstill. However, the long thin feed tube is critical in terms of vibration, and for the topology in Fig.3.14(a3), the rotor integrated valve adds complexity. However, these

Tab. 3.6: Solution S4: novel PUCF rotor topology - main result.

S4: problem remedy	main result
SL-PUCF rotor topology without seals for fluid guidance	novel SL-PUCF rotor topology without rotary seals, filled from the top dynamically while the rotor rotates, incorporating an inflow distributor to avoid fluid from falling through the rotor and leaking out

two topologies do not appear to be very advantageous for continuous feed separation and discharge. However, the novel topology of Fig.3.14(a4) appears to be very suitable for this purpose and is therefore realized. It also appears attractive due to its robust and simple design.

Fig.3.14(b) shows the operating states of the proposed SL-PUCF. Fig.3.14(b1) shows the filling. The rotor is filled in contrary to the state of the art from above while the rotor spins, instead of at standstill from below. A novel inflow distributor prevents the liquid form falling through. Accordingly, the rotor fills radially inward, shown in Fig.3.14(b2). Depending on the wanted ultracentrifugation process, the suspension is sedimented down to the rotor wall, or banded as shown in Fig.3.14(b3). Examples of potential ways of extracting the separated suspension are: adding more of the cushion layer density gradient medium which forces radially the separated media inward, as shown in Fig.3.14(b4), or in form of an enrichment process where constantly suspension is fed supernatant discharged, or as shown in Fig.3.14(b5), reducing the rotational speed to gradually empty the rotor, or in case of an internal rotor valve of Fig.3.14(b5), decelerating the rotor to standstill and releasing the banded media. Tab.3.6 summarizes the main findings of solution S4.

Problem P5: Dynamic Filling

A challenge of the novel SL-PUCF rotor lies in filling while rotating, avoiding rotor unbalance. Given that the rotors of topologies in Fig.3.14(a2) and and Fig.3.14(a3) are operated only when completely filled, their magnetic suspension does not appear to be critical during operation. In contrast to those, the novel topology (a4) requires dynamic filling. The problems to be solved are P5a), i.e. preventing the fluid from falling through the rotor directly during filling while still maintaining direct access for the added fluid to all radius

Tab. 3.7: Solution S5a: novel inflow distributor - main result.

S5a: problem remedy	main result
novel inflow distributor which prevents fluid from falling through the rotor during dynamic filling	novel inflow distributor, with bores allowing for all radial positions fluid to enter the rotor; anisotropic fluid resistance in radial and axial direction enables fluid to fill radially inwards without falling through

positions in the rotor during continuous filling in separation mode, and P5b), i.e. avoidance of unbalance during the filling process.

Solution S5a: Novel Inflow Distributor

Fig.3.14(c) shows the layout of the proposed SL-PUCF. Fig.3.14(d) shows a rotor section view thereof. The novel inflow distributor enables filling from the top while spinning. Small bores in axial direction allow the fluid to enter the rotor on all radii. But their small size results in the fluid flowing mainly radially outwards first, as it is the path of lowest resistance. Hence the inflow distributors anisotropic fluid resistance in radial and axial direction are the key factors. The bores through the inflow distributor Fig.3.14(f) are placed, such that on all radii there is always an axial path available for the feed suspension. This avoids, that part of the feed suspension with a certain density is blocked from axially entering the rotor. The radial path length l_p is a process parameter, which is adapted depending on the ultracentrifugation task. For the function of the inflow distributor, the larger l_p, the more difficult to maintain its function. Therefore the prototype in Fig.3.14(f-g) was realized with the maximum l_p possible to investigate the worst case. Tab.3.7 summarizes the main findings of solution S5a.

Solution S5b: Equalizing Channels

Novel equalizing channels between the divided rotor sectors enable unbalanced liquid in the rotor to equalize their level across the whole rotor and thus prevent unbalance. They are shown in Fig.3.14(d,e,g,h). Fig.3.14(h) shows the assembled SL-PUCF rotor, with its rotor jacket in Fig.3.14(i). Tab.3.8 summarizes the main findings of solution S5b.

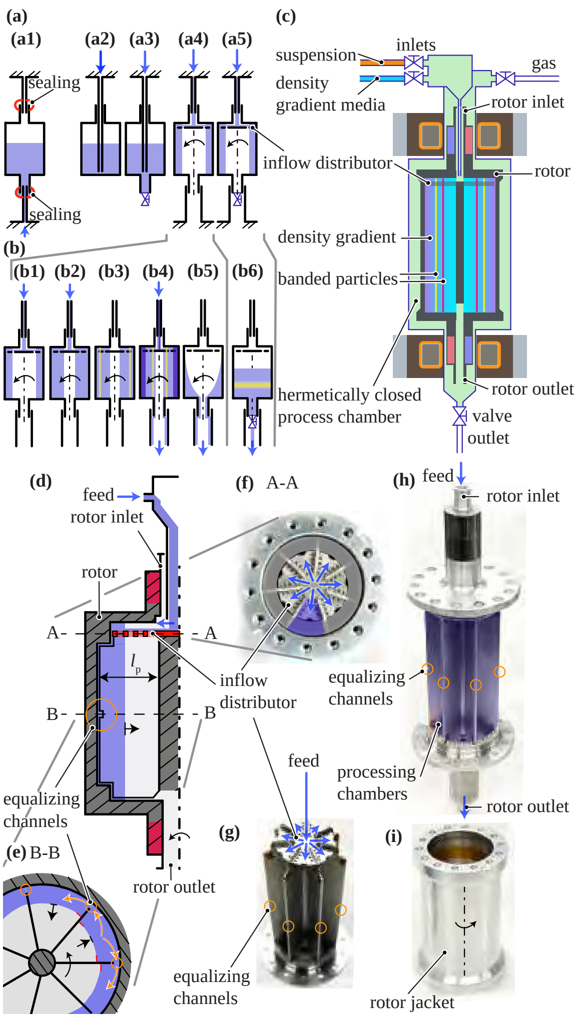

Fig. 3.14: **(a)** PUCF rotor topologies, **(b)** operating states of the selected novel SL-PUCF rotor topology, **(c)** novel SL-PUCF concept, **(d)** rotor section view showing the novel inflow distributor and the novel fil-level equalizing channels, **(e)** section view of the equalizing channels, **(f)** hardware realization of the inflow distributor, and **(g)** of the equalizing channels, **(h)** assembled rotor fluid path, **(i)** rotor jacket.

Tab. 3.8: Solution S5b: novel equalizing channels - main result.

S5b: problem remedy	main result
avoiding of rotor unbalance during filling	equalizing channels between divided rotor sectors let unbalanced liquid to level out, preventing rotor unbalance

3.4 Component C3: Burst Armor

The rotational energy E_{rot} of the SL-PUCF rotor increases quadratically with the rotational speed Ω:

$$E_{rot} = \frac{1}{2} J_z \Omega^2 \tag{3.21}$$

with J_z being the moment of inertia. Thus, the energy of a single rotor at 100 krpm corresponds to that of 100 rotors at 10 krpm. This shows the fragment containment challenge associated with ultra-high speeds. The rotational energy stored in the rotor of the presented SL-PUCF prototype at 100 krpm is 10.2 kJ. This corresponds approximately to the muzzle energy of five 5.56 mm caliber assault rifle projectiles [66]. A PUCF needs accordingly a burst armor to retain rotor fragments in the event of the rotor bursting. This is also specified in the standard DIN EN 12547 [67].

3.4.1 Technology Gaps for the Component Requirement RD; Openable Burst Armor

As only one SL-PUCF prototype exists for this chapter, a destructive rotor burst containment validation test is not possible within the scope of this chapter. The standard DIN EN 12547 [67] does not provide any guidelines for the burst armor design either. To the knowledge of the author, no first principles based design guideline was published in literature for a PUCF burst armor. To asses its feasibility to successfully contain the rotor fragments, a simplified containment analysis is conducted.

As a first conservative assumption, it is assumed that the entire rotor energy must be absorbed by the openable burst armor (O-BA) in the form of plastic deformation to keep it contained. Energy dissipation due to e.g. friction losses and rotor deformation is conservatively omitted. The maximum absorbable deformation energy $E_{def,max}$ is calculated as the plastic deformation energy up to ultimate elongation ϵ_{us}, but conservatively without plastic hardening. The maximum achievable radial material stress is therefore conservatively assumed to be the yield stress $\sigma_{r,max} = R_{p0.2}$:

$$E_{def,max} = R_{p0.2} \cdot A_{BA} \cdot L_0 \cdot \epsilon_{us}, \tag{3.22}$$

where $A_{BA} = w_{BA} \cdot h_{BA}$ is the O-BA material cross-section area. The inner circumference of the armor is conservatively used as the initial length $L_0 = 2\pi r_{BA,i}$. For the alloy steel 1.7225 / 42CrMo4 ($R_{p0.2} = 550$ Mpa, $\epsilon_{us} = 0.14$, $R_m = 800$ Mpa [68]), this results in an absorbable deformation energy of the armor with a thickness of 2 cm of 20.7 kJ. This corresponds to a safety factor of $\mathrm{SF_{a,r}} = 2$ of the burst armor against rupture. This shows the feasibility of the burst armor in general, not yet taking into account the opening joint weak points.

Problem P6: Joint Weak Points

However, to be openable, a hinge and a corresponding locking mechanism must be designed, that are able to withstand the forces that occur. The load has to be transferred through the joints without resembling weak points as the source of failure.

Solution S6: Joint Load Distribution

Fig.3.15(a) shows the SL-PUCF prototype with O-BA. The maximum average circumferential force F_{BA} that occurs in the armor shown in Fig.3.15(b) is conservatively:

$$F_{\mathrm{BA}} = \mathrm{R_{p0.2}} \cdot w_{\mathrm{BA}} \cdot h_{\mathrm{BA}}. \tag{3.23}$$

This force has to be transmitted by the armor bolts shown in Fig.3.15(c). Instead of subjecting the load to only one bolt cross-section which would be a weak point, N_{L} lugs are attached to the two O-BA halves, shown in Fig.3.15(d). They distribute the load over $(2 \cdot N_{\mathrm{L}} - 1)$ bolt cross-sections. Neglecting bending of the bolt, the corresponding shear stress $\tau_{\mathrm{b,N}}$ in the bolt cross-section A_{b} is

$$\tau_{\mathrm{b,N}} = \frac{\mathrm{R_m} \cdot w_{\mathrm{BA}} \cdot h_{\mathrm{BA}}}{A_{\mathrm{b}} \cdot (2 \cdot N_{\mathrm{L}} - 1)}. \tag{3.24}$$

The resulting shear stresses are shown in Fig.3.15(e). The safety factor against bolt rupture $\mathrm{SF_{b,r}}$ results as:

$$\mathrm{SF_{b,r}} = \frac{\tau_{\mathrm{sB}}}{\tau_{\mathrm{b,N}}} = \frac{f_{\mathrm{t}} \cdot \mathrm{R_m}}{\tau_{\mathrm{b,N}}} = \frac{f_{\mathrm{t}} \cdot A_{\mathrm{b}} \cdot (2 \cdot N_{\mathrm{L}} - 1)}{w_{\mathrm{BA}} \cdot h_{\mathrm{BA}}} \cdot \mathrm{SF_{a,r}}. \tag{3.25}$$

The factor $f_{\mathrm{t}} = \frac{\tau_{\mathrm{sB}}}{\mathrm{R_m}} = 0.58$ from [69] accounts for the reduced ultimate shear strength compared to the ultimate tensile strength of steel. $N = 1$, as in Fig.3.15(c), would result in too thick and heavy bolts for a hinge. With $N = 6$, as realized in the prototype Fig.3.15(a), the safety factor $\mathrm{SF} = 2$ can be maintained for a bolt diameter of 2 cm.

The realized O-BA furthermore covers the rotor end faces, to prevent fragments from escaping axially. At the separating interface, the inner surface is designed to overlap to avoid fragments from escaping in between. The two armor halves are additionally designed such, that they are of identical geometry but still fit together.

The presented solution is scalable in length for longer rotors without change in the safety factor.

Tab.3.9 summarizes the main findings of solution S6.

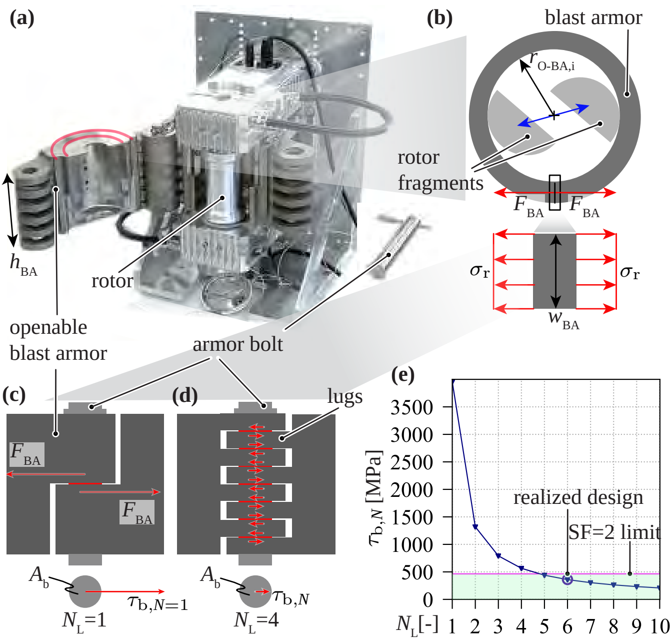

Fig. 3.15: (a) SL-PUCF prototype with novel openable rotor burst armor (O-BA) with joints. **(b)** Simplified model for occurring circumferential stress within the armor while containing a rotor burst. **(c)** Load transfer at the joint with one lug would result in high bolt shear load. **(d)** Multiple lugs reduce the stress level on the bolt with load distribution along the bolt. **(e)** Stress reduction in the bolt depending on number of lugs.

Tab. 3.9: Solution S6: joint load distribution - main result.

S6: problem remedy	main result
new concept for removing joint weak points in the openable burst armor	multiple lugs distribute the joint load along the bolt, reducing the bolt shear stress, enabling a safety factor > 2 for approximated dimensioning

3.5 Validation of Novel SL-PUCF System: Sedimentation of Whey Proteins as Test-Medium

The novel SL-PUCF concept is realized as a prototype. The SL-PUCF prototype was installed on a mobile laboratory unit together with the subsystems required for test operation, such as the mixing tank and feed pump, as shown in Fig.3.16(a). The SL-PUCF rotor was successfully accelerated across the axial resonance frequency to 2 krpm, validating Solution S1 and S2. Particles and water were mixed in the mixing tank and then fed to the SL-PUCF by a magnetically levitated feed pump (Levitronix PuraLev i30SU). Whey proteins are used as test particles, mixed in water with 20 g/L. Their harmless nature, smaller size than viruses, very low cost and great availability as common food supplement, render them as a very attractive test medium for general working principle validation.

Using the O-SBMs magnetic bearing functionality as a sensor makes it possible to monitor the SL-PUCF dynamic rotor filling process by measuring the SL-PUCF rotor weight, shown in Fig.3.16(b). It shows the rotor weight increase determined via the axial rotor position measurement during the dynamic filling of the SL-PUCF rotor at 2 krpm. It shows a constant feed rate, controlled by Levitronix Flow Control with the feed pump together with a inline Levitronix ultrasonic flow sensor. This validates experimentally, that the contact-less dynamic filling of the SL-PUCF rotor during stable levitated rotation from above via the inflow distributor works. This validates solutions S4-S5. After successfully filling of the SL-PUCF rotor, it was accelerated successfully stably suspended to 20 krpm.

Sedimentation was conducted as a first experimental validation of the basic functionality of the SL-PUCF rotor as a PUCF. The rotor was brought to zero rpm, and inspected, as shown in Fig.3.16(c). A layer of sedimented

Tab. 3.10: SL-PUCF: system validation - main results.

problem remedy	main results
passing of axial resonance frequency	successful, without rotor-housing contact
dynamic filling without fluid falling through rotor	successful
dynamic filling without destabilizing rotor unbalance	successful, stable suspension while filling
successful, stable high speed operation	20 krpm reached with filled rotor
rotor topology enables separation of particles	successful sedimentation of whey proteins at 20 krpm
operation without excessive winding surface temperature with passive cooling	successful, SL-PUCF operation at 20 krpm with winding surface temperature of 40.8° C

whey proteins was detected and therefore the separation successful. The basic separating function of the SL-PUCF has thus been experimentally validated.

The winding surface temperature of the O-SBM at 20 krpm was measured with only passive motor cooling to be 40.8° C, which confirms experimentally also during system operation the exceptionally good thermal properties of the novel MAFC for stator heat dissipation. Tab.3.10 summarizes the main findings of the SL-PUCF system validation.

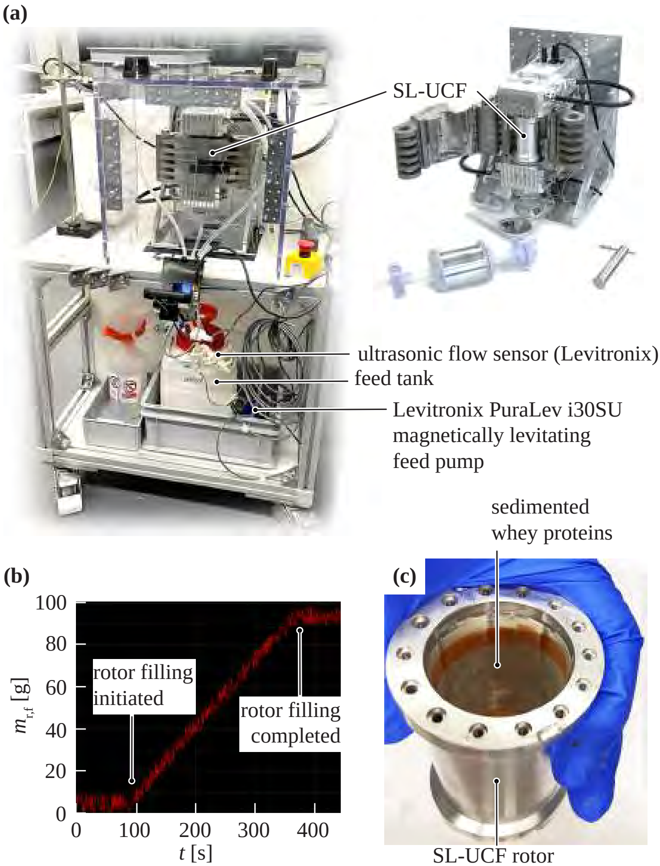

Fig. 3.16: (a) Novel SL-PUCF prototype connected to mixing tank, feed pump, and feed flow sensor and a camera to observe the turbidity of the feed and the outflow of the SL-PUCF. **(b)** Measured fill-level of the SL-PUCF rotor by converted measurement of the axial (vertical) rotor position during filling, using the axial stiffness k_{ax} of the O-DSBMs. **(c)** First test for validating the fundamental function as a centrifuge: successfully sedimented whey proteins at 20 krpm on the rotor jacket wall.

3.6 Outlook on Novel Future Smart Capabilitiy Potential of the proposed SL-PUCF concept

The following gives an outlook to new capabilities and benefits, that the new SL-PUCF concept can offer to the PUCF application. Three case studies are given, experimentally validating selected capabilities.

3.6.1 Sensing with O-SBMs as Sensors

Magnetic bearings can measure the radial and axial rotor position via their inherent function with position sensors. In literature, methods for contactless measurement of the rotor temperature via e.g. high frequency impedance measurement of the magnetic circuit from the stator to the rotor are described in [70]. This means, that contactless monitoring of the PUCF rotor temperature is also conceivable in the future. This would help to monitor the rotor and therefore also rotor fluid temperature without contact.

Furthermore, information on the rotor, or the entire system structure can be obtained by measuring frequency responses through the magnetic bearing excitation, additionally extended by measuring the acoustic frequency response, as shown in [71].

3.6.2 Sensing: Design Verification

The measurement of frequency responses can be used to verify the rotor dynamic properties of the rotor, including the bending resonance frequencies, to ensure that the rotor is sub-critical in the operating range. This is also possible during rotor rotation.

3.6.3 Sensing: Health Monitoring

The presented measurable system properties are conceivable to be used for health monitoring in the future. For example, a scan of the rotor resonance frequencies at standstill, before the speed is increased, is conceivable. A scan of the acoustic frequency response, according to [71], to check the overall structure is also conceivable. Possible detectable system faults are, e.g., missing screws or cracks in the rotor that shift the rotor resonance frequencies out of a permissible tolerance band. It should even be possible to identify different rotor types in this way by measuring the frequency response of the magnetic bearing excitation and / or the rotor weight.

3.6.4 Sensing: Ultracentrifugation Process Control

The ultracentrifugation process control potentially benefits in the future from the newly measurable properties. The SL-PUCF rotor fill-level measurement during operation makes it possible to monitor the filling process and thus avoid overfilling the rotor. During centrifuging, for example, it is also conceivable to track the rotor weight increase during continuous feeding for enrichment. In principle, sedimented particles will also be registered as an increase in weight during standstill. The emptying of the rotor can also be monitored accordingly.

The detection of error states is also conceivable. Acoustic monitoring of the structure as in [71] can also be combined with acoustic monitoring of the hermetically sealed process chamber.

3.6.5 Smart Capability Case Studies

O-SBMs as Sensors: Fill-Level Measurement

The axial magnetic bearing stiffness can as demonstrated be used to measure changes in the rotor weight due to the resulting axial displacement. Knowing the density of the added suspension, the fill-level in the rotor can be measured during filling, discharging or during operation. This rotor mass measurement is shown in Fig.3.16(b). The state of the completely filled rotor can be identified by the fact that the rotor weight does not increase any further during filling. Excess fluid exits directly at the rotor outlet. In principle, this even allows the density of the medium in the rotor to be determined, since the internal rotor volume is known.

Design Verification: Rotor Bending Resonance Measurement

To measure the rotor bending resonance frequencies, the excitation was carried out as described in [71]. The direction of the excitation, i.e. forward or backward, can be freely selected. Here the excitation was carried out backwards. Thus the backward whirl mode was excited. The bending resonance frequencies were found to lie above 3 kHz. The rotor resonance frequencies lie with sufficient reserve outside the first-order excitation (sub-critical), which at 100 krpm lies at 1.667 kHz. The measurement of the rotor bending resonance frequencies during rotation at 2 krpm showed the typical lowering of the resonance frequencies for backward whirls with increasing speed. The first and second backward whirl bending resonance frequencies have decreased from 3.7 kHz to 3.65 kHz and 4.17 kHz to 4.13 kHz respectively, due to the increased speed. This verifies, that the backward whirl modes were excited, showcasing the capability to measure entire Campbell diagrams.

Process Control: Acoustic Process Monitoring

A microphone for process chamber monitoring is attached to the connections for process gas handling. This allows detection of fault conditions such as overfilling of the rotor, resulting in asynchronously rotating fluid in the process chamber, foam formation and rotor emptying. Fig.3.17 shows exemplary the recorded channels of an external as well as an internal microphone which is connected to the inlets of the SL-PUCF during a commissioning experiments. Failure states like outflow of the rotor fluid, foam formation and wall contact, or stop of levitation leave distinct acoustic signatures. In the future, machine-learning based state recognition algorithms are conceivable.

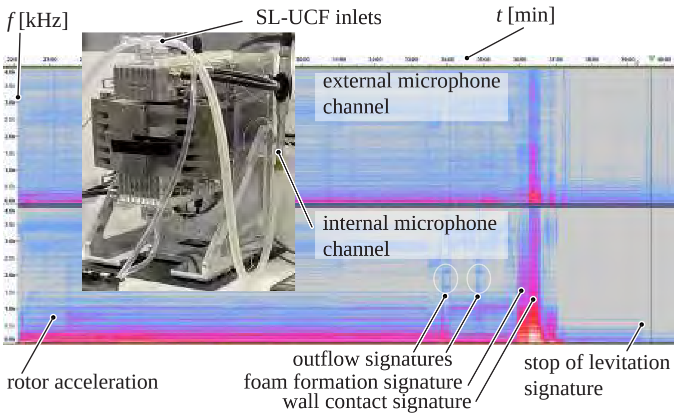

Fig. 3.17: External and internal microphone recording spectrogram during a commissioning experiment with visible failure state signatures, showcasing the potential of acoustic process monitoring.

3.7 Limitations and Future Improvements

This section discusses limitations and future improvements of the main novel solutions found in this chapter.

3.7.1 SL-PUCF Component Level Solutions

Solution S1: Yoke Interface Shoes

The proposed yoke interface shoes enable a RMS reduction of the axial stiffness ripple by 39% for a yoke air-gap surface increase of 33%. Their effect is limited to a reduction of the axial stiffness ripple to a tolerable level, but they cannot eliminate it completely.

As future improvements, larger reductions are conceivable with an even larger increase of the yoke air-gap surface, optionally also in axial direction. Furthermore, measures known from cogging torque reduction, e.g. forms of skewing, can e.g. by skewing the yoke air-gap potentially further contribute to the ripple reduction.

Applications beyond the scope of this chapter of yoke interface shoes are any new developments of openable self-bearing motors or openable magnetic bearings.

Solution S2: Rotor Magnet Design

A guideline for optimal magnet orientation offset is proposed. As shown, the rotor magnet design remains a compromise between axial stiffness reduction, motor and magnetic bearing performance, mechanics and rotor dynamics. Furthermore, reasoning for the magnet length and position dimension selection is given. As a limitation, only a compromise is possible.

Improvements are mainly possible by improving the yoke interface shoes, while following the optimal magnet orientation guide.

The presented guideline and reasoning are applicable for any new system with two openable self-bearing motors or magnetic bearings with a common rotor.

Solution S3: Macro-Filler Composite Thermal Bridge Material

The MAFC material is validated to increase the thermal conductivity of potting material by a factor of 3.4 to 4 W/mK, which results in a massive reduction in temperature of critical components. Limitations are the cost of a more complex manufacturing process and the minimal gap size due to the macro-filler particle dimensions. The increase in manufacturing complexity is justified for application, where the benefit of the temperature reduction while avoiding eddy current losses is critical.

For future improvement, a mixture of different size MAFC filler particles to increase the theoretical limit of the MAFC packing density is suggested.

However, it is a trade-off between thermal conductivity and high enough liquid characteristics which enable good surface contact.

Due to the MAFC particle dependent minimal gap size, MAFC is suited especially for applications with a large gap size or large volumes to be filled. Examples without limitation are electric machines, motors, self-bearing motors, magnetic bearings, motor windings or end-windings and magnetics in power electronics.

Solution S4: SL-PUCF Rotor Topology

The proposed SL-PUCF rotor topology is validated for the principal separation function by successful sedimentation of whey proteins. Its design is currently limited to dynamic filling and unloading during rotor rotation.

Future extension of the topology in Fig.3.14(a4) with a rotor-integrated valve as shown in Fig.3.14(a5) can additionally simplify the unloading process. The rotor can then be emptied slowly and in a controlled manner at standstill. The valve could conceivably be activated by centrifugal force, mechanically from below or (electro-) magnetically.

The proposed SL-PUCF topology is generally applicable to any sort of centrifugation or ultracentrifugation application, however, the process for each application needs to be validated individually.

Solution S5a: Inflow Distributor

The inflow distributor is validated in its function to prevent fluid from falling through the rotor during filling. However, the flow details at the inflow distributor during filling are unknown.

Future studies can investigate the detailed inflow distributor flow field to find optimization potential.

The inflow distributor can be interesting for any top filled bowel centrifuge.

Solution S5b: Equalizing Channels

The SL-PUCF rotor with equalizing channels enabled validated stable dynamic filling during rotation. It should be investigated in future studies, if they lead to unwanted mixing, disturbing the separation process, or if they have no negative impact.

In case this should be discovered in future studies to be an issue, their distribution, size, and shape can be subjected to an optimization. Generally, the concept of equalizing channels can be of interest in any application with a rotor containing rotating fluid, especially for self-bearing motor or magnetic bearing suspended rotors.

Solution S6: Joint Load Distribution

The newly derived approximate dimensioning of the novel openable burst armor showed a safety factor above two against rupture. Within this chapter, no rotor was accelerated until rotor burst, as the only prototype available should not be risked. In a future study, destructive burst tests with a rotational speed margin above the maximum rotor speed has to be conducted. The openable burst armor concept is generally applicable to any rotating machinery with needed rotor exchange or access and very high rotational energy to be contained.

3.7.2 SL-PUCF System

Expanding Operating Envelope

The proposed SL-PUCF is validated in its functionality. It is operated within this chapter at 20 krpm, to not risk destructive damage on this first prototype. In the precedent chapter, published in [18], the first generation O-SBMs without the improvements of this chapter, suspending horizontally instead of vertically a thin solid test-rotor, reached 103 krpm. The improved second generation of O-SBMs of this chapter therefore is highly likely to reach 100 krpm successfully also with a vertical rotor.

In a future study with more than one prototype available, the operating envelope will be successively expanded to higher rotational speeds. A vacuum system will be attached to lower the air pressure during high speeds to reduce rotor gas friction losses. A cooling system is foreseen around the process chamber to control the temperature of the rotor including its biotech payload. The full speed and power testing will also show the MAFCs performance under full load. However, the motor internal linearity of heat conduction with respect to the thermal resistance R_{Th} and the heat flux Q, $\Delta T = R_{\mathrm{Th}} \cdot Q$, combined with the MAFC thermal conductivity measurement and the very low winding surface temperature measurement result at 20 krpm, leads to the expectation of a very good thermal performance at 100 krpm as predicted.

Application Specific Development

The SL-PUCF functionality was validated with the sedimentation of whey proteins.

In a future study, the SL-PUCF rotor will be investigated and optimized further for the viral nanotechnology application. Application development for new biotech devices is extensive and requires further studies, focusing on this. The SL-PUCF offers many application specific optimization parameters, such as the radial path length, application of density gradients and process related modes, e.g. filling and unloading speeds, processing times and profiles. Once the application protocols are established and validated, the up-scaling of the LaS-PUCF prototype to PiS-PUCF and PrS-PUCF can be conducted.

The proposed SL-PUCF is generally unlimited to any biopharmaceutical and other purification application or to potential specialized applications even in clarification applications or other separation needs.

3.8 Conclusion

A novel sealless production ultracentrifuge type with two openable double self-bearing motors with novel features, tailored to vertically suspend its novel sealless rotor shielded by a novel openable burst armor was proposed and realized as a prototype. The current limitations of the state of the art of production ultracentrifuges for the manufacturing of viral vectors for gene therapies and vaccines were identified, system and component level requirements derived, component level problems identified, solutions presented and experimentally validated. This includes novel yoke interface shoes for openable self-bearing motor yokes, a guide to find optimal magnet alignment combinations and magnet dimensions for vertical rotor axis operation of such a system, the overcoming of axial bearing resonance, a novel scalable electrically insulating but highly thermally conductive macro-filler thermal bridge material for toroidal slotless ultra high-speed motors, a novel sealless flowpath design including a novel inflow distributor and equalizing channels and a novel openable ultracentrifuge burst armor. The general working principle of the novel sealless ultracentrifuge is validated experimentally by the successful sedimentation of whey proteins. Furthermore, an outlook is given to novel future capabilities for monitoring and process control thanks to the smart capabilities of the openable self-bearing motors and examples are experimentally demonstrated in the form of case studies.

The development trend for production ultracentrifuges stagnated. This chapter identified limitations of the state of the art and proposes solutions. The research described in this chapter aims at bringing ultracentrifuges ”back in the game” for future purification in viral nanotechnology, especially the separation of empty and full capsids.

The findings for the openable self-bearing motors to reduce the yoke air-gap influence can be used in any new application for openable self-bearing motors. The novel macro-filler composite thermal bridge material with an increased thermal conductivity by a factor of 3.4 compared to potting material can be of use for electric machines of any type in general to lower its (end-) winding temperatures or to increase power density.

4
Acoustic Diagnosis

This chapter summarizes the most relevant findings regarding the acoustic diagnosis of systems with active magnetic bearings, which are also published in:

- **E.J. Hubmann**, F. Weissofner, D. Steinert, T. Nussbaumer and J.W. Kolar, "Novel acoustic failure prediction method for active magnetic bearing systems," *IEEE/ASME Transactions on Mechatronics,* vol. 29, no. 2, pp. 1181-1192, 2024.

Chapter Abstract

For magnetic bearing manufacturers, the installation situations in systems in the field are often unknown and not accessible. Hence, the final system vibration spectrum with respect to excitations by operating the system and therefore mechanical resonances are unknown as well. But to avoid failure, they need to be known before the speed is initially ramped-up in a magnetic bearing suspended system. Therefore, there is a need for an experimental method to predict and prevent already at rotor standstill risks due to plant mechanical resonances. This chapter shows theoretically and experimentally that conventional magnetic bearing rotor displacement measurement is insensitive on mechanical system resonances. As a solution, two new acoustic response methods are proposed, which can completely detect the system mechanical resonances that will occur during operation already in the standstill levitating state. Furthermore, it is shown with application case studies, that these methods can be used for condition monitoring to detect deteriorating changes in the system before rotor speed ramp-up.

4.1 Introduction

Active magnetic bearings (AMBs) are installed as components into industrial systems. Their mechanical properties differ, leading to different system vibration (SV-)spectra and thus mechanical resonance frequencies of each system. These resonances are excited during operation if they correspond to the rotor speed Ω or harmonics thereof. This can lead to crash, damage or even destruction of parts of the system or long-term damage. To help in avoiding such expensive failures in AMB systems, the following prediction methods for AMB systems are needed: (i) experimental method for quantification of structural optimization attempts regarding dampening or shifting of mechanical resonances before speed ramp-up; (ii) identification prior to speed ramp-up of speed ranges in the operating range $[0, \Omega_{\max}]$, at which mechanical resonances are substantially excited in the system and therefore should be avoided for continuous operation (in this chapter called mechanical resonance speed ranges); (iii) condition monitoring of structural health allowing for health assessment before system is (re-)started. This chapter shows, that the state of the art methods are limited and how these limitations can be overcome with novel acoustics based methods. For all those methods, the SV-spectrum is needed before speed is ramped-up. It is state of the art

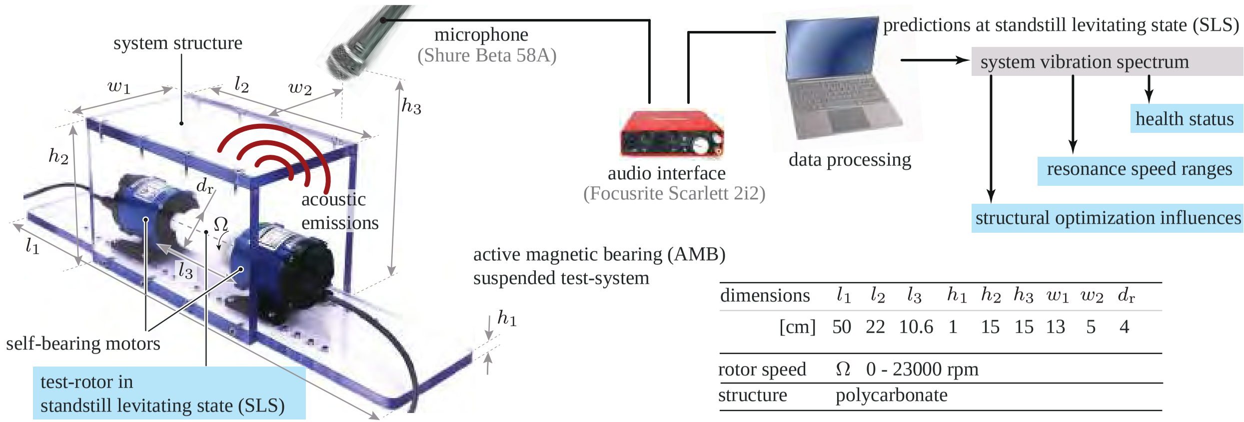

dimensions	l_1	l_2	l_3	h_1	h_2	h_3	w_1	w_2	d_r
[cm]	50	22	10.6	1	15	15	13	5	4
rotor speed	Ω 0 - 23000 rpm								
structure	polycarbonate								

Fig. 4.1: Proposed novel methods and the 23 krpm double self-bearing motor test system. Acoustic emissions of the active magnetic bearing (AMB) system are recorded with a microphone in the standstill levitating state (SLS). From this, the system vibration spectrum is obtained. Predictions on health status, mechanical resonance speed ranges and structural optimization influences can be made.

to diagnose AMB problems using the AMBs internal signals such as rotor displacement measurement (RD-M) [72]- [73]. An Internet of Things (IoT) application for processing those signals was reported recently in [74]. However, this chapter shows, that RD-M is not suited to gain the SV-spectrum needed. It is impossible with RD-M to detect vibrations that have a node at the AMBs RD-M sensing location, or that do not result in relative radial displacement between the rotor and stator there. The same applies if vibration sensors as in [75] would be used. Although these vibrations are not measurable by RD-M, they emit airborne (i.e. transmitted through air) acoustic emissions, with a new possibility for detecting them.

The use of airborne acoustic emissions for detection and diagnosis during operation of machines in general has been investigated in e.g. [76]- [77]. Additionally the monitoring of structure-borne (i.e. transmitted through the structure) noise in rotors with regard to crack formation has been investigated in e.g. [78]- [79]. However, this requires physical contact from the piezo-sensor to the spinning rotor body. This has been solved in the literature by wireless communication from the spinning rotor to the stationary evaluation device [78] or via a structure-borne sound conducting mechanical contact via the stationary outer ring of a ball bearing [79]. There, structure-borne noise generated by crack growth or plastic deformation in the range of several 100 kHz is measured by a bonded sensor. Therefore, the occurrence of degradation events in the rotor during operation can be detected, but not the health state as such.

In [80] a procedure was proposed to monitor cracks in rotors suspended with mechanical bearings and using an AMB as an excitation source only and position sensors to measure the differing rotor response to the excitation in the presence of a rotor crack.

However, for systems with AMBs, the usage of the information conveyed in the airborne acoustic domain for diagnosis or assessment is not covered in literature so far to the knowledge of the author, although the field of AMBs is a very active field of research. Only few efforts touching acoustics in AMB systems for other purposes were reported. In [81] the control signal filtering procedure for reduction of AMB acoustic noise due to electromagnetic interference (EMI) was reported. In [82] the AMB was used to generate anti-noise to reduce fluid dynamic induced noise from an AMB suspended fan. Recently an advanced control strategy to reduce vibrations (i.e. also acoustic noise) of magnetically suspended rotors was reported in [83]. The monitoring and diagnosis of the application process related quality in machining was reported in [84], [85].

In contrast to the field of systems with AMBs, the acoustic emissions were more in focus of research activities for mechanically suspended electric motors. They may be grouped into the three topics: asset diagnosis, emission prediction and mitigation. Two recent publications addressed the condition monitoring of electric motors with data fusion of acoustic and motor data. In [86], electric faults and faults of rotating parts were diagnosed combined acoustically and with winding current data. In [87], acoustic data was combined with vibration sensor data targeting ball bearing damage. The prediction and mitigation of acoustic emissions of mechanically suspended electric machines gained increasing attention in the last years with the rise of electric vehicle (EV) technology. To model, predict and reduce noise, vibration and harshness (NVH) emissions of electric machine designs, which would be experienced by passengers, simulation frameworks were reported. With modern commercially available software it is possible to listen to a digital motor-model in operation already during the design phase [88]. This enables design optimizations incorporating the acoustic footprint of electric machines. Example application targets of these activities were EV traction motors, [89]- [90], or a high-speed air compressor motor for fuel cell EVs [91]. None of these reported works fulfill the three needs stated in the beginning of this section. As a solution, the novel methods presented in this chapter provide the needed SV-spectrum based on airborne acoustic emissions, already in the standstill levitating state (SLS) before the speed is ramped up. In the following, "airborne" is assumed but no longer explicitly stated. Fig. 4.1 illustrates the methods. A double self-bearing motor test-system (i.e. AMB and motor function combined in one unit) with rotor speeds of up to 23 krpm from [92] is used along with acoustic recording and processing equipment to demonstrate the novel methods. In a levitating standstill state (SLS) of the rotor, i.e. before speed-ramp up, acoustically the SV-spectrum is measured. It can then be used for experimental structural optimization quantification, identification of mechanical resonance speed ranges or structural health monitoring.

In Section 4.2 the capability of RD-M to measure the SV-spectrum is investigated with the aid of a mathematical system model. The RD-M is shown to fail to measure the SV-spectrum in the model. Two acoustic disturbance force excitation (DF-E) response measurement methods are introduced in Section 4.3. They serve as a basis for the acoustic prediction of mechanical resonances in standstill levitating state. This methods are validated with 3D-FEM modal analysis and a speed ramp-up experiment in Section 4.4. It is shown experimentally that the AMB RD-M fails to measure the SV-spectrum.

Three case studies for the application of the novel methods are presented in Section 4.5. Section 4.6 summarizes the main findings and concludes the chapter.

4.2 Mechanical Resonance Measurement: AMB-Limitations and Acoustics Advantages

In their ability to measure mechanical vibrations, RD-M and acoustic emission measurement (AE-M) differ in two basic principles. First, RD-M measures only locally, whereas AE-M can sense emissions from vibrations throughout the entire system. Thus, RD-M cannot measure vibration modes with vibration nodes at the RD-M locations whereas AE-M can, because of its global nature. Second, the physical quantity being measured is different. The RD-M measures a physical distance between two objects, AE-M measures sound waves. Vibrating parts emit sound waves, i.e. they can be measured by AE-M. Further, it is unclear how the RD-M is related to vibrations. This is investigated in the following by breaking the system down into mass-spring-damper ($mkd-$)element sub-components and discussion of their individual DF-ER in Section 4.2.1 and by mathematically modeling the combined system and investigating its combined DF-ER to rotor forces in Section 4.2.2.

4.2.1 System Model mkd-Sub-Components

Fig. 4.2(a) shows a simplified model of the test-system depicted in Fig. 4.1. Sub-components exhibiting vibration modes are represented lumped as spring symbols k_i. Each of these sub-components possesses an attributed mass and damping. This results in ($mkd-$)elements, which are described in the following:
As commonly done [93], an AMB with proportional-derivative (PD) position control (cf. [94]) can be modeled as a spring-damper (k_B, d_B) element if linearized at the operating point. In the test-system, the rotor position is radially actively controlled whereas axially it is passively stabilized by reluctance forces. The AMB stiffness in Fig. 4.2(a) is thus further distinguished into the radial stiffness $k_\mathrm{B,r}$ and the axial $k_\mathrm{B,ax}$ one. The stiffnesses for bending modes are generalized indicated as: rotor k_R, self-bearing motor stator k_A and structural $k_{\mathrm{S},i}$ bending stiffnesses. The mounting support stiffness is labelled as k_M.
For simplicity and generalization, in Fig. 4.2(b), the complexity of the system

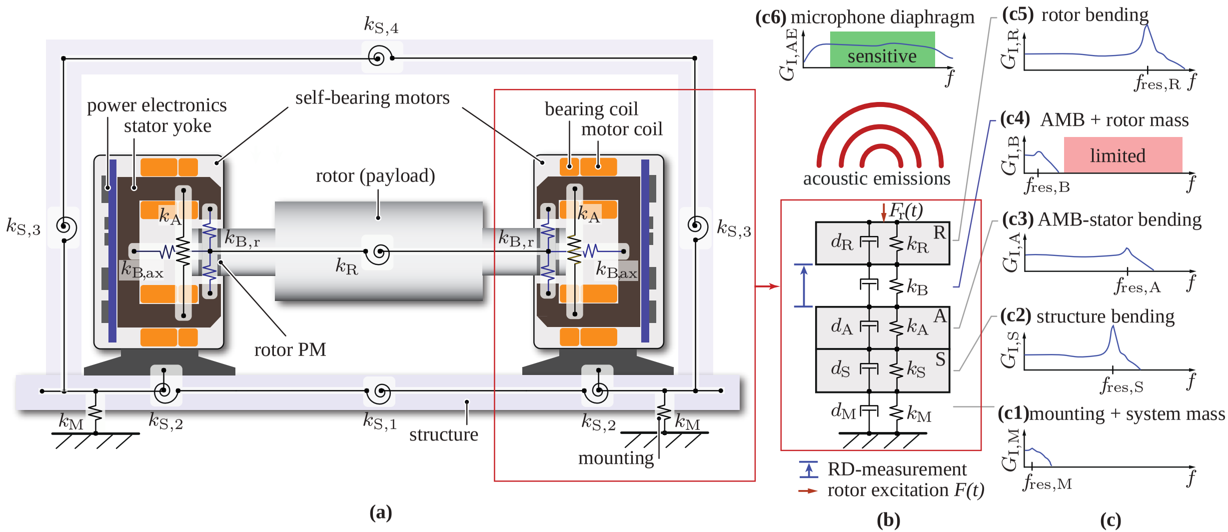

Fig. 4.2: **(a)** Simplified conceptual model of the test-system with stiffnesses k_i: rotor bending stiffness k_R, AMB stiffness k_B, AMB-stator bending stiffnesses k_A, system structure stiffnesses k_S and mounting stiffness k_M. **(b)** Further simplified model in abstracted form. **(c)** Typical individual disturbance force excitation response $G_{I,i}$ to force excitation on the corresponding mass m_i of the sub-components.

model is further reduced. In Fig. 4.2(c), the individual DF-ERs $G_{\mathrm{I,i}}$ from the disturbance force excitation F_i on the corresponding mass m_i to the deflection x_i of the sub-elements from Fig. 4.2(b) are qualitatively shown.
All modeled sub-elements behave individually as $mkd-$elements. They represent a second order system. Newton's second law yields:

$$m_i\ddot{x}_i = -k_i x_i - d_i\dot{x}_i + F_i(t). \tag{4.1}$$

Resulting in the sub-component transfer function (TF) $H_i(s)$ from disturbance force excitation $F_i(t)$ on the mass m_i to the position x_i

$$H_i(s) = \frac{X_i(s)}{F_i(s)} = \frac{1}{m_i s^2 + d_i s + k_i}, \tag{4.2}$$

which for no damping d_i leads to a resonance frequency $f_{\mathrm{res},i}$ of

$$f_{\mathrm{res},i} = \frac{1}{2\pi} \cdot \sqrt{\frac{k_i}{m_i}} \tag{4.3}$$

Above $f_{\mathrm{res},i}$, the $mkd-$elements show a low-pass filter characteristic. The coupling of the test-system to ground in Fig. 4.2(c1) is done in a soft way. It was placed on a foam matt resulting in a $f_{\mathrm{res,M}}$ in the range of 60 Hz. Structural resonances in Fig. 4.2(c2) show higher $f_{\mathrm{res,S}}$. The same holds for AMB stator bending $f_{\mathrm{res,A}}$ in Fig. 4.2(c3). In contrast to that, the combination of rotor mass and AMB stiffness in Fig. 4.2(c4) leads to very low $f_{\mathrm{res,B}}$, in the test-system in the range of 24 Hz (axial), 45 Hz (cylindrical) 70 – 100 Hz (conical modes) [92]. Rotor bending modes of the test-system in Fig. 4.2(c5) show $f_{\mathrm{res,R}}$ above 1.5 kHz [92]. The sensitivity of a microphone diaphragm in Fig. 4.2(c6) remains high over a large frequency range due to its low inertia. The used microphone in this chapter, Shure Beta 58A, has a high sensitivity in the range of 50 Hz – 16 kHz [47].

4.2.2 Combined DF-ERs and AMB Relative Normalized Vibration Amplitude Estimation Error

To investigate the combined DF-ERs to rotor forces, the $mkd-$model in Fig. 4.2b) is further simplified by omitting the low frequency mounting support k_{M}, resulting in the $mkd-$model in Fig. 4.3(a). In the following, a state space system representation of the $mkd-$model is derived in the form:

$$\dot{\underline{x}} = \underline{A} \cdot \underline{x} + \underline{B} \cdot \underline{u} \tag{4.4}$$

$$\underline{y} = \underline{C} \cdot \underline{x} \,. \tag{4.5}$$

The individual distances x_i between the masses m_i, and their time derivatives serve as the system states $\underline{x}$. As inputs $\underline{u}$ serve the constant neutral (zero force) distances x_i^0 of the springs k_i and the time varying rotor excitation force $F_\mathrm{r}(t)$

$$\begin{bmatrix} \dot{x}_\mathrm{A} \\ \dot{x}_\mathrm{B} \\ \dot{x}_\mathrm{C} \end{bmatrix} := \begin{bmatrix} x_4 \\ x_5 \\ x_6 \end{bmatrix}, \; \underline{x} = \begin{bmatrix} x_\mathrm{A} \\ x_\mathrm{B} \\ x_\mathrm{C} \\ x_4 \\ x_5 \\ x_6 \end{bmatrix}, \; \underline{u} = \begin{bmatrix} x_\mathrm{A}^0 \\ x_\mathrm{B}^0 \\ x_\mathrm{C}^0 \\ F_\mathrm{r}(t) \\ 0 \\ 0 \end{bmatrix}. \tag{4.6}$$

With Δ_i being the deflection of the corresponding mkd−element:

$$\Delta_\mathrm{i} = x_\mathrm{i} - x_\mathrm{i}^0 , \tag{4.7}$$

Newton's second law yields:

$$m_\mathrm{S} \cdot \ddot{x}_\mathrm{S} = -\Delta_\mathrm{S} k_\mathrm{S} - \dot{x}_\mathrm{S} d_\mathrm{S} + \Delta_\mathrm{A} k_\mathrm{A} + \dot{x}_\mathrm{A} d_\mathrm{A} \tag{4.8}$$

$$m_\mathrm{A} \cdot (\ddot{x}_\mathrm{S} + \ddot{x}_\mathrm{A}) = -\Delta_\mathrm{A} k_\mathrm{A} - \dot{x}_\mathrm{A} d_\mathrm{A} + \Delta_\mathrm{B} k_\mathrm{B} + \dot{x}_\mathrm{B} d_\mathrm{B} \tag{4.9}$$

$$m_\mathrm{B} \cdot (\ddot{x}_\mathrm{S} + \ddot{x}_\mathrm{A} + \ddot{x}_\mathrm{B}) = -\Delta_\mathrm{B} k_\mathrm{B} - \dot{x}_\mathrm{B} d_\mathrm{B} + F_\mathrm{r}(t) . \tag{4.10}$$

Accordingly the system matrices of the state space representation can be derived to:

$$\underline{A} = \begin{bmatrix} 0 & 0 & 0 & 1 & 0 & 0 \\ 0 & 0 & 0 & 0 & 1 & 0 \\ 0 & 0 & 0 & 0 & 0 & 1 \\ -\frac{k_\mathrm{S}}{m_\mathrm{S}} & \frac{k_\mathrm{A}}{m_\mathrm{S}} & 0 & -\frac{d_\mathrm{S}}{m_\mathrm{S}} & \frac{d_\mathrm{A}}{m_\mathrm{S}} & 0 \\ \frac{k_\mathrm{S}}{m_\mathrm{S}} & -\frac{k_\mathrm{A}}{m_\mathrm{S}} - \frac{k_\mathrm{A}}{m_\mathrm{A}} & \frac{k_\mathrm{B}}{m_\mathrm{A}} & \frac{d_\mathrm{S}}{m_\mathrm{S}} & -\frac{d_\mathrm{A}}{m_\mathrm{S}} - \frac{d_\mathrm{A}}{m_\mathrm{A}} & \frac{d_\mathrm{B}}{m_\mathrm{A}} \\ 0 & \frac{k_\mathrm{A}}{m_\mathrm{A}} & -\frac{k_\mathrm{B}}{m_\mathrm{A}} - \frac{k_\mathrm{B}}{m_\mathrm{B}} & 0 & \frac{d_\mathrm{A}}{m_\mathrm{A}} & -\frac{d_\mathrm{B}}{m_\mathrm{A}} - \frac{d_\mathrm{B}}{m_\mathrm{B}} \end{bmatrix} \tag{4.11}$$

$$\underline{B} = \begin{bmatrix} 0 & 0 & 0 & 0 & 0 & 0 \\ 0 & 0 & 0 & 0 & 0 & 0 \\ 0 & 0 & 0 & 0 & 0 & 0 \\ \frac{k_\mathrm{S}}{m_\mathrm{S}} & -\frac{k_\mathrm{A}}{m_\mathrm{S}} & 0 & 0 & 0 & 0 \\ -\frac{k_\mathrm{S}}{m_\mathrm{S}} & \frac{k_\mathrm{A}}{m_\mathrm{S}} + \frac{k_\mathrm{A}}{m_\mathrm{A}} & -\frac{k_\mathrm{B}}{m_\mathrm{A}} & 0 & 0 & 0 \\ 0 & -\frac{k_\mathrm{A}}{m_\mathrm{A}} & \frac{k_\mathrm{B}}{m_\mathrm{A}} + \frac{k_\mathrm{B}}{m_\mathrm{B}} & \frac{1}{m_\mathrm{B}} & 0 & 0 \end{bmatrix}. \tag{4.12}$$

$\underline{C}$ is an identity matrix, returning the states $\underline{x}$ in the output $\underline{y}$. With this state space representation, the DF-ERs were computed for all three $mkd-$elements w.r.t the rotor excitation, presented in Fig. 4.3(b). Thereby the model parameters shown in Fig. 4.3(c) were used. The bearing stiffness k_B corresponds to the measured value of the test system from [92]. Compared to its low k_B and high d_B, high structural stiffness (k_A,k_S) and low structural damping (d_A,d_S) was analyzed to represent structural behavior. The AMB RD-M shows for low frequencies a damped resonance and for higher frequencies a low-pass filter characteristic and two anti-resonances in Fig. 4.3(b1). In the presence of RD-M sensor noise, those anti-resonances are partially covered by the noise. In contrast to the RD-M, both structure-related $mkd-$systems show two distinct resonances in Fig. 4.3(b2)-(b3). Therefore the rotor excitation force $F_\mathrm{r}(t)$ at those frequencies excites mechanical resonances, whereas the AMB $mkd-$system is not excited, it even shows anti-resonances. To quantify how well the AMB RD-M can measure the mechanical resonances, the AMB relative normalized vibration amplitude estimation error $e_\mathrm{vib,r,n}$ is introduced as:

$$e_\mathrm{vib,r,n}(f) = \frac{\hat{x}_\mathrm{B}(f)}{\hat{x}_\mathrm{i}(f)} \cdot \frac{\hat{x}_\mathrm{i}(f=0)}{\hat{x}_\mathrm{B}(f=0)} \, . \tag{4.13}$$

If the DF-ER of the AMB RD-M captures the vibrations, then it is proportional to the DF-ERs of the vibrations, i.e. showing the same response characteristic. In that case, $e_\mathrm{vib,r,n} = 1$. If the AMB RD-M underestimates vibrations then $e_\mathrm{vib,r,n} < 1$, if it overestimates, $e_\mathrm{vib,r,n} > 1$. Fig. 4.3(d) shows $e_\mathrm{vib,r,n}$ for the two structural $mkd-$sub-components. For frequencies lower then the RD-M DF-ER bandwidth $B_\mathrm{RD-M}$, $e_\mathrm{vib,r,n}$ is very close to 1. It should be noted, that $B_\mathrm{RP-M}$ is defined by the $mkd-$property of the AMB together with the rotor mass. I.e. no matter how high the bandwidth of an actual position sensor is, the physical quantity measured defines already the upper limit $B_\mathrm{RD-M}$. Above $B_\mathrm{RD-M}$, $e_\mathrm{vib,r,n}$ increasingly deviates from 1, even with sign changes. The mechanical resonances are underestimated by order of magnitudes. The AMB RD-M therefore fails to measure the vibrations present in the system model. This is in alignment with experiences in other fields: In a system with many resonance frequencies, the energy concentrates in the vibration modes with excitation matching resonance frequency. This is exploited in tuned resonators for damping of unwanted resonances as reported in [95] - [96]. It is applied for example in bridges, skyscrapers or stringed musical instruments (e.g. ”wolftone” eliminator on a cello). Therefore AMB RD-M shows substantial deficiencies in measuring vibrations, whereas AE-M shows promising characteristics. This is investigated in the following sections.

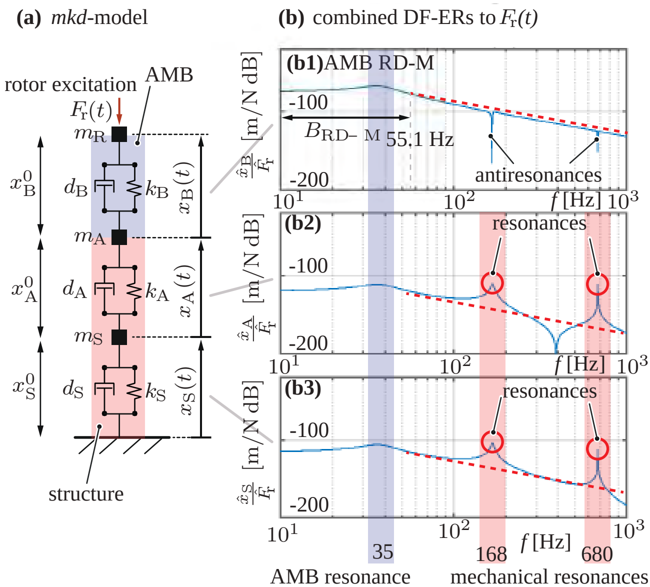

(c) *mkd*-model parameters

k [kN/m]		m [kg]		d [Ns²/m]		x [m]	
k_B	5.6	m_R	0.1	d_B	10	x_B^0	0.001
k_A	1000	m_A	0.3	d_A	0.01	x_A^0	0.1
k_S	600	m_S	0.1	d_S	0.01	x_S^0	0.1

(d) AMB relative normalized vibration amplitude estimation error $e_{vib,r}$

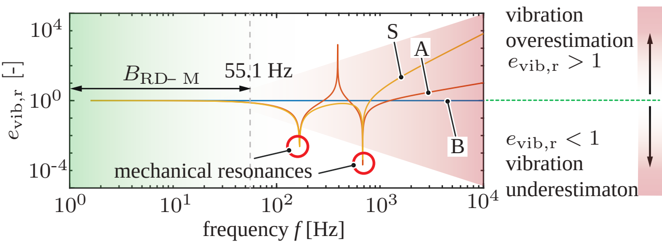

Fig. 4.3: (a) *mkd*–model used for the mathematical analysis. **(b)** Combined disturbance force excitation responses (DF-ERs) from rotor force excitation $F_r(t)$ to the corresponding deflections x_i. **(c)** *mkd*-Model parameters of the analysis. **(d)** AMB relative normalized vibration amplitude estimation error.

4.3 Acoustic DF-ER Measurement Methods - Basis for Acoustic Prediction of Mechanical Resonances and Validation Thereof

The active nature of AMBs enables to measure system DF-ERs by exciting and measuring a response, shown for example in [97]. For this purpose, in the standstill levitating state (SLS) a disturbance force excitation DF-E is realized by superimposing a corresponding excitation current $\underline{i}_{\mathrm{e}}$ component on the reference bearing current $\underline{i}_{\mathrm{b,ref}}$. In [98] and [99], instead or additionally to the excitation with one discrete frequency f_{k}, a noise component was superimposed on $\underline{i}_{\mathrm{b,ref}}$. In [100], separate excitation winding turns were wound onto the AMB Stator.
Fig. 4.4 shows the two approaches for using the AMB itself as an excitation source: in Fig. 4.4(a) the excitation current $\underline{i}_{\mathrm{ed}}$ with a discrete frequency and in Fig. 4.4(b) the excitation with noise n. Both are resumed in this chapter, but in a new form. Instead of the RD-M response, the AE-M system response is measured for both methods. Further, instead of superimposing artificial noise, the naturally present noise in the bearing current is used. Ultimately, the bearing current superpositions lead to additional forces $\underline{F}_{\mathrm{i,ed}}$ and $\underline{F}_{\mathrm{i,en}}$ between rotor and stator. They act like the reference bearing current $\underline{i}_{\mathrm{b,ref}}$ generated nominal bearing force itself $\underline{F}_{\mathrm{i,b}}$ or like unbalance excitations $\underline{F}_{\mathrm{u}}$ or passive magnetic forces $\underline{F}_{\mathrm{x,sr}}$. Since, these magnetic forces also act on the stator they excite the structure with a force $\underline{F}_{\mathrm{AMB,structure}}$. In [73], $\underline{F}_{\mathrm{AMB,structure}}$ was measured and modeled for a Lorentz-type AMB where (in contrast to the AMBs of the test-system in this chapter) the passive reluctance force relationships $\mathrm{F}_{\mathrm{x,sr}}$ in Fig. 4.4 played a minor role compared to the current dependent ones $\mathrm{F}_{\mathrm{i,sr}}$. AMB-stator internal forces $\underline{F}_{\mathrm{i,ss}}$ are parasitically generated in the same way and are a possible additional contributor to the system structure excitation.
In the following section, the two types of DF-E methods and corresponding acoustic response measurements are explained in detail.

4.3.1 Acoustic Discrete DF-ER in SLS

A discrete DF-E with one frequency, which is then varied over a frequency range, was realized as a spatially rotating disturbance force vector $\underline{F}_{\mathrm{i,ed}}$. This was implemented by superimposing a sine component corresponding to the excitation frequency in the x-direction and a cosine component in the y-direction.

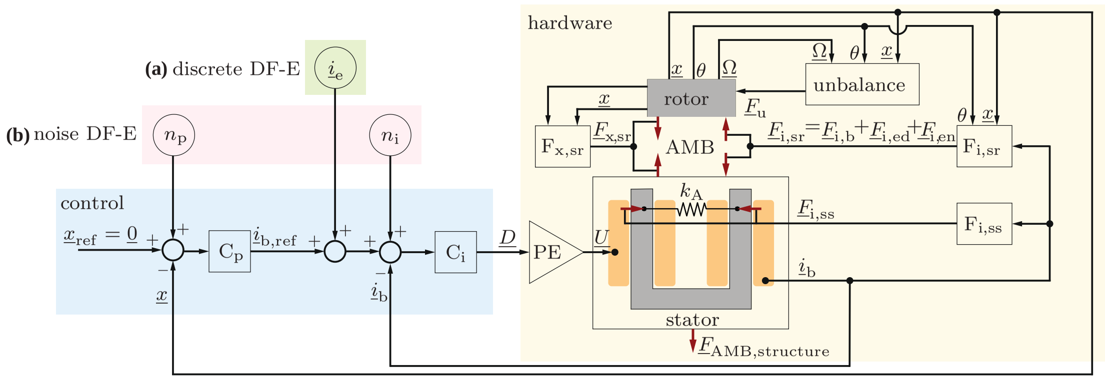

Fig. 4.4: The two proposed excitation methods are: **(a)** active superimposed discrete disturbance force excitation (discrete DF-E) as i_e on the reference current at the output of the position controller C_p and **(b)** noise disturbance force excitation (noise DF-E) as the coupling of noise sources by e.g. noise n_p on the position signal or noise n_i on the current measurement. Resulting excitation forces between stator and rotor $\underline{F}_{i,ed}$ and $\underline{F}_{i,en}$ are superimposed on the nominal magnetic bearing force $\underline{F}_{i,b}$ actively generated by the reference bearing current $\underline{i}_{b,ref}$. Further during rotation, unbalance forces $\underline{F}_u$ excite the rotor and passive magnetic reluctance forces $\underline{F}_{x,sr}$ excite both rotor and stator. Additionally, excitation forces are generated internally to the stator $\underline{F}_{i,ss}$.

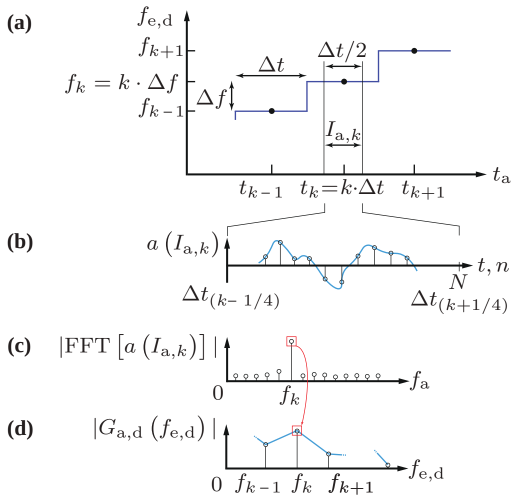

Fig. 4.5: **(a)** Realization of discrete DF-E, **(b)** extraction of half hold-period sized evaluation interval $I_{a,k}$ for each hold period Δt, **(c)** discrete Fast Fourier Transform (FFT) of the evaluation interval data, **(d)** interpretation of the extracted FFT amplitude of the respective discrete excitation frequency f_k as the k-th acoustic discrete DF-ER $|G_{a,d}|$.

Fig. 4.5 shows the measurement and evaluation procedure. The discrete DF-E was realized as a staircase-shaped discrete frequency sweep presented in Fig. 4.5(a). For each hold period Δt, a half hold-period sized evaluation interval $I_{a,k}$ of the acoustic signal was extracted from the permanently running acoustic recording as presented in Fig. 4.5(b). The evaluation interval $I_{a,k}$ was subsequently subjected to the discrete Fast Fourier Transform (FFT) Fig. 4.5(c). The amplitude of the respective discrete excitation frequency f_k was extracted and interpreted as the k-th acoustic discrete DF-ER $|G_{a,d}|$ as displayed in Fig. 4.5(d).

4.3.2 Acoustic Natural Bearing Current Noise DF-ER in SLS

The natural noise on the bearing current, which is present in normal operation, i.e. not generated artificially, leads to a DF-E, albeit of very small amplitude. Unavoidable sources of current noise n_i and position measurements noise n_p could be of thermal, $1/f$ decaying (with frequency f) [101], and electro-

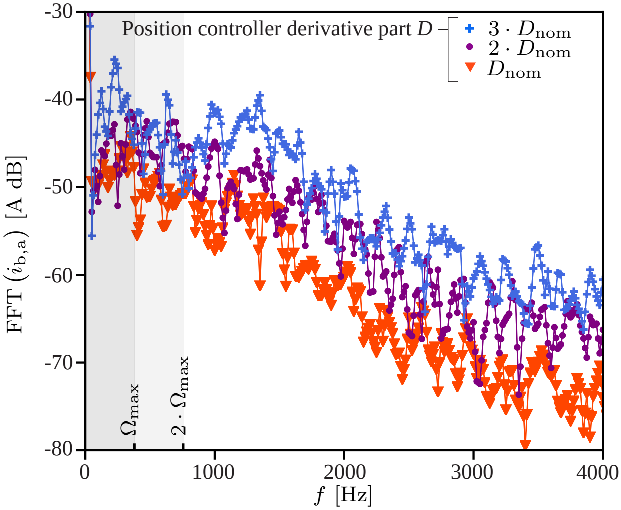

Fig. 4.6: Example measurement of the bearing current noise spectrum of one bearing phase by FFT transformation of the current measured on the oscilloscope. The bearing current noise spectrum is shown for nominal, doubled and tripled position controller D-part. The noise spectrum is relatively flat in the operating range of the AMB and its magnitude increases with increasing position controller D-part.

magnetic interference [81] nature. An exemplary measured bearing current frequency spectrum is shown in Fig. 4.6. The noise spectrum is relatively flat in the operating range up to the maximum speed $\Omega_{\max}$. This low frequency noise cannot be filtered without impairing the position control. To prove the influence of the position measurement noise, the derivative part (D-part) of the PID position controller was doubled and tripled from the nominal value and the corresponding frequency spectrum was measured. The noise amplitude increases with a higher D-part, thus confirming the suspected correlations. This also means that within control stability limits, the D-part could be used to artificially increase the noise level. With the nominal D-part, the resulting acoustic noise was barely audible, nevertheless this nominal value was kept constant for all following investigations. To measure the acoustic response to the natural bearing current noise, a short audio sequence was recorded with the rotor in SLS. The FFT of this recording sequence directly yields the acoustic noise DF-ER.

4.4 Validation of Acoustic Mechanical Resonance Prediction in SLS and Failure of AMB RD-M to Achieve the Same

Both in Section 4.3 presented acoustic DF-ER measurement methods in SLS were applied to predict the mechanical resonances of the test-system shown in Fig. 4.7(a)-(b). This prediction was successfully validated first with 3D-FEM modal analysis of the test system Fig. 4.7(a) and second with a speed ramp-up of the test system Fig. 4.7(c). As proposed by the derived theory in Section 4.2, the DF-ER of the RD-M at SLS shown in Fig. 4.7(d) failed to predict the mechanical resonances, supporting the theory. In the speed ramp up experiment, the RD-M did not show signs of mechanical resonance detection capability in Fig. 4.7(d), i.e. the detection failed. This is in accordance with the presented theory in Section 4.2. In summary, the acoustic mechanical resonance prediction in SLS was validated with simulation and experiment. Furthermore, the theory in Section 4.2 was found to be supported by the failure of AMB RD-M to predict in SLS and to detect during operation the mechanical resonances. In the following, the details of the measurements are discussed.
For the validation of the proposed theory and methods, the frequency range was defined to cover frequencies up to twice the rotational frequency (excitation order EO = 2) at a maximum test system speed of $\Omega_{\mathrm{max}} = 23\,\mathrm{krpm}$ ($383\,\mathrm{rev/s}$), i.e. $0 - 800\,\mathrm{Hz}$. This was done to cover the range, where the main excitations occur during rotating operation, as for higher EOs the excitation magnitude drops. In electric machines, due to the non-ideal field shapes, higher harmonics also occur in the magnetic forces and lead to higher order excitations as shown in e.g. [89]. For the acoustic measurements, the sound pressure levels provided are normalized pressures p_{rel}, which by normalization with $p_0 = 20\,\mu\mathrm{Pa}$, (calibrated at $400\,\mathrm{Hz}$ with testo 816-1 sound pressure level measurement unit, testo SE & Co. KGaA, Lenzkirch, Germany). For the discrete DF-E, an amplitude of $400\,\mathrm{mA}$ was superimposed on the reference bearing current $\underline{i}_{\mathrm{b,ref}}$.
The prediction of mechanical resonances with acoustic discrete DF-ER in SLS in Fig. 4.7(a) shows distinct peaks. They are validated twice as mechanical resonances, once with mechanical eigenmodes obtained by 3D FEM modal analysis in Fig. 4.7(a) and once with the speed ramp-up in Fig. 4.7(c).
The acoustic noise DF-ER Fig. 4.7(b) and the discrete one in Fig. 4.7(a) show the same SV-spectrum profile with very good agreement. The noise DF-ER signal is two orders of magnitude weaker, but does not show less information

content. I.e. similar information from discrete DF-ER can be obtained by noise DF-ER. It further confirms the cause effect chain in Fig. 4.4. This similarity means, that the same double validation as for the discrete DF-ER applies similarly for this noise based method.
The validation experiment in Fig. 4.7(c) is a a speed ramp-up from $0 - 23$ krpm. The same procedure as for the discrete DF-ER was used for evaluation, but instead of artificial excitation, the natural excitations due to speed ramp-up operation were present. Simultaneously both EO=1 and EO=2 were evaluated for each rotational speed Ω. Deviations in magnitude compared to the discrete and noise DF-ER were expected due to the different nature of excitation. Vibration modes with natural frequencies higher than the maximum rotational frequency of the rotor are excited by the excitations with EO $= 2$ during the run-up, and these peaks also agree with the acoustic predictions in SLS (Fig. 4.7(a) and Fig. 4.7(b)). The acoustic predictions in SLS and speed ramp-up validation experiment are further compared with the AMB internal RD-M shown in Fig. 4.7(d). Neither the maximum or average rotor displacement $|\underline{x}|_{\mathrm{max}}$ and $|\underline{x}|_{\mathrm{avg}}$) nor the measured bearing currents (maximum and average magnitude of bearing current space vector $|\underline{i}_{\mathrm{b}}|_{\mathrm{max}}$ and $|\underline{i}_{\mathrm{b}}|_{\mathrm{avg}}$) show distinct resonance peaks corresponding to the validation experiment in Fig. 4.7(c). Only in the region of the AMB-rotor $mkd-$self-resonances in Fig. 4.7(f), large peaks in the measured rotor position $|\underline{x}_{\mathrm{r}}|$ are found. Slightly above these resonances, the low-pass filter characteristic of the AMB becomes apparent with decreasing rotor displacements in accordance with the theory in Section 4.2. Also during speed ramp-up no signs of mechanical resonance induced peaks were found in the AMB internal RD-M and bearing currents shown in Fig. 4.7(e). Above its resonance frequency, the AMB becomes self-centering. Geometric rotor asymmetries are still perceived ($< 50\,\mu$m for this test-system) due to the high position sensor bandwidth. Force rejection methods as summarized in [102] and [103] allow the position sensors to ignore those supposed oscillations and letting the rotor rotate around its principal axis of inertia, explaining the asymptotically reached rotor deflection offset. In accordance with the theory in Section 4.2, the AMB failed to detect the mechanical resonances occurring during operation.
Summarizing, the theoretical considerations in Section 4.2 are confirmed experimentally. Both acoustic methods that were introduced to predict mechanical resonances in SLS were successfully validated with 3D-FEM modal analysis and experimentally, while as expected the AMB RD-M failed to achieve that prediction.

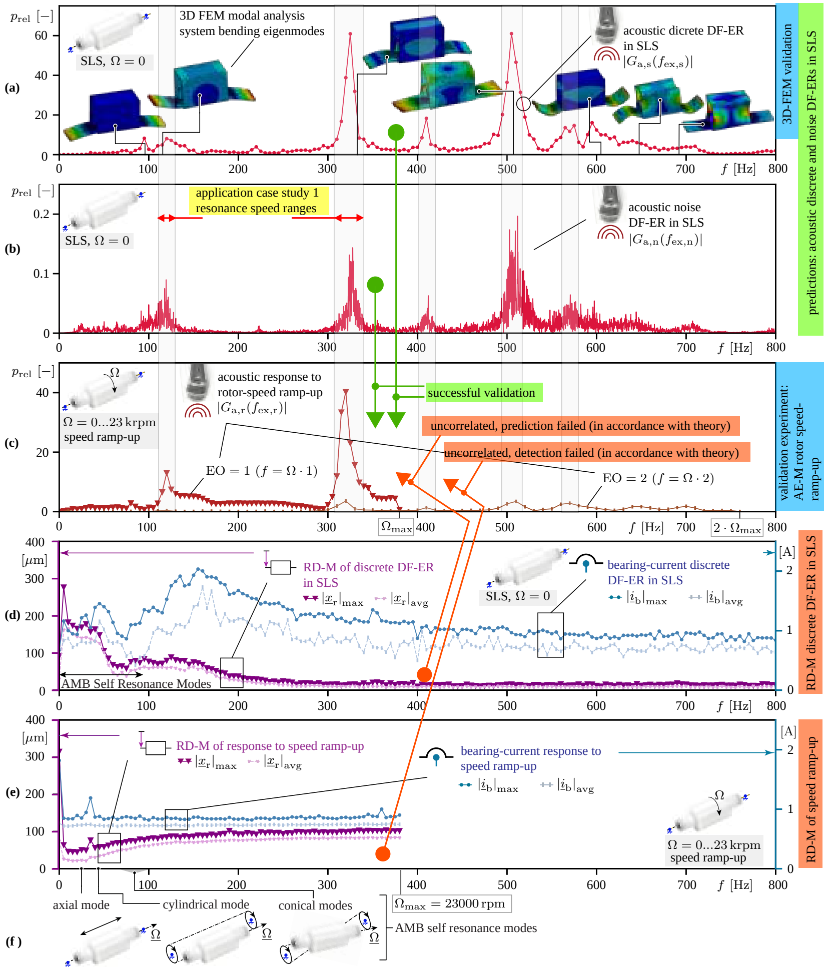

Fig. 4.7: (a) Successful prediction of mechanical resonances with acoustic discrete DF-ER in SLS and 3D-FEM validation of the acoustic SV-spectrum predictions. **(b)** Successful prediction of mechanical resonances with acoustic noise DF-ER in SLS and application case study one: identification of mechanical resonance speed ranges. **(c)** Validation experiment: acoustic response to rotor speed ramp-up, validation of AE-M predictions. **(d)** Failed RD-M prediction of the SV-spectrum in accordance with the theory. **(e)** Failed RD-M detection of mechanical resonances during rotor speed ramp-up in accordance with the theory. **(f)** Indicated AMB self resonance modes.

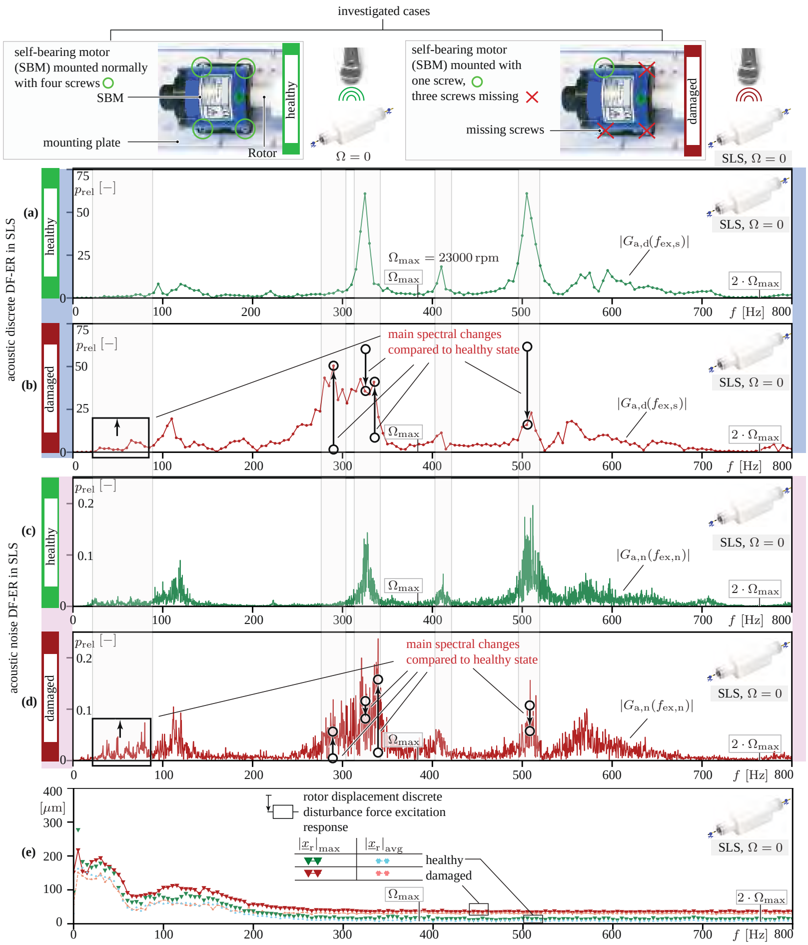

Fig. 4.8: Acoustic failure risk prediction: comparison of the acoustic DF-ERs between a healthy state and a damaged state with three missing SBM mounting screws. Acoustic discrete DF-ER is shown in **(a)** for the healthy system condition and **(b)** in damaged state with main spectral changes indicated. **(c)** Acoustic noise DF-ER in healthy state, **(d)** in damaged condition with main spectral changes. Significant amplitude differences in the SV-spectrum are evident in the acoustic responses **(e)** AMB RD-M of the discrete DF-ER in healthy and damaged state.

4.5 Acoustic Failure Prediction at Standstill

In Section 4.4 it was shown that both proposed acoustic DF-ER methods can provide a SV-spectrum. A healthy system possesses a certain characteristic SV-spectrum. It can therefore serve as a reference, against which condition monitoring can be done. Faults which result in a change in the SV-spectrum due to e.g. change in stiffnesses, damping, mass distributions or excitation transmission change can therefore be detected. In the following, this capability is exemplary demonstrated with three application case studies. By means of the two acoustic methods presented in this chapter, it is possible to detect such a system fault acoustically even in SLS before the speed is ramped up, i.e. predict a potential system failure before it can occur.

4.5.1 Application Case Study 1: Mechanical Resonance Speed Ranges

Both noise and discrete DF-ER prediction of the SV-spectrum are used to identify mechanical resonance speed ranges. These speed ranges should be excluded from continuous operation due to excessive mechanical vibrations. They are shown in Fig. 4.7(b). It should be noted however, that resonance frequencies that do not originate from the stationary structure but from the rotor, can deviate from the value identified at SLS with increasing speed due to gyroscopic effects.

4.5.2 Application Case Study 2: Lost AMB Mounting Screws

Three out of four fastening screws of one AMB were removed, which represents a severe fault with system failure potential. The fault resulted in a change in the SV-spectrum. The acoustic discrete DF-ER in SLS is shown in Fig. 4.8(a) in healthy and in Fig. 4.8(b) in damaged condition. Fig. 4.8(c) shows the acoustic noise DF-ER in SLS in healthy, Fig. 4.8(d) in damaged condition. Significant amplitude differences in the SV-spectra are evident for both acoustic predictions and are indicated. The corresponding acoustic responses for both methods for the same system condition match well, i.e. both are capable of predicting the system fault at SLS already. The lost stiffness due to the missing screws leads to increased vibration amplitude in the RD-M. However, changes in the SV-spectrum are not unveiled by RD-M. While a fault close to the RD-M location can be detected by RD-M, as the next case study shows, more remote faults cannot be detected by RD-M but with the acoustic methods.

4.5.3 Application Case Study 3: Forgotten Maintenance Tool

To show the higher sensitivity of the proposed acoustic methods compared to the AMB RD-M with increasing distance to the RD-M sensing location, a case is shown exemplary, where the acoustic noise based method can detect the presence of a forgotten maintenance wrench lying on the test-system. The spectogram in Fig. 4.9(a) shows the spectral difference when the wrench is placed (W) compared to when it is not (N). It was placed four times and removed four times, which is clearly visible in the presented spectogram. Fig. 4.9(b) shows the difference in the noise DF-ER between this two cases. The SV-spectrum changes in Fig. 4.9(a) are identified in Fig. 4.9(b) in form of non-symmetric difference peaks which differ from the symmetric peaks due to noisy signals. The noise DF-ER method is accordingly sensitive enough to detect a wrench placed on the test system already in SLS. The AMB RD-M shows in Fig. 4.9(c) no signs of detection of the differences. In accordance with the presented theory in this chapter it does not correlate with the SV-spectrum.

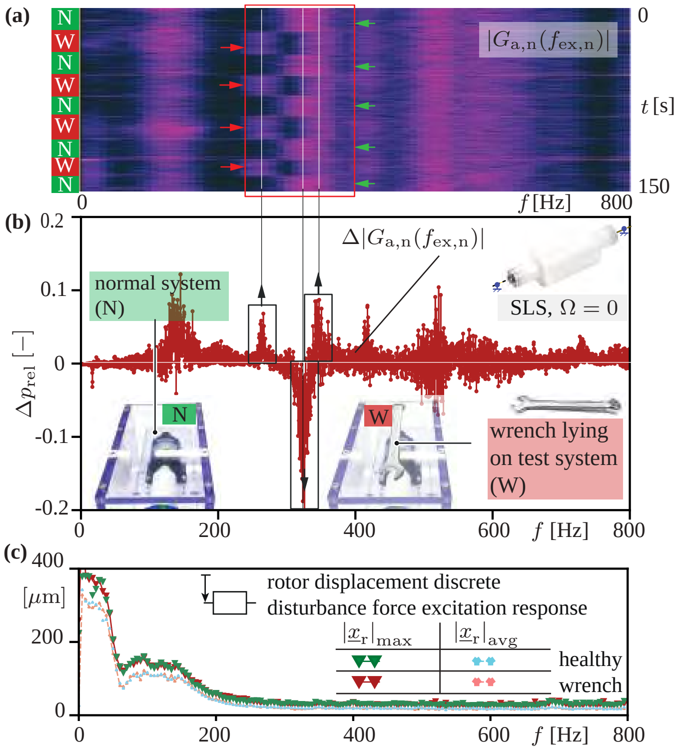

Fig. 4.9: **(a)** Spectrogram of noise DF-ER of repeated wrench placement on the test-system at SLS, with indication of the normal system without wrench (N) and with wrench (W). **(b)** Difference of noise DF-ERs with and without wrench at SLS. **(c)** RD-M of discrete DF-ER with and without wrench.

4.6 Conclusion

In this chapter, it was shown with theory and experimentally that rotor displacement measurement fails to adequately measure mechanical resonances of AMB systems. Two novel acoustic disturbance force excitation response methods to predict the system vibration spectrum already in standstill levitating state were presented. They were further validated with 3D-FEM modal analysis and experimental ramp-up of the rotor speed. Three application case studies were presented: identification of mechanical resonance speed ranges already at standstill levitating state, detection of missing AMB mounting screws and detection of a forgotten maintenance tool lying on the test-system housing. System failure risks can therefore be predicted safely before rotor speed is ramped-up. The fast measurement procedure, in case of the natural noise response even instantaneous feedback, allows for future live trial and error system optimization, e.g. adding dampers or stiffening elements, with quantifiable evaluation of the applied measures. The demonstrated capability for condition monitoring may be used in the future to capture acoustic ”fingerprints” of industrial AMB systems, and their condition monitoring. Future applications may combine the presented methods with data-processing methods including machine learning.

5 Conclusion

This dissertation addresses the limitations of state of the art production ultracentrifuges for the biopharmaceutical industry, which have so far prevented them from widespread use in purification processes. As a potential solution, a novel sealless production ultracentrifuge with its drive and magnetic bearing system consisting of openable self-bearing motors, is proposed, realized as a prototype and operated to a rotational speed of 103 krpm. The proposed concepts enable a novel hermetically contained, fast exchangeable, sealless production ultracentrifuge process chamber. The whole system was realized as a prototype. Its working principle was validated experimentally by sedimentation of whey proteins as a test medium. The introduction of self-bearing motors to production ultracentrifuges opens new capabilities for system diagnosis. Novel acoustic methods were proposed to determine the system vibration spectrum already at standstill by using the self-bearing motors as an excitation source. It was experimentally validated in case studies, that already at standstill levitating state, system defects can be successfully diagnosed by acoustic methods, before the speed is ramped up. This enables the potential for preventive maintenance, before a production ultracentrifuge with defects is ramped up to very high speeds, risking massive damage.

In the course of these main findings, the following novel solutions to identified challenges were found.

5.1 Novel Openable Self-Bearing Motors

- The novel openable self-bearing motors render rotary seals, mechanical bearings and damping elements unnecessary. They allow for a hermetically enclosed process chamber incorporating the rotor. The connected inlet and outlet tubes can stay connected, i.e. maintaning sterility, while exchanging the whole rotor unit. This solves any contamination issues in both directions, to the outside and from the outside, while enabling extremely small batch changeover times.

- Adverse effects caused by the unavoidable yoke air-gaps in the novel openable self-bearing motors were discovered: a) parasitic induced voltages, resulting in parasitic induced currents, caused by the flux variations due to the rotor angle dependent reluctance, generating undesired stator losses. b) axial magnetic bearing stiffness ripple appears for vertical rotor operation of openable self-bearing motors, which hinders the passing of the axial magnetic bearing resonance frequency. Two measures were found and successfully implemented to reduce the parasitic induced currents to an acceptable level. On the one hand, phase L-filters were found to reduce their amplitude. On the other hand, a current control scheme with a parasitic current feed-forward control was proposed. To reduce the axial magnetic bearing stiffness ripple, the root cause has been identified. As a countermeasure, novel yoke interface shoes are introduced, which reduces the rotor angle dependent reluctance variation. This helps also for the other yoke air-gap caused adverse effects. Furthermore, guides to find the optimal magnet orientation offset combinations of the two rotor magnets and the magnet dimensions for vertical rotor operation, as required for PUCFs, was derived.

- Stray fields of high-speed toroidally wound slotless motors prevent the direct cooling of the windings with an electrically conductive cooling jacket due to eddy current loss generation at very high speeds. A novel electrically insulating macro-filler composite (MAFC) material, containing highly thermally conductive macroscopic aluminum oxide ceramics spheres is proposed and successfully measured to improve the potting thermal conductivity by a factor of 3.4.

- The ability of the proposed openable self-bearing motors to achieve very high rotational speeds was experimentally demonstrated by reaching 103 krpm.

5.2 Novel Sealless Production Ultracentrifuge Type

- To avoid crossing of the first flexural bending mode of the rotor, the rotor was designed to operate subcritical. This was verified with 3D-FEM modal analysis, acoustic impact response measurement, and rotor frequency response measurement with the aid of the self-bearing motors as actuators.

- In case of burst, high kinetic energy containing rotor fragments need to be contained. An openable burst armor concept was proposed to still allow for fast exchange of the hermetically enclosed process chamber. The openable burst armor feasibility to contain rotor fragments is supported by a theoretical analysis.

- The omitted rotary seals require a new sealless rotor flow path concept to avoid the fluid from falling through the rotor without filling the rotor. A method was proposed, which enables dynamic filling of the rotor during rotation. A novel inlet distributor avoids fluid from falling through the rotor during filling. Equalizing channels ensure balanced fluid distribution in all rotor chambers. The general working principle was experimentally verified by the successful sedimentation of whey proteins.

5.3 Novel Acoustic Diagnosis Methods

- To prevent damage by system failures during high-speed operation due to undetected system faults, a system diagnose method is desired, which is applicable before speed ramp-up. The magnetic bearing functionality enables new opportunities to diagnose the system by exciting it and measuring a response. However, it was found theoretically and experimentally that the rotor displacement measurement fails to adequately measure mechanical resonances in the stationary system structure. Therefore, two novel acoustic disturbance force excitation response measurement methods to predict the system vibration spectrum already in standstill levitating state were presented and validated experimentally. They allow to analyze the structural resonances of the system already before the speed is ramped up. In case studies it was shown, that already in standstill levitating state, system defects can be diagnosed. They can thus be repaired before they cause further damage in operation.

5.4 Outlook

The proposed solutions to the identified major problems of the state-of-the-art production ultracentrifuges preventing them from widespread use in purification for biopharmaceutical products are experimentally validated within this dissertation. They represent one step towards bringing ultracentrifugation back into consideration as a candidate for the purification of biopharmaceutical products in industrial large-scale production, with the advantage of the capability to separate by density or sedimentation coefficient. The presented sealless production ultracentrifuge concept has the potential to serve as a basis for a future alternative to chromatography or a complementing polishing step.

The foundation is laid for a new type of production ultracentrifuge, on which future biopharmaceutical research can build to refine the rotor and process design to specific biopharmaceutical purification process needs.

The proposed production ultracentrifuge concept is a potential technology candidate to help solving the problem of undesired immune reactions to empty or partially empty capsids in viral vector therapies.

The proposed ultracentrifuge potentially can serve additional applications in the chemical industry, for example in the production of nano-particles.

The proposed openable self-bearing motor technology potentially also can find further applications in biopharmaceutical and chemical industry, where a fast exchange of hermetically enclosed rotors can be beneficial.

The proposed cost effective macro-filler composite thermal bridge material can find use in other applications such as the heat extraction of very high-speed electric machine stators or magnetic components in power electronics.

Acoustic diagnosis of structural properties in systems suspended by magnetic levitation already during standstill can be of use in different industries as well. Preventive maintenance of high asset systems like power plant generators or turbines, industrial compressors, or kinetic energy storage could benefit from this form of system diagnosis, to prevent damage. The identification and monitoring could be enhanced by artificial intelligence in the future.

Bibliography

[1] S. A. Al Shehri, A. Al-Sulaiman, S. Azmi, and S. S. Alshehri, "Biosafety and bio-security: A major global concern for ongoing COVID-19 pandemic," *Saudi Journal of Biological Sciences*, vol. 29, no. 1, pp. 132–139, 2022, DOI: 10.1016/j.sjbs.2021.08.060.

[2] M. M. Segura, A. A. Kamen, and A. Garnier, "Overview of current scalable methods for purification of viral vectors," *Viral Vectors for Gene Therapy: Methods and Protocols*, pp. 89–116, 2011, DOI: 10.1007/978-1-61779-095-9_4.

[3] A. L. Gimpel, G. Katsikis, S. Sha, A. J. Maloney, M. S. Hong, T. N. Nguyen, J. Wolfrum, S. L. Springs, A. J. Sinskey, S. R. Manalis *et al.*, "Analytical methods for process and product characterization of recombinant adeno-associated virus-based gene therapies," *Molecular Therapy-Methods & Clinical Development*, vol. 20, pp. 740–754, 2021, DOI: 10.1016/j.omtm.2021.02.010.

[4] P. C. F. Pau, J. Berg, and W. McMillan, "Application of Stokes' law to ions in aqueous solution," *Journal of Physical Chemistry*, vol. 94, no. 6, pp. 2671–2679, 1990, DOI: 10.1021/j100369a080.

[5] A. Gooders, N. Webb, G. Allen, and B. Richards, "Total containment of a continuous-flow zonal centrifuge," *Biotechnology and Bioengineering*, vol. 23, no. 1, pp. 1–18, 1981, DOI: 10.1002/bit.260230102.

[6] T. Svedberg, "Nobel lectures, chemistry 1926: The ultracentrifuge, May 19, 1927," *Nobel Lectures*, vol. 1, no. 1, 1995.

[7] T. Svedberg and J. Nichols, "The application of the oil turbine type of ultracentrifuge to the study of the stability region of carbon monoxide-hemoglobin," *Journal of the American Chemical Society*, vol. 49, no. 11, pp. 2920–2934, 1927, DOI: 10.1021/ja01410a046.

[8] P. Allaire, R. Humphris, and D. Lewis, "Professor Jesse W. Beams and the first practical magnetic suspension," in *International Symposium on Magnetic Suspension Technology, Part 2*, 1992, pp. 25–32.

[9] N. G. Anderson, "The zonal ultracentrifuge. A new instrument for fractionating mixtures of particles," *The Journal of Physical Chemistry*, vol. 66, no. 10, pp. 1984–1989, 1962, DOI: 10.1021/j100816a039.

[10] C. S. Plüisch, B. Bössenecker, L. Dobler, and A. Wittemann, "Zonal rotor centrifugation revisited: New horizons in sorting nanoparticles," *RSC Advances*, vol. 9, no. 47, pp. 27 549–27 559, 2019, DOI: 10.1039/C9RA05140F.

[11] N. G. Anderson, "Preparative particle separation in density gradients," *Quarterly Reviews of Biophysics*, vol. 1, no. 3, pp. 217–263, 1968, DOI: 10.1017/S0033583500000561.

[12] T. Perardi, R. Leffler, and N. Anderson, "K-series centrifuges II. Performance of the k-II rotor," *Analytical Biochemistry*, vol. 32, no. 3, pp. 495–511, 1969, DOI: 10.1016/S0003-2697(69)80015-1.

[13] T. Perardi and N. G. Anderson, "K-series centrifuges: III. Effect of core taper on particle capture efficiency," *Analytical Biochemistry*, vol. 34, no. 1, pp. 112–122, 1970, DOI: 10.1016/0003-2697(70)90091-6.

[14] J. Brantley, D. Willis, J. Breillatt, R. Gibson, L. Patrick, and N. Anderson, "K-series centrifuges: IV. Measurement and control of temperature," *Analytical Biochemistry*, vol. 36, no. 2, pp. 434–442, 1970.

[15] N. Cho, J. Breillatt, J. Brantley, and N. Anderson, "K-II centrifuge flow improvement," 1971.

[16] N. G. Anderson, J. L. Gerin, and N. L. Anderson, "Global screening for human viral pathogens," *Emerging Infectious Diseases*, vol. 9, no. 7, pp. 768–773, 2003, DOI: 10.3201/eid0907.030004.

[17] M. Konrath, J. Gorenflo, N. Hübner, and H. Nirschl, "Application of magnetic bearing technology in high-speed centrifugation," *Chemical Engineering Science*, vol. 147, pp. 65–73, 2016, DOI: 10.1016/j.ces.2016.03.025.

[18] E. J. Hubmann, R. Eberhard, C. F. Blaser, S. Erismann, D. Steinert, T. Nussbaumer, and J. W. Kolar, "Magnetically self-bearing drive system for ultracentrifugation: Towards 100'000 rpm and 200'000g," *IEEE Transactions on Industry Applications*, vol. 60, no. 1, pp. 321–331, 2023, DOI: 10.1109/TIA.2023.3314016.

[19] A. Hashimoto, A. Matsui, M. Motohashi, N. Miyake, H. Ota, Y. Nakanishi, and H. Nishimura, "P-pw-02 a novel motor manufacturing technology using spiral type core for information devices," in *in Proc. of*

JSME-IIP/ASME-ISPS Joint Conference on Micromechatronics for Information and Precision Equipment: IIP/ISPS joint MIPE. The Japan Society of Mechanical Engineers, 2003, pp. 403–404, DOI: 10.1299/jsmemipe.2003.403.

[20] J. Chen, J. Zhu, and E. L. Severson, "Review of bearingless motor technology for significant power applications," *IEEE Transactions on Industry Applications*, vol. 56, no. 2, pp. 1377–1388, 2019, DOI: 10.1109/TIA.2019.2963381.

[21] T. Pei, D. Li, J. Liu, J. Li, and W. Kong, "Review of bearingless synchronous motors: Principle and topology," *IEEE Transactions on Transportation Electrification*, vol. 8, no. 3, pp. 3489–3502, 2022, DOI: 10.1109/TTE.2022.3164420.

[22] B. S. Weinreb, M. Noh, D. C. Fyler, and D. L. Trumper, "Design and implementation of a novel interior permanent magnet bearingless slice motor," *IEEE Transactions on Industry Applications*, vol. 57, no. 6, pp. 6774–6782, 2021, DOI: 10.1109/TIA.2021.3080663.

[23] J. Asama and A. Chiba, "Three-coil combined winding configuration for a 2-DOF actively controlled bearingless permanent magnet motor," *IEEE Transactions on Industry Applications*, vol. 57, no. 6, pp. 6765–6773, 2021, DOI: 10.1109/TIA.2021.3078665.

[24] I. Bagaric, D. Steinert, T. Nussbaumer, and J. W. Kolar, "Concept of a novel bearingless three-pole motor for two-sided driven applications," in *in IEEE 24th International Conference on Electrical Machines and Systems (ICEMS)*, 2021, pp. 99–104, DOI: 10.23919/ICEMS52562.2021.9634649.

[25] J. Asama, Y. Kamiya, and A. Chiba, "Asymmetrical four-phase combined winding arrangement for bearingless PM motors," *IEEE Transactions on Industry Applications*, vol. 57, no. 6, pp. 6870–6879, 2021, DOI: 10.1109/TIA.2021.3089447.

[26] Z. Wen, G. Valente, A. Formentini, L. Papini, C. Gerada, and P. Zanchetta, "A novel current limitation technique exploiting the maximum capability of power electronic inverter and bearingless machine," *IEEE Transactions on Industry Applications*, vol. 57, no. 6, pp. 7012–7023, 2021, DOI: 10.1109/TIA.2021.3069149.

[27] T. Noguchi, H. Sugimoto, Y. Fujii, and A. Chiba, "A novel combined winding and test result of a 20-pole/24-slot consequent-pole bearingless motor with parallel motor winding," *IEEE Transactions on Industry Applications*, vol. 57, no. 6, pp. 6880–6891, 2021, DOI: 10.1109/TIA.2021.3096485.

[28] N. Petersen, A. Khamitov, T. Slininger, and E. L. Severson, "Machine design and precision current regulation for the parallel DPNV bearingless motor winding," *IEEE Transactions on Industry Applications*, vol. 57, no. 6, pp. 7000–7011, 2021, DOI: 10.1109/TIA.2021.3059717.

[29] D. Dietz and A. Binder, "Design guidelines and scaling effects for bearingless PM synchronous machines accounting for eddy current reaction field," *IEEE Transactions on Industry Applications*, vol. 57, no. 6, pp. 6844–6855, 2021, DOI: 10.1109/TIA.2021.3083673.

[30] G. B. Gallego, L. Rossini, T. Achtnich, D. M. Araujo, and Y. Perriard, "Efficiency optimization of slotless magnetic-bearing machines," *IEEE Transactions on Industry Applications*, vol. 57, no. 6, pp. 6833–6843, 2021, DOI: 10.1109/TIA.2021.3072614.

[31] H. Sugimoto and A. Chiba, "Dynamic modeling and experimental validations of passing through critical speeds by high acceleration in one-axis actively positioned bearingless motors," *IEEE Transactions on Industry Applications*, vol. 57, no. 6, pp. 6956–6964, 2021, DOI: 10.1109/TIA.2021.3079169.

[32] N. Petersen, T. Slininger, and E. L. Severson, "State observers and runout reduction for magnetically levitated motor systems," *IEEE Transactions on Industry Applications*, vol. 59, no. 2, pp. 1812–1823, 2022, DOI: 10.1109/TIA.2022.3226134.

[33] D. Kepsu, R. P. Jastrzebski, and O. Pyrhönen, "Modeling of a 30 000 rpm bearingless SPM drive with loss and thermal analyses for a 0.5 MW high-temperature heat pump," *IEEE Transactions on Industry Applications*, vol. 57, no. 6, pp. 6965–6976, 2021, DOI: 10.1109/TIA.2021.3087118.

[34] T. Srichiangsa, H. Sugimoto, Y. Fujii, and A. Chiba, "Design, development, and experimental results of a 30 000-r/min one-axis actively positioned single-drive bearingless motor," *IEEE Transactions on Industry Applications*, vol. 57, no. 6, pp. 6783–6791, 2021, DOI: 10.1109/TIA.2021.3090736.

[35] J. Asama, "Design of slotless single-drive bearingless permanent magnet motor for high-speed applications," in *in Proc. of IEEE International Power Electronics Conference (IPEC-Himeji 2022-ECCE Asia)*, 2022, pp. 397–400, DOI: 10.23919/IPEC-Himeji2022-ECCE53331.2022.9806840.

[36] Y. Fu, M. Takemoto, S. Ogasawara, and K. Orikawa, "Investigation of operational characteristics and efficiency enhancement of an ultrahigh-speed bearingless motor at 100 000 r/min," *IEEE Transactions on Industry Applications*, vol. 56, no. 4, pp. 3571–3583, 2020, DOI: 10.1109/TIA.2020.2986453.

[37] J. Asama and A. Chiba, "Performance evaluation of a homopolar bearingless motor for ultrahigh speed applications," *IEEE Transactions on Industry Applications*, vol. 57, no. 6, pp. 6913–6920, 2021, DOI: 10.1109/TIA.2021.3089556.

[38] P. Puentener, M. Schuck, J. W. Kolar, and D. Steinert, "Comparison of bearingless slice motor topologies for pump applications," in *in Proc. of IEEE International Electric Machines & Drives Conference (IEMDC)*, 2019, pp. 9–16, DOI: 10.1109/IEMDC.2019.8785163.

[39] P. Peralta, D. M. Araujo, and Y. Perriard, "Design of compact bearingless disc drive systems," *IEEE Transactions on Industry Applications*, vol. 56, no. 5, pp. 4870–4881, 2020, DOI: 10.1109/TIA.2020.3008368.

[40] D. Steinert, T. Nussbaumer, and J. W. Kolar, "Topology evaluation of slotless bearingless motors with toroidal windings," in *in Proc. of IEEE International Power Electronics Conference (IPEC-Hiroshima 2014-ECCE ASIA)*, 2014, pp. 975–981, DOI: 10.1109/IPEC.2014.6869705.

[41] D. Steinert, T. Nussbaumer, and J. W. Kolar, "Slotless bearingless disk drive for high-speed and high-purity applications," *IEEE Transactions on Industrial Electronics*, vol. 61, no. 11, pp. 5974–5986, 2014, DOI: 10.1109/TIE.2014.2311379.

[42] R. Schöb and N. Barletta, "Principle and application of a bearingless slice motor," *JSME International Journal Series C Mechanical Systems, Machine Elements and Manufacturing*, vol. 40, no. 4, pp. 593–598, 1997, DOI: 10.1299/jsmec.40.593.

[43] Y. Okada, "Self–bearing motors," in *Magnetic Bearings: Theory, Design, and Application to Rotating Machinery*. Springer, 2009, pp. 461–485, DOI: 10.1007/978-3-642-00497-1.

[44] M. C. Kulan, N. J. Baker, K. A. Liogas, O. Davis, J. Taylor, and A. M. Korsunsky, “Empirical implementation of the Steinmetz equation to compute eddy current loss in soft magnetic composite components,” *IEEE Access*, vol. 10, pp. 14 610–14 623, 2022, DOI: 10.1109/ACCESS.2022.3148593.

[45] J. Muhlethaler, J. Biela, J. W. Kolar, and A. Ecklebe, “Core losses under the DC bias condition based on Steinmetz parameters,” *IEEE Transactions on Power Electronics*, vol. 27, no. 2, pp. 953–963, 2011, DOI: 10.1109/TPEL.2011.2160971.

[46] A. Preumont, “Twelve lectures on structural dynamics,” in *Solid Mechanics and Its Applications*. Springer, 2013, vol. 198, DOI: 10.1007/978-94-007-6383-8.

[47] Shure Incorporated, “Product specifications beta 58a supercardioid dynamic vocal microphone,” 2015.

[48] Testo India Pvt Ltd, “Data sheet testo 816-1, sound level meter,” 2015.

[49] F. Briz, P. Garcia, M. W. Degner, D. Diaz-Reigosa, and J. M. Guerrero, “Dynamic behavior of current controllers for selective harmonic compensation in three-phase active power filters,” *IEEE Transactions on Industry Applications*, vol. 49, no. 3, pp. 1411–1420, 2013, DOI: 10.1109/TIA.2013.2253537.

[50] *Mechanical Vibration - Vibration of rotating machinery equipped with active magnetic bearings - Part 3: Evaluation of stability margin*, ISO Std. ISO 14 839-3: 2006 (E), 2006.

[51] S. Wang, B. Liang, W. Wang, L. Li, N. Feng, Y. Zhao, T. Wang, F. Yan, S. Yang, and X. Xia, “Viral vectored vaccines: Design, development, preventive and therapeutic applications in human diseases,” *Signal Transduction and Targeted Therapy*, vol. 8, no. 1, p. 149, 2023, DOI: 10.1038/s41392-023-01408-5.

[52] J. T. Bulcha, Y. Wang, H. Ma, P. W. Tai, and G. Gao, “Viral vector platforms within the gene therapy landscape,” *Signal Transduction and Targeted Therapy*, vol. 6, no. 1, p. 53, 2021, DOI: 10.1038/s41392-021-00487-6.

[53] U. Bezeljak, “Cancer gene therapy goes viral: Viral vector platforms come of age,” *Radiology and Oncology*, vol. 56, no. 1, pp. 1–13, 2022, DOI: 10.2478/raon-2022-0002.

[54] Alfa Wassermann Inc., "Products overview continuous flow ultracentrifugation," 2024.

[55] A. Flegler, M. Schneider, J. Prieschl, R. Stevens, T. Vinnay, and K. Mandel, "Continuous flow synthesis and cleaning of nano layered double hydroxides and the potential of the route to adjust round or platelet nanoparticle morphology," *RSC Advances*, vol. 6, no. 62, pp. 57 236–57 244, 2016, DOI: 10.1039/c6ra09553d.

[56] N. Singh and C. L. Heldt, "Challenges in downstream purification of gene therapy viral vectors," *Current Opinion in Chemical Engineering*, vol. 35, no. 100780, 2022, DOI: 10.1016/j.coche.2021.100780.

[57] A. Srivastava, K. M. Mallela, N. Deorkar, and G. Brophy, "Manufacturing challenges and rational formulation development for AAV viral vectors," *Journal of Pharmaceutical Sciences*, vol. 110, no. 7, pp. 2609–2624, 2021, DOI: 10.1016/j.xphs.2021.03.024.

[58] M. Wada, N. Uchida, G. Posadas-Herrera, H. Hayashita-Kinoh, Y. Tsunekawa, Y. Hirai, and T. Okada, "Large-scale purification of functional AAV particles packaging the full genome using short-term ultracentrifugation with a zonal rotor," *Gene Therapy*, vol. 30, no. 7, pp. 641–648, 2023, DOI: 10.1038/s41434-023-00398-x.

[59] H. Agarwal, C. Thwin, and B. T. Kumaar, "Single-use centrifugal separator enables intensification of the clarification process in biomanufacturing of recombinant proteins," *Journal of Chemical Technology & Biotechnology*, vol. 98, no. 5, pp. 1321–1332, 2023, DOI: 10.1002/jctb.7351.

[60] J. Walker, Y. Lam, A. Loman, J. P. Smelko, and M. Rohr, "Evaluation of a single-use disk stack centrifuge for improved efficiency and sustainability at 1000 L GMP manufacturing scale," *Biotechnology and Bioengineering*, vol. 120, no. 11, pp. 3347–3356, 2023, DOI: 10.1002/bit.28519.

[61] A. Borisavljevic, *Limits, modeling and design of high-speed permanent magnet machines.* Springer Science & Business Media, 2012, DOI: 10.1007/978-3-642-33457-3.

[62] A. Borisavljevic, S. Jumayev, and E. Lomonova, "Toroidally-wound permanent magnet machines in high-speed applications," in *in Proc. of IEEE International Conference on Electrical Machines (ICEM)*, 2014, pp. 2588–2593, DOI: 10.1109/ICELMACH.2014.6960552.

[63] F. Ferrucci, M. Merdzan, F. G. Capponi, and E. Lomonova, "Evaluation of eddy current losses in the cooling sleeve of a toroidal high speed permanent magnet machine," in *in Proc. of IEEE 2nd Global Power, Energy and Communication Conference (GPECOM)*, 2020, pp. 125–130, DOI: 10.1109/GPECOM49333.2020.9248718.

[64] H. Cohn, "A conceptual breakthrough in sphere packing," *arXiv preprint arXiv:1611.01685*, 2016, DOI: 10.48550/arXiv.1611.01685.

[65] N. Anderson, D. Waters, C. Nunley, R. Gibson, R. Schilling, E. Denny, G. Cline, E. Babelay, and T. Perardi, "K-series centrifuges I. Development of the k-II continuous-sample-flow-with-banding centrifuge system for vaccine purification," *Analytical Biochemistry*, vol. 32, no. 3, pp. 460–494, 1969, DOI: 10.1016/S0003-2697(69)80014-X.

[66] K. Piasta and P. Kupidura, "Perspective armour-piercing intermediate cartridge projectile," *Problemy Mechatroniki: Uzbrojenie, lotnictwo, inżynieria bezpieczeństwa*, vol. 14, 2023, DOI: 10.5604/01.3001.0016.2961.

[67] *Zentrifugen - Allgemeine Sicherheitsanforderungen*, DIN EN Std. DIN EN 12 547, 2014.

[68] Thyssenkrupp Materials Austria GmbH, "Werkstoffdatenblatt 1.7220."

[69] H. Roloff and W. Matek, *Roloff-Matek Maschinenelemente: Tabellen*. Springer Science & Business Media, 2007, vol. 2, DOI: 10.1007/978-3-8348-9998-9_24.

[70] L. He, Y. Feng, Y. Zhang, and B. Tong, "Methods for temperature estimation and monitoring of permanent magnet: A technology review and future trends," *Journal of the Brazilian Society of Mechanical Sciences and Engineering*, vol. 46, no. 4, p. 174, 2024, DOI: 10.1007/s40430-024-04723-2.

[71] E. J. Hubmann, F. Weissofner, D. Steinert, T. Nussbaumer, and J. W. Kolar, "Novel acoustic failure prediction method for active magnetic bearing systems," *IEEE/ASME Transactions on Mechatronics*, vol. 29, no. 2, pp. 1181–1192, 2023, DOI: 10.1109/TMECH.2023.3301815.

[72] M. Hutterer and M. Schroedl, "Stabilization of active magnetic bearing systems in the case of defective sensors," *IEEE/ASME Transactions on Mechatronics*, vol. 27, no. 5, pp. 3672–3682, 2021, DOI: 10.1109/TMECH.2021.3131224.

[73] G. B. Gallego, L. Rossini, E. Onillon, T. Achtnich, C. Zwyssig, R. Seiler, D. M. Araujo, and Y. Perriard, "On-line micro-vibration measurement method for Lorentz-type magnetic-bearing space actuators," *Mechatronics*, vol. 64, p. 102283, 2019, DOI: 10.1016/j.mechatronics.2019.102283.

[74] A. H. Pesch and P. N. Scavelli, "Condition monitoring of active magnetic bearings on the internet of things," vol. 8, no. 1, p. 17, 2019, DOI: 10.3390/act8010017.

[75] W. Wang and O. A. Jianu, "A smart sensing unit for vibration measurement and monitoring," *IEEE/ASME Transactions on Mechatronics*, vol. 15, no. 1, pp. 70–78, 2009, DOI: 10.1109/TMECH.2009.2016956.

[76] G. Michau, G. Frusque, and O. Fink, "Fully learnable deep wavelet transform for unsupervised monitoring of high-frequency time series," *Proceedings of the National Academy of Sciences*, vol. 119, no. 8, pp. 1–10, 2022, DOI: 10.1073/pnas.2106598119.

[77] J. L. Ferrando Chacon, "Fault detection in rotating machinery using acoustic emission," Ph.D. dissertation, Brunel University London, 2015.

[78] J. N. Schoess, "Rotor acoustic monitoring system (RAMS): a fatigue crack detection system," vol. 2717, pp. 212–218, 1996, DOI: 10.1117/12.239023.

[79] L. Lin and F. Chu, "Hht-based ae characteristics of natural fatigue cracks in rotating shafts," *Mechanical Systems and Signal Processing*, vol. 26, pp. 181–189, 2012, DOI: 10.1016/j.ymssp.2011.07.017.

[80] D. D. Quinn, G. Mani, M. E. Kasarda, T. Bash, D. J. Inman, and R. G. Kirk, "Damage detection of a rotating cracked shaft using an active magnetic bearing as a force actuator-analysis and experimental verification," *IEEE/ASME Transactions on Mechatronics*, vol. 10, no. 6, pp. 640–647, 2005, DOI: 10.1109/TMECH.2005.859833.

[81] C. H. Marais, "High speed flexible rotor active magnetic bearing control," Ph.D. dissertation, North-West University, 2006.

[82] G. E. Piper, J. M. Watkins, and O. G. Thorp III, "Active control of axial-flow fan noise using magnetic bearings," *Journal of Vibration and Control*, vol. 11, no. 9, pp. 1221–1232, 2005, DOI: 10.1177/1077546305057261.

[83] G. B. Gallego, L. Rossini, T. Achtnich, D. M. Araujo, and Y. Perriard, "Novel generalized notch filter for harmonic vibration suppression in magnetic bearing systems," *IEEE Transactions on Industry Applications*, vol. 57, no. 6, pp. 6977–6987, 2021, DOI: 10.1109/TIA.2021.3062587.

[84] M. K. Müller, "On-line process monitoring in high speed milling with an active magnetic bearing spindle," Ph.D. dissertation, ETH Zurich, 2002.

[85] I. Inasaki, T. Blum, I. Suzuki, H. Itagaki, and M. Sato, "A practical mounting device for an acoustic emission sensor for the failure detection of multipoint cutting tools," *Transactions of the Institute of Systems, Control and Information Engineers*, vol. 2, no. 6, pp. 210–221, 1989, DOI: 10.5687/iscie.2.210.

[86] P. K. Wong and J. S. Biao, "Fault diagnosis of induction motors under untrained loads with a feature adaptation and improved broad learning framework," *IEEE/ASME Transactions on Mechatronics*, vol. 27, no. 5, pp. 3041–3052, 2021, DOI: 10.1109/TMECH.2021.3125767.

[87] O. Mey, A. Schneider, O. Enge-Rosenblatt, D. Mayer, C. Schmidt, S. Klein, and H.-G. Herrmann, "Condition monitoring of drive trains by data fusion of acoustic emission and vibration sensors," *Processes*, vol. 9, no. 7, p. 1108, 2021, DOI: 10.3390/pr9071108.

[88] ANSYS Inc., "Ansys NVH solutions for electric vehicles, whitepaper," 2019.

[89] P. Kotter, "Vibroacoustics of electrical drive systems," Ph.D. dissertation, ETH Zurich, 2019, DOI: 10.3929/ethz-b-000344764.

[90] M. Boesing and R. W. De Doncker, "Exploring a vibration synthesis process for the acoustic characterization of electric drives," *IEEE Transactions on Industry Applications*, vol. 48, no. 1, pp. 70–78, 2011, DOI: 10.1109/TIA.2011.2175469.

[91] A. Gilson, G. Verez, F. Dubas, D. Depernet, and C. Espanet, "Design of a high-speed permanent-magnet machine for electrically-assisted turbocharger applications with reduced noise emissions," in *in Proc. of IEEE International Electric Machines and Drives Conference (IEMDC)*, 2017, pp. 1–6, DOI: 10.1109/IEMDC.2017.8002386.

[92] E. J. Hubmann, C. F. Blaser, S. Erismann, D. Steinert, T. Nussbaumer, and J. W. Kolar, "Magnetically self-bearing drive system for ultracentrifugation: Towards 100'000 rpm and 200'000 g," in *in Proc. of 24th International Conference on Electrical Machines and Systems (ICEMS)*, 2021, pp. 88–94.

[93] G. Schweitzer, "Active magnetic bearings-chances and limitations," in *6th International Conference on Rotor Dynamics*. ETH Zurich, 2002, pp. 1–14.

[94] R. Larsonneur, "Principle of active magnetic suspension," in *Magnetic Bearings: Theory, Design, and Application to Rotating Machinery*. Springer, 2009, pp. 27–68, DOI: 10.1007/978-3-642-00497-1_2.

[95] J. Sun, M. Jolly, , and M. t. Norris, "Passive, adaptive and active tuned vibration absorbers—a survey," *ASME. J. Vib. Acoust.*, vol. 117B, pp. 234–242, 1995, DOI: 10.1115/1.2838668.

[96] D. Pilbauer, T. Vyhlídal, and N. Olgac, "Delayed resonator with distributed delay in acceleration feedback—Design and experimental verification," *IEEE/ASME Transactions on Mechatronics*, vol. 21, no. 4, pp. 2120–2131, 2016, DOI: 10.1109/TMECH.2016.2516763.

[97] R. Khatri, L. Hawkins, M. Ortiz Neri, F. Cangioli, and D. Biliotti, "Design and prototype test data for a 300 kW amb-supported turbine generator for natural gas pressure letdown," in *ASME Turbo Expo: Power for Land, Sea, and Air*, vol. 7B. American Society of Mechanical Engineers, 2019, DOI: 10.1115/GT2019-91172.

[98] R. Humphris, P. Allaire, D. Lewis, and L. Barrett, "Diagnostic and control features with magnetic bearings," in *in Proc. of IEEE 24th Intersociety Energy Conversion Engineering Conference*, 1989, pp. 1491–1498, DOI: 10.1109/IECEC.1989.74666.

[99] E. Maslen, P. Allaire, M. Noh, and C. Sortore, "Magnetic bearing design for reduced power consumption," *ASME. J. Tribol.*, vol. 118, no. 4, pp. 839–846, 1996, DOI: 10.1115/1.2831617.

[100] M. O. Cole and W. Fakkaew, "An active magnetic bearing for thin-walled rotors: Vibrational dynamics and stabilizing control," *IEEE/ASME Transactions on Mechatronics*, vol. 23, no. 6, pp. 2859–2869, 2018, DOI: 10.1109/TMECH.2018.2877777.

[101] J. R. Pierce, "Physical sources of noise," *Proceedings of the IRE*, vol. 44, no. 5, pp. 601–608, 1956, DOI: 10.1109/JRPROC.1956.275123.

[102] E. H. Maslen, G. Schweitfzer, H. Bleuler, and M. Cole, *Magnetic bearings: Theory, design, and application to rotating machinery.* Springer, 2009, DOI: 10.1115/1.2831617.

[103] *Mechanical Vibration: Vibration of Rotating Machinery Equipped with Active Magnetic Bearings. Evaluation of Vibration*, International Organization for Standardization Std. ISO 14 839-4, 2004.